Lire
la seconde partie
de la thèse

CHAPITRE 8

Etude du cliquetis sur le point de fonctionnement de référence.

Dans ce chapitre, tous les modèles et méthodologies présentées partie I sont appliquées au point de fonctionnement de référence de la base de données ICAMDAC (cas baseline*). Dans une première partie, le point de fonctionnement* baseline *déjà calculé par Robert (2014) avec le modèle de combustion CFM couplé à TKI est recalculé avec la méthodologie TFLES-IPRS. L'objectif est ici double: d'une part confronter cette nouvelle méthodologie à un cas d'application réel, d'autre part comparer et analyser les comportements et prédictions des deux approches. Pour ce faire, tous les autres paramètres des calculs sont conservés identiques: la méthodologie ESO_2 est utilisée et les températures de parois empiriques sont conservées. La seconde partie se présente sous la forme d'un article soumis au journal Combustion and Flames qui traite de l'étude de ce même point de fonctionnement* baseline *dans le cadre d'un couplage thermique fluide-solide permettant d'utiliser des températures de paroi réalistes issues d'un calcul couplé et non pas d'approches empiriques.*

Partie II: Etude des combustions anormales

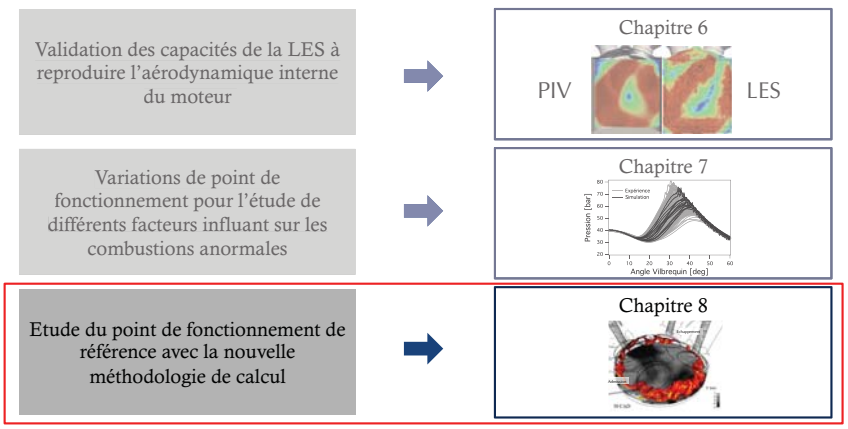

8.1 Confrontation des approches CFM-TKI et TFLES-IPRS pour le calcul des combustions anormales

La collaboration CERFACS/IFPEN en LES présente un avantage important: différentes approches de modélisation de la combustion turbulente sont disponibles dans le même code et peuvent être comparées. Pour la simulation des combustions anormales, deux approches sont disponibles dans *AVBP*:

- l'approche utilisée par Robert (2014) où la propagation turbulente est modélisée par CFM couplé à TKI pour l'auto-allumage;
- l'approche développée dans cette thèse où la propagation turbulente est modélisée par TFLES couplé à IPRS pour l'auto-allumage.

Ce chapitre compare les résultats fournis par ces deux méthodes.

8.1.1 Mise en données et méthodologie numérique

Le moteur ECOSURAL en version opaque est utilisé pour cette étude. Dans la première partie de ce chapitre les paramètres de simulation sont repris de Robert (2014) hormis les modèles combustions afin de comparer les méthodologies CFM-TKI et TFLES-IPRS. En particulier, le couplage thermique décrit Chap. 5 n'est pas utilisé. Pour rappel, les caractéristiques du point de fonctionnement *baseline* et les températures imposées à la paroi sont résumés Tab. 8.1 et Tab. 8.2. Les relevés expérimentaux de pression en entrée et sortie du domaine sont utilisés

Paramètre	Unité	*baseline*
Régime moteur	[tr/min]	1800
P_{adm}	[bar]	1.8
Carburant	[-]	C_8H_{18}
Aérodynamique des conduits d'admission	[-]	standard
Taux de dilution (par N_2)	[%]	0

Table 8.1: Caractéristiques du point de fonctionnement *baseline*.

Région	*baseline*
Haut de chemise	459 K
Bas de chemise	418 K
Piston	497 K
Soupapes admission	639 K
Queues de soupapes admission	383 K
Soupapes échappement	784 K
Queues de soupapes échappement	403 K
Culasse	409 K
Collecteur admission	374 K
Collecteur échappement	379 K

Table 8.2: Conditions limites thermiques utilisées pour le point de fonctionnement *baseline*.

comme conditions limites d'entrée et sortie de la simulation à l'aide du formalisme NSCBC. La méthodologie ESO_2 est utilisée et le modèle de sous maille est le modèle de Smagorinsky. De

même que dans le Chap. 7, les simulations réalisées dans ce chapitre ne rendent pas compte de l'injection directe du carburant dans le cylindre mais celui-ci est introduit sous forme gazeuse au moment de la phase d'admission.

Tous les résultats obtenus avec la méthodologie CFM-TKI sont issus des travaux de Robert (2014). Afin de minimiser les temps de calcul, les simulations TFLES-IPRS présentées ne sont réalisées que pour les phases de compression et combustion. Pour chaque cycle, la solution initiale utilisée est la solution du calcul CFM-TKI au moment de la fermeture des soupapes d'admission pour le cycle correspondant.

8.1.2 Résultats sur le point de fonctionnement de référence

La figure 8.1 compare les évolutions temporelles de la pression dans le cylindre entre l'expérience et les deux méthodologies de calcul. Dans un premier temps et avant de comparer les deux

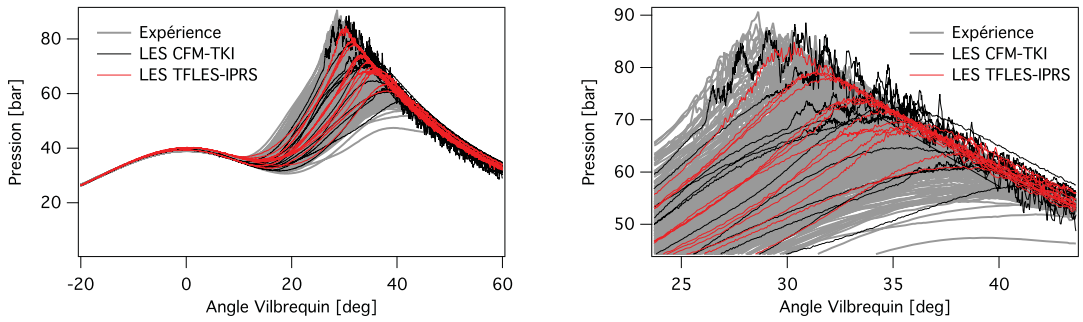

Figure 8.1: Evolution temporelle de la pression dans le cylindre avec les méthodologies CFM-TKI et TFLES-IPRS pour un allumage 6DV après le PMH. Zoom sur les pressions les plus élevées à droite.

simulations en termes de combustions anormales, il est intéressant de remarquer que les deux méthodologies donnent des enveloppes de pression dans le cylindre proches et en bon accord avec l'expérience. Les niveaux de pression moyenne ainsi que son coefficient de variation pour ce point de fonctionnement sont regroupés Tab. 8.3. Les deux simulations donnent des résultats

	PMI [bar]	Cov(PMI) [%]
Expérience (Moyenne / 500 cycles)	19.06	2.6
Expérience (Moyenne / 15 cycles)	[18,62-19.25]	[1.7-3.7]
LES (CFM-TKI)	19.5	2.7
LES (TFLES-IPRS)	19,21	2,9

Table 8.3: Pression moyenne dans le cylindre sur le point *baseline* avec les méthodologies CFM-TKI et TFLES-IPRS avec allumage 6 DV après le PMH.

proches et conformes à l'expérience. Comme dans les études de Enaux (2010) et Granet (2011), le modèle de combustion TFLES permet de modéliser correctement la combustion dans ce moteur fonctionnant à charge plus élevée. Bien que les deux simulations soient réalisées à partir de la même solution initiale au moment de la fermeture des soupapes d'admission, la combustion n'est pas identique entre les deux calculs lorsque l'on considère un cycle isolé. Par exemple, la Fig. 8.2 compare le déroulement de la combustion du cycle 6 pour les deux approches. Ce cycle est celui qui présente la plus grande intensité de cliquetis, que ce soit dans la simulation CFM-TKI ou la simulation TFLES-IPRS. Il est difficile de comparer les deux simulations de manière

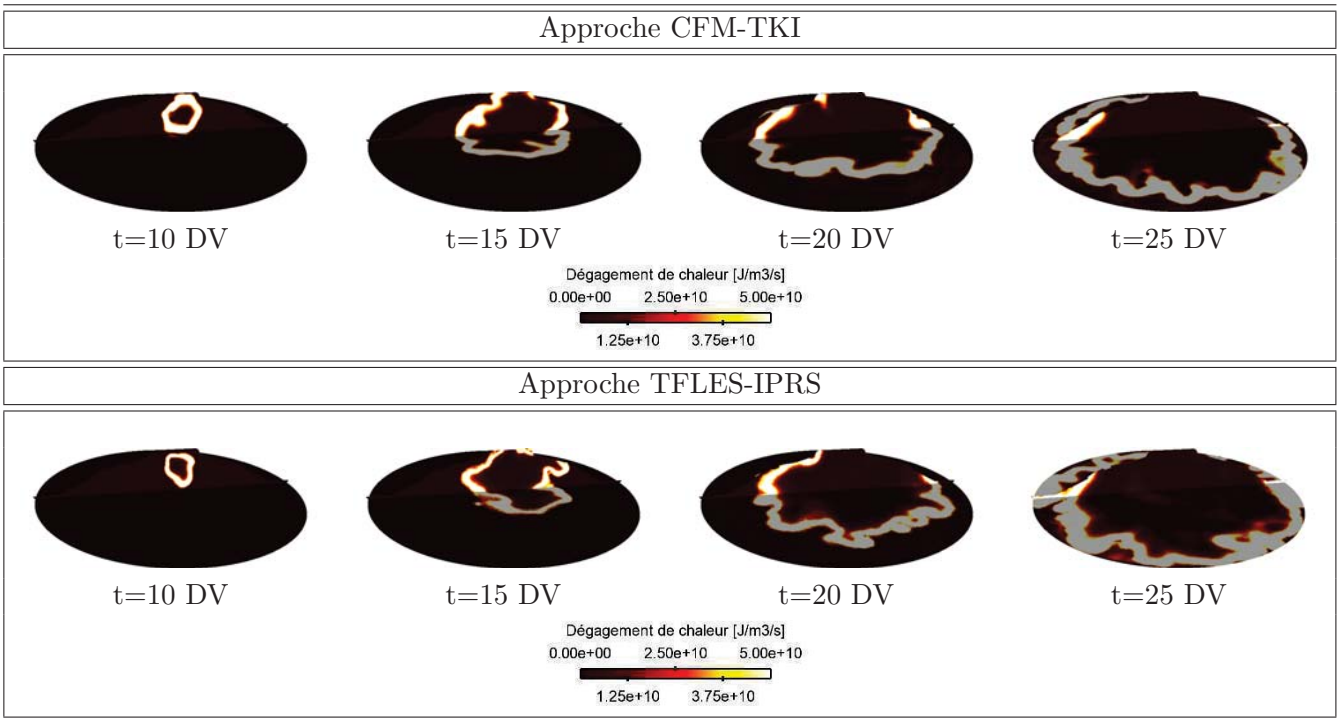

Figure 8.2: Déroulement de la combustion avec les méthodologies CFM-TKI et TFLES-IPRS pour un allumage 6 DV après le PMH pour le cycle 6. L'admission est à gauche des figures tandis que l'échappement se situe coté droit. Le temps des solutions est donné en référence au PMH.

fine: en plus des modèles de propagation turbulente et d'auto-allumage qui diffèrent, le modèle d'allumage (ISSIM dans la simulation CFM-TKI et ED dans la simulation TFLES-IPRS) est également très différent. Malgré ces approches très différentes, la combustion se déroule de manière très similaire entre les deux simulations aussi bien en termes de vitesse de combustion que d'épaisseur et le plissement du front de flamme résolu (jusque 20 DV après le PMH). Au delà, des différence plus marquées apparaissent: 25 DV après le PMH, on remarque notamment que la flamme a consommé l'intégralité des gaz frais coté échappement dans le cas TFLES-IPRS alors que ce n'est pas le cas avec les modèles CFM-TKI.

En termes de combustions anormales, la Fig. 8.1 montre deux résultats essentiels: (i) dans les deux cas, pour les cycles moteur dont la pression est dans la partie supérieure de l'enveloppe, des oscillations représentatives du cliquetis sont observées, (ii) ces oscillations sont nettement moins intenses dans la simulations TFLES-IPRS par rapport à la simulation CFM-TKI. Pour quantifier le cliquetis sur ce point de fonctionnement, l'outil de post-traitement présenté Chap. 7.3 est utilisé. Les résultats sont présentés Tab. 8.4. De même que dans le Chap. 7, en plus des statis-

	Cycles cliquetants [%]	Angle de départ d'AI [deg]
Expérience (Moyenne / 500 cycles)	51.51	31.61
Expérience (Moyenne / 15 cycles)	[13.34-80.0]	[29.92-35.24]
LES (CFM-TKI)	73.3	35.1
LES (TFLES-IPRS)	40.0	32.56

Table 8.4: Statistiques de cliquetis sur le point *baseline* avec les méthodologies CFM-TKI et TFLES-IPRS avec allumage 6 DV après le PMH.

tiques globales, l'expérience est également analysée par échantillons de 15 cycles. Cette analyse expérimentale sur un nombre de cycles identique à la LES permet de déterminer une enveloppe de variabilité des résultats afin de faciliter les comparaisons. Dans les deux cas, les pourcentages de cliquetis et l'angle de départ du cliquetis se situent dans l'enveloppe expérimentale, montrant ainsi que les deux approches reproduisent quantitativement le cliquetis sur ce point de fonctionnement. L'occurrence du cliquetis est cependant plus faible avec les modèles TFLES et IPRS. Tous les cycles pour lesquels du cliquetis est observé avec les modèles TFLES et IPRS sont aussi des cycles avec cliquetis dans l'approche CFM-TKI mais l'inverse n'est pas vrai.

Comme le montre la Fig. 8.3, bien que les statistiques de cliquetis soient similaires entre les deux simulations, le cliquetis n'apparait pas dans la même région du moteur. L'auto-allumage se

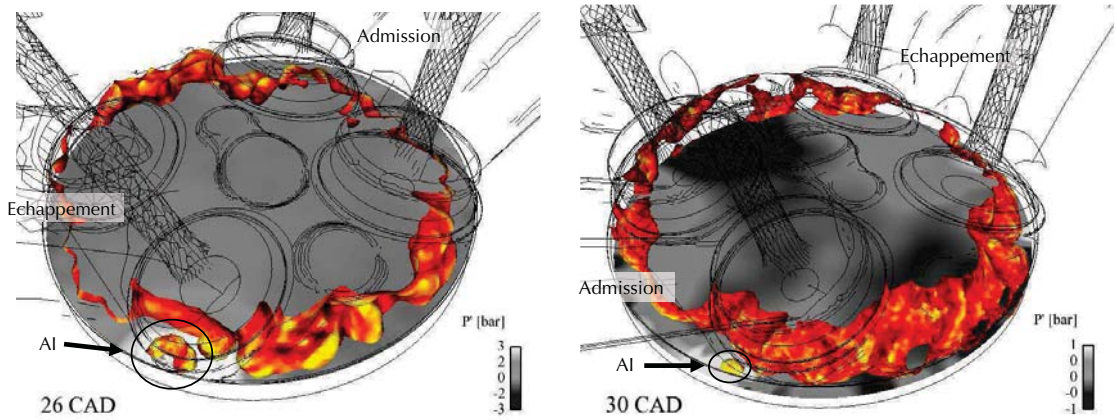

Figure 8.3: Visualisation de l'auto-allumage au cours du cycle 6 avec un allumage 6 DV après le PMH. Iso-surface de variable de progrès ($c = 0.5$) colorée par la courbure et coupe $(\vec{x}, \vec{y})$ colorée par les fluctuations de pression. Simulation CFM-TKI à gauche et simulation TFLES-IPRS à droite.

produit plus tôt dans le cas CFM-TKI et sous la soupape d'échappement dont la température est plus élevée. Dans le cas TFLES-IPRS, la flamme se propage plus vite vers les soupapes d'échappement: 25 DV après le PMH la totalité des gaz frais est consommée coté échappement (Fig. 8.2). En conséquence, aucun auto-allumage n'est constaté dans cette région. En revanche, pour ce cycle, l'auto-allumage se produit coté admission où la flamme se propage plus lentement. La figure 8.3 met également en évidence une onde de pression importante (de l'ordre de 3 bar) générée dans le cas CFM-TKI. Dans le cas TFLES-IPRS, une onde est également générée mais son amplitude est moindre, de l'ordre du bar.

Une autre caractéristique importante de ces modèles est leur coût de calcul. Il est possible de déterminer le temps de calcul lié au modèle de combustion en comparant l'efficacité du code de calcul pendant les phases purement aérodynamiques et pendant les phases de combustion avec chacune des deux approches. L'efficacité, en temps de calcul par itération et par noeud, est résumé Tab. 8.5 pour les différents cas. Le surcoût dû à la combustion est donc de 1.65 10^{-7}

	Efficacité réduite [s.CPU/noeud/itération]
Phase aérodynamique	6.57 10^{-7}
Phase de combustion avec CFM-TKI	8.22 10^{-7}
Phase de combustion avec TFLES-IPRS	7.18 10^{-7}

Table 8.5: Efficacité réduite moyenne du code *AVBP*.

s/CPU/noeud/itération avec l'approche CFM-TKI et 0.61 10^{-7} s/CPU/noeud/itération avec l'approche TFLES-IPRS. La modélisation de la combustion à l'aide des modèles IPRS-TFLES est donc sensiblement plus efficace. Cette différence entre les deux approches abouti à des différences de temps de calcul sensibles. Pour la phase de combustion uniquement, *i.e.* du PMH jusque 88 DV après le PMH, l'approche CFM-TKI donne un temps de calcul de l'ordre de 16.10^3 hCPU tandis que l'approche TFLES-IPRS nécessite environ 12.10^3 hCPU sur le calculateur neptune BULL B510 du CERFACS.

En résumé, les deux simulations fournissent des résultats très proches malgré des modèles d'allumage, de propagation et d'auto-allumage très différents. Dans un contexte de moteurs à piston, où le développement de la flamme est par nature très instationnaire, comparer des modèles différents est une tache difficile. En effet, les non linéarités des équations résolues peuvent amplifier les plus petites différences introduites par les différents modèles et aboutir à des réalisations très différentes. De plus, dans le cas présent, il ne s'agit pas de faire varier uniquement un modèle mais une combinaison de trois modèles différents (allumage, propagation et auto-allumage) qui peuvent interagir entre eux. Enfin, certains diagnostiques sont difficilement réalisables avec les modèles TFLES et IPRS. Par exemple, des informations souvent utilisées pour étudier le cliquetis sont les évolutions de la surface de flamme d'auto-allumage ou la quantité de gaz brulée par auto-allumage. Grâce à des variables de progrès bien séparées, il est facile de discriminer les deux modes de combustion dans l'approche CFM-TKI. En revanche, avec les modèles TFLES et IRPS, une description unique est utilisée pour l'auto-allumage et pour la propagation de la flamme. Il est alors très difficile de séparer rigoureusement ces deux contributions de la combustion et faire des diagnostiques séparés. Dans l'ensemble, les résultats des deux approches sont en bon accord avec les relevés expérimentaux à la fois en termes de combustion "normales" (pression moyenne, variabilité cycle à cycle) que de combustions anormales (statiques d'apparition du cliquetis) mais pour les raisons citées précédemment, il est difficile de comparer plus finement les deux approches.

8.2 Impact du couplage thermique sur la combustion

La section précédente a montré la capacité des modèles TFLES et IPRS à reproduire un point de fonctionnement avec combustions anormales. Dans la suite, ces modèles de combustion sont conservés pour étudier l'influence des conditions limites thermiques sur la combustion. Cette section se présente sous la forme d'un article soumis au journal *Combustion and Flames*.

LES of knocking in engines using dual heat transfer and two-step reduced schemes.

Antony Misdariis[a,b], Olivier Vermorel[b], Thierry Poinsot[c]

[a] *Renault SAS, 1 Allée Cornuel, 91570 Lardy, France*
[b] *CERFACS, CFD Team, 42 Avenue G. Coriolis, 31057 Toulouse Cedex 01, France*
[c] *Institut de Mécanique des Fluides de Toulouse, CNRS, Avenue C. Soula, 31400 Toulouse, France*

Abstract

Large Eddy Simulation of knocking in piston engines requires high-fidelity physical models and numerical techniques. The need to capture temperature fields with high precision to predict autoignition is an additional critical constraint compared to existing LES in engines. The present work presents advances for LES of knocking in two fields: (1) a reduced two-step scheme is used to predict both propagating premixed flames as well as autoignition times over a wide range of equivalence ratios, pressures and temperatures and (2) a Conjugate Heat Transfer (CHT) technique is implemented to compute the flow within the engine over successive cycles with LES together with the temperature field within the cylinder head walls and the valves. The paper focuses on CHT which is critical for knocking because the gas temperature field is controlled by the wall temperature field and knocking is sensitive to small temperature changes. The CHT LES is compared to classical LES where the temperatures of the head and the valves are supposed to be homogeneous and imposed empirically. Results show that the skin temperature field (which is a result of the CHT LES while it is a user input for classical LES) is complex and controls knocking events. While the results of the CHT LES are obviously better because they suppress a large part of the empirical specification of the wall temperatures, this study also reveals a difficult and crucial element of the CHT approach: the description of exhaust valves cooling which are in contact with the engine head for part of the cycle and not in the rest of the cycle, leading to difficulties for heat transfer descriptions between valves and head. The CHT method is successfully applied to an engine studied at IFP Energies Nouvelles where knocking characteristics have been studied over a wide range of conditions.

Keywords: LES, Knock, Autoignition, Internal combustion engine, Heat transfert

1. Introduction

To increase the efficiency of reciprocating engines, downsizing has become a new standard in the automotive industry [17]. By combining smaller cylinder sizes with turbo-chargers, engines can be operated in a region of higher efficiency. For moderate downsizing levels, this technique enables to decrease fuel consumption significantly and thus pollutants emissions. However abnormal combustions prevent engine manufacturers from using advanced levels

of downsizing. Abnormal combustion results from the competition between the turbulent propagation of the premixed flame initiated by the spark plug and the spontaneous ignition of the fresh gas. When high pressure and high temperature are encountered in the fresh gas in front of the flame front (also called end-gas), the auto-ignition delay drops and can become lower than the time needed by the premixed flame to burn the charge. This kind of auto-ignition events leads to abnormal combustions such as knocking or rumble and can destroy the engine. Over the last decades, the increase of engines compression ratios lead to the same issues [5, 26] and a better understanding of heat transfer and engine cooling allowed to control knocking. Nowadays, such fluid/solid interactions remain a key-parameter but it is not sufficient to control abnormal combustions in highly downsized engines. Increasing the engine resistance to knocking requires a better understanding of these phenomena. Although optical diagnostics are not easy to perform, existing experimental studies [2, 19, 18] highlighted some key features leading to abnormal combustions: (1) the intensity of knock is linked to the portion of fresh gas when auto-ignition occurs [20] and (2) detonation waves may appear in knocking cycles. The basic mechanism leading to detonation in such flows was studied by Zeldovich [37] who showed that a 1D temperature gradient in a flow close to auto-ignition could initiate a detonation wave. This mechanism was studied later by Bradley *et. al.* [3] or Clavin *et. al.* [6] and has become the prototype configuration used to illustrate how detonation can begin in an engine. Even though detonation can hardly be observed directly inside a piston engine several studies were carried-out in canonical configurations [37, 11] suggesting that conditions were indeed favorable to detonation in knocking engines.

In this context, Large Eddy Simulations (LES) can provide detailed information to analyze abnormal combustion. Peters *et. al.* [30] used simulations to identify regions where a Deflagration to Detonation Transition (DDT) can occur based on cold flow LES results and on the Zeldovich *et. al.* theory. Robert *et. al.* [34] proved that LES can be used to evaluate the knocking tendency of an experimental engine. They retrieved quantitatively the experimental behavior of the real engine and performed a first analysis of abnormal combustion thanks to LES.

Obviously temperature plays a major role for knock and in a real engine the temperature field is expected to control knocking events to a large extent. For instance, wall heat transfer dictates the temperature level at Top Dead Center (TDC) when ignition is performed just before knock can begin near hot regions. This issue becomes even more important for engines running with abnormal combustion where local and intermittent hot spots found near high temperature walls can initiate auto-ignition inside fresh gases. In that sense, the use of realistic wall temperatures is of first importance when studying abnormal combustions with numerical simulations. The potential benefits of conjugate heat transfer simulations for piston engines flows are pointed out in [24] and the same methodology is used in [25]. As LES becomes a higher precision method, it is very likely that a high precision description of wall temperatures will become mandatory. This is one of the objectives of the present paper which focuses on the apparition of abnormal combustions. Although previous studies proved that information on knocking can be obtained with a first order estimation of the wall temperatures, the study presented in this paper includes a comprehensive description

of conjugate heat transfer with LES.

2. Configuration and methodology

In an engine, conjugate heat transfer controls wall temperatures and has a strong impact on combustion [23] because of the long residence time of the fresh gas in the cylinder prior to combustion triggered around TDC. The large variations of the combustion chamber volume and thus of the thermodynamic conditions promote heat exchanges at the boundaries and impact the combustion process. The wall temperatures used in numerical simulations are usually obtained from experimental measurements or from *a priori* estimations. This approach can provide an appropriate global behavior but local information is missing. In particular, the sophisticated cooling system used for the cylinder head can lead to temperature in-homogeneities that can have an impact on abnormal combustion. Only one hot wall zone can be enough to trigger knocking. This situation differs from 'classical' LES in engines, far from knocking conditions where wall temperatures play a more limited role [32, 10, 15]. In this paper, conjugate heat transfer is solved by means of a fully coupled simulation between fluid and solid so that relevant boundary conditions can be used to study knocking. While such studies have already been performed using RANS [25], they require much more care in a true LES framework as described in the next section.

2.1. Coupling methodology

In order to use realistic boundary conditions, a common strategy consists in using two different solvers: one for LES and another one to solve the heat equation in the solid domain. In such simulations, the characteristic time of the heat conduction in the solid $\tau_s \sim L^2/D_s$ (with L the solid characteristic length and D_s the solid diffusivity) is often several orders of magnitude higher than the combustion characteristic time $\tau_c \sim \delta_l/S_L$ (with δ_l the flame thickness and S_L the flame speed). For instance, assuming a valve head of $L = 10$ mm and with the properties of steel (Tab. 1), the conduction characteristic time is:

$$\tau_s = \frac{L^2}{\lambda/(\rho Cp)} = \frac{0.01^2}{36/(7500.450)} = 9s \tag{1}$$

while for an iso-octane/air flame at 40 bar and 700 K, the combustion characteristic time is:

$$\tau_c = \delta_l/S_L = \frac{1.10^{-4}}{1.0} = 1.10^{-4}s \tag{2}$$

For this particular case, the conduction characteristic time is 5 orders of magnitude bigger than the conduction characteristic time: the solid acts like a low-pass filter and only sees a mean heat flux coming from the fluid domain. A numerical difficulty directly introduced by this time scales difference is that the convergence speeds differs in the fluid and in the solid domains. The convergence for the solid temperature is too long to be computed with LES. In practice however, this time scales difference can be exploited efficiently by recognizing that

only a weak coupling between the two domains is sufficient. Decoupling the computations of LES in the cylinder and temperature in the solid walls allows to reach a converged state at the fluid/solid interface by only considering a mean averaged field of heat fluxes as inputs for the heat transfer simulation in the solid. The methodology used to obtain the converged conjugated heat transfer at the fluid/solid interface is based on such a weak coupling (Fig. 1). The two solvers are run sequentially: first, an initial set of wall skin temperatures is obtained

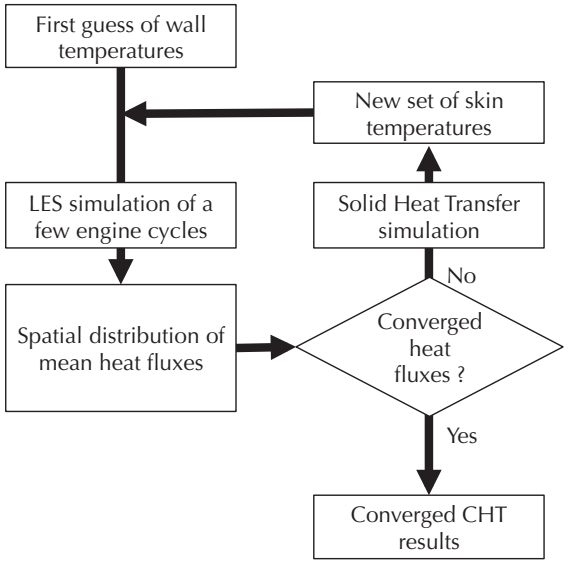

Figure 1: Diagram of the weak coupling algorithm to perform a Conjugated Heat Transfer (CHT) simulation.

from experimental measurements or from 0D simulations [29]. This set of wall temperature is used to compute the fluid dynamics thanks to the LES solver and wall Heat Fluxes (HF) are locally integrated over the full engine cycle. Then, the Heat Transfer (HT) solver is used to compute the steady temperature field inside the solid domain. Finally, the converged temperature at the fluid/solid interface is used to update the wall temperature field of the LES simulation. This coupling loop is performed until convergence of the heat fluxes and temperature at the interface.

2.2. Numerical set-up

In the present work, the fully compressible explicit code (called AVBP) is used to solve the filtered multi-species 3D Navier-Stokes equations with realistic thermochemistry on unstructured meshes [35, 13]. Based on the ESO_2 approach [27], numerics is handled with the second-order accurate in space and time Law-Wendroff scheme [22] and a Two-step Taylor-Galerkin finite element scheme (TTG), third-order accurate in space and time [7] for phases with require increased accuracy (compression and combustion). The Smagorinsky sub-grid scale model is used [36] and boundary conditions use the NSCBC approach [31]. Combustion is modeled with a simple 2-step scheme chemistry and a combination of the TFLES [4] and IPRS [28] models for the flame propagation and auto-ignition. The IPRS approach allows to compute the whole combustion phase with a single expression for reaction rates which

captures both auto-ignition time in well-stirred reactors (thereby able to predict the onset of knocking) and the structure of premixed flames which develop in engine before or after knocking takes place. The same model also captures the front after detonation is initiated, if needed. The Energy Deposition (ED) model [21] is used for spark ignition and moving meshes are handled with the ALE formalism [16].

The energy equation inside the solid domain is solved by the AVTP solver [9]. Spatial discretization is handled with a second-order Galerkin scheme [8] and temporal integration uses a first-order forward implicit scheme. The resolution of the implicit system is done with a parallel matrix free conjugate gradient method [12]. Heat fluxes are determined by means of a Fourier's law and temperature dependent heat conductivity coefficients and heat capacities are used.

As shown in Fig 2, the LES simulation for one cycle represents 67 ms of physical time (for an engine speed of 1800 rpm) while 60 seconds of physical time are needed to reach steady state inside the solid. However, thanks to the use of an implicit time marching, the heat transfer simulation inside the solid uses large time-steps and the final cost is negligible compared to the LES simulation. Eventually, the cost of the CHT simulation is only

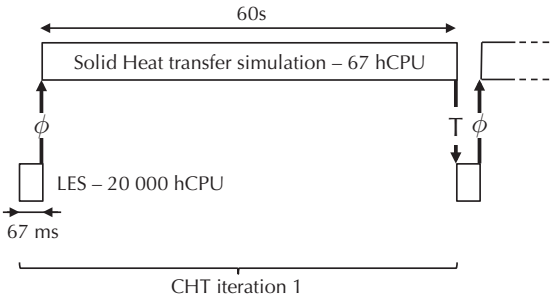

Figure 2: Schematic of the Conjugated Heat Transfer (CHT) simulation.

due to the extra LES simulations performed at each CHT iteration to reach a converged temperature field at the fluid/solid interface.

2.3. Experimental configuration and operating point

The target configuration is an experimental mono-cylinder 4 valves turbo-charged ECO-SURAL engine shown in Fig. 3. This engine is installed at *IFP Energies Nouvelles* in the framework of the french ANR (Research National Agency) ICAMDAC project to study abnormal combustion in downsized spark-ignited engines. The spatial discretization uses full tetrahedral meshes for the fluid and solid domains. The fluid domain begins in the inlet plenum and finishes on the outlet plenum, a procedure which has been shown to provide the required accuracy for LES by specifying boundary conditions far away from the cylinder [10, 14]. The mesh size for the fluid domain varies between 2.2 and 12 million cells while a fixed 1.7 million cells mesh is used for the solid domain. As shown in Fig. 4, the mesh at the fluid/solid interface is the same between the two domains. Two metals are accounted for in the CHT solver: the cylinder head is made of cast iron while steel is used for valves. The properties of cast iron and steel are summarized in Tab. 1.

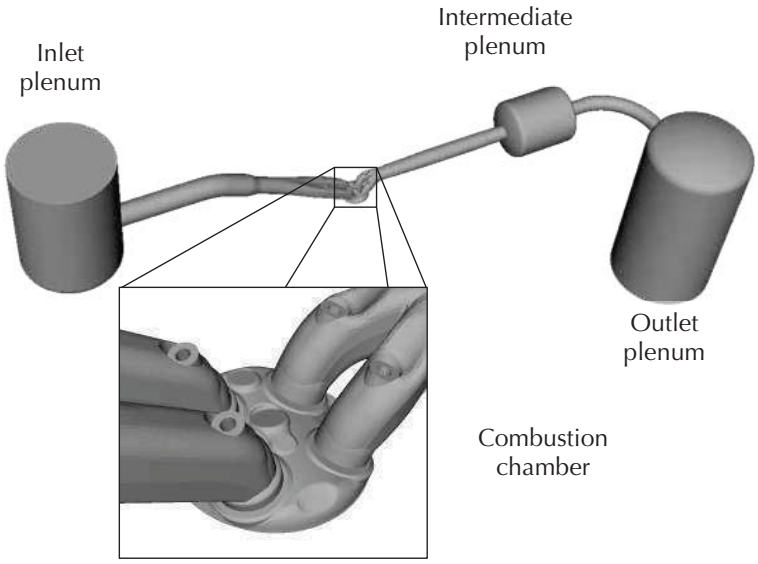

Figure 3: Sketch of the experimental Ecosural engine test bench.

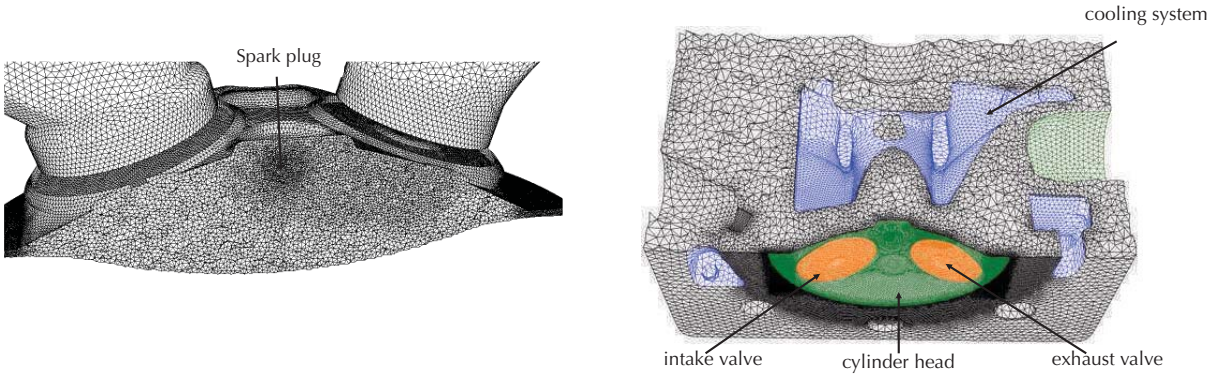

Figure 4: Illustration of a typical mesh for the LES simulation (left) and for the CHT simulation (right).

	Symbol	Unity	Cast iron	steel
Density	ρ	$[kg/m^3]$	2675	7500
Heat capacity	Cp	$[J/(kg.K)]$	900	450
Heat conductivity	λ	$[W/(m.K)]$	100	36

Table 1: Properties of the materials used in the CHT simulation.

	Unity	
Compression ratio	-	10.64
Bore	[mm]	77
Stroke	[mm]	85.8
Connecting rod length	[mm]	132.2
IVO/IVC	[CAD]	353/-162
EVO/EVC	[CAD]	142.5/-352.5

Table 2: Main engine specifications. Crank Angle Degrees (CAD) are relative to combustion top dead center. IVO and IVC respectively stand for Inlet Valve Opening and Closure while EVO and EVC stand for Exhaust Valve Opening and Closure.

	Unity	
Engine rotation speed	[rpm]	1800
IMEP	[bar]	19
Intake pressure	[bar]	1.8
Intake temperature	[K]	308
Fuel	[-]	C_8H_{18}

Table 3: Definition of the operating point chosed in the ICAMDAC database to study the knocking phenomena. IMEP stands for Indicated Mean Effective Pressure.

The engine geometrical specifications (Tab. 2) and the operating point described in Tab. 3 correspond to the knocking conditions. For this regime, the dynamics of the flow predicted by LES were validated against PIV measurements [33].

3. Conjugate heat transfer simulation

All LES of piston engines require the specification of the wall temperatures. In the present work, two methods were used to obtain these quantities:

- the usual method is to assume that (1) the chamber walls can be decomposed in isothermal elements: piston head, intake, exhaust valves and (2) the temperature of these elements is known, usually obtained either through a global energy balance or through empiric evaluations (this method is called *empirical* here).
- the CHT method where heat transfer in the walls (cylinder head and valves) is coupled to LES to obtain the skin wall temperature by a fully coupled simulation (called *CHT* here).

Note that in the *empirical* approach, the elements temperatures are often tuned to match experimental observations (volumetric efficiency, heat losses, etc.). Here we use the wall temperatures proposed for the same engine by [34] (Tab. 4). For the *CHT* approach, walls temperatures are a result of the computation and not an input data.

During one cycle the diffusion through the cylinder head and valves is actually not steady because of moving parts, of the unsteadiness of fluid dynamics and of the intermittency of

Patch	Temperature [K]
Cylinder head	409
Intake valves	639
Exhaust valves	784

Table 4: Skin wall temperatures obtained from 0D simulations used for the *empirical* simulation [34].

combustion. For instance, for an engine cycle of 720 CA, the heat flux to the exhaust valve is high during combustion and exhaust phases while it is low during the intake stroke because of the low temperature of the fresh gases. In practice, however, because of the difference in characteristic times between heat diffusion inside the solid and flow motion in the cylinder, the solid acts as a low-pass filter and receives a heat flux coming from the fluid domain which can be averaged over the whole engine cycle, allowing to decouple LES and heat transfer codes. The most significant complexity for the CHT method is the description of the diffusive heat fluxes between valves and cylinder head. When valves are closed, heat can diffuse from the valve to the cylinder head depending on the heat resistance of the contact zones between valves and cylinder head which is controlled by the force of the valve spring [1]. On the other hand in the open position, no thermal exchange can occur between the valve seat and the cylinder head. This geometry change has proved to be a major difficulty for the CHT approach because it controls the exhaust valve temperature and therefore the onset of knocking. The first part of this paper (Sec. 3.1) assumes that during the whole engine cycle, valves remain in the closed position as far as heat fluxes in the engine walls in concerned. This assumption clearly over-estimates the exhaust valve cooling and leads to lower temperatures. This problem is addressed in Sec. 3.4.

3.1. Heat transfer cycle-to-cycle variability

In spark ignited piston engines RMS pressures due to Cycle-to-Cycle Variability can reach several percents of the mean in-cylinder pressure. Cycle to cycle variability can also affect heat fluxes through the walls. In order to evaluate the variability of heat fluxes, Fig. 5 shows the value of the total flux to the cylinder head (valves are not included) obtained from LES for 15 consecutive engine cycles with the *empirical* approach and reveals a significant variability. For engine cycles where the whole mixture is burned quickly, pressure and temperature in the cylinder are high and increase thermal exchanges at the boundaries leading to large and variable fluxes during the combustion phase. However, Fig. 5 also shows that the main flux from the fluid to the cylinder head occurs during the exhaust stroke when the cylinder is filled with hot gases and high velocities caused by the exhaust valve opening. For this engine, all the fuel is consumed when the exhaust valves open, so that the temperature inside the cylinder is almost the same for all cycles. Even though the instantaneous flux to the cylinder head varies from cycle to cycle (Fig. 5), its value averaged over each cycle exhibits much less variation (Fig. 6). To evaluate the impact of these variations on combustion, the engine cycle showing the highest heat fluxes and the engine cycle with the lowest heat fluxes were used as boundary conditions for a HT simulation inside the solid domain. The converged solution on the skin at the interface between fluid and solid domains is displayed in Fig. 7 for those

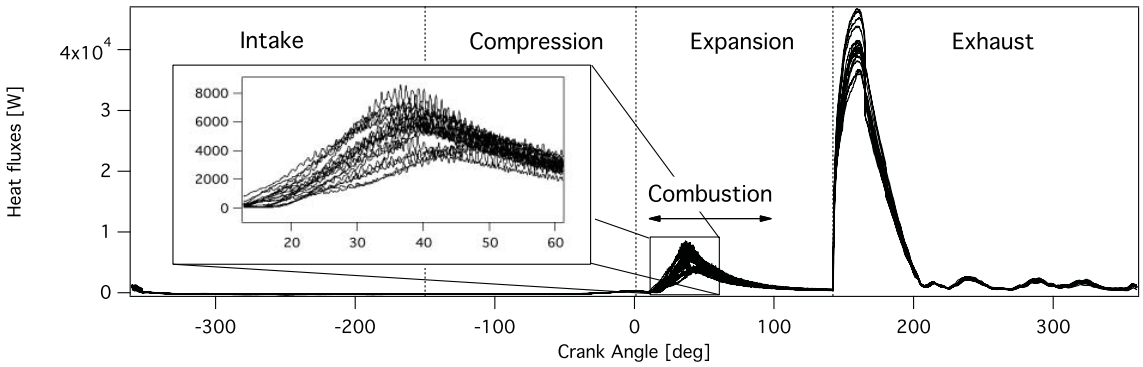

Figure 5: Heat fluxes through the cylinder head during 15 consecutive cycles.

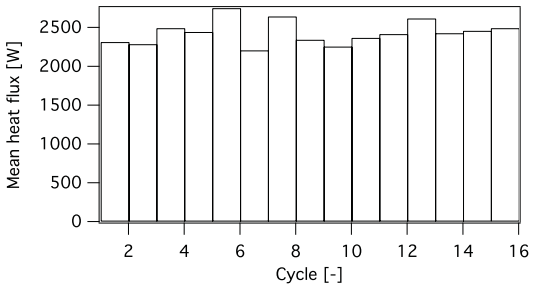

Figure 6: Mean heat flux between the cylinder head and the fluid integrated over each engine cycle.

two engine cycles. Even though these two cycles represent extreme scenarios in terms of

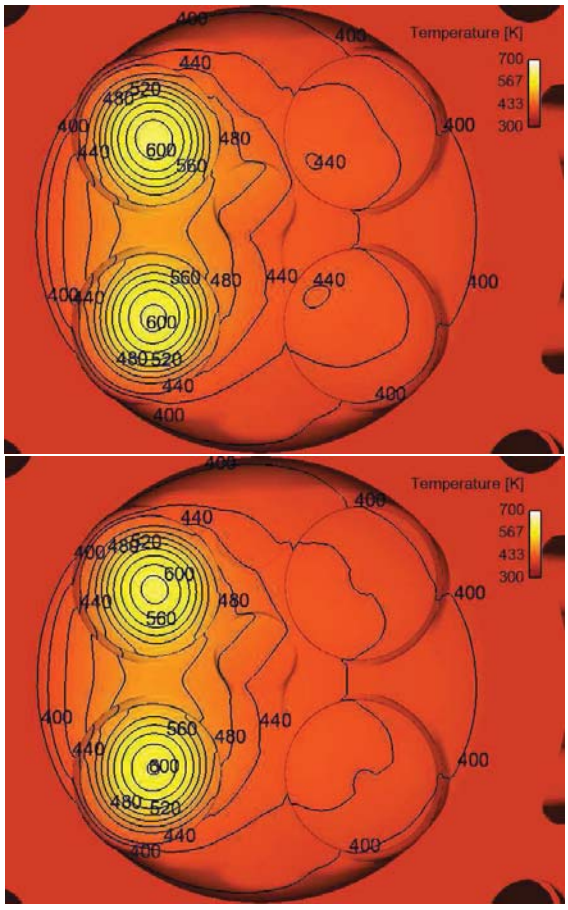

Figure 7: Converged temperature on the solid skin after the first CHT iteration. (a) engine cycle with the highest mean heat transfer and (b) engine cycle with the lowest heat transfer.

fluid-solid heat fluxes, these HT simulations show that the impact on the solid temperature is very low. The mean temperature integrated over the cylinder head and valves is 441 K for the engine cycle with the highest heat fluxes while it is equal to 438 K for the engine cycle with the lowest heat fluxes. As expected, the highest temperatures are found on the exhaust valves but they vary only from 607K for the low flux cycle to 611 K for the high flux cycle. In other words, temperature in the solid is mainly driven by heat exchanges with the ambient air and coolant fluid and its sensitivity to variations of the heat flux coming from the fluid domain is low. This shows that the temperature field in the engine walls is almost insensitive to the details of each cycle and can be computed using the cycle averaged heat fluxes. Note that for the two simulations performed, steady state is reached after about 60 s of physical time meaning that a synchronized coupling between fluid and solid domains is actually out of reach for this kind of applications.

3.2. CHT convergence and influence on the fluid solution.

Figure 8 shows the evolution of the mean solid temperature and the mean heat fluxes integrated over the cylinder head and valves using the algorithm of Fig. 1. Convergence is

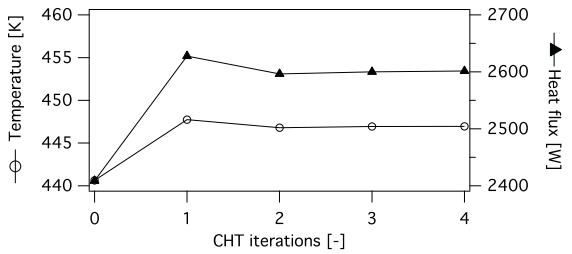

Figure 8: Convergence of the mean temperature and heat fluxes at the interface between the fluid and solid domains.

reached very quickly: at the end of the second CHT iteration, the error compared to the fourth CHT iteration on the mean heat flux is 0.2% and 0.3% on the mean temperature. Figure 9 shows the evolution of the skin temperature used as boundary condition for the LES. The quick convergence of the CHT simulation observed for global quantities in Fig. 8 is also observed for the local distribution of the wall temperature. The main advantage of using a CHT methodology is to provide the full wall temperature field while the *empirical* simulation relies on a user-specified mean temperature for each element of the model (cylinder head, valves). For a more quantitative comparison, temperature profiles on cylinder head and valves (see Fig. 9.b for profile positions) are plotted in Fig. 10. These profiles prove that it is difficult to obtain good estimations of wall temperature with *empirical* guess. Up to 60 K variations of temperature are observed on the center of the cylinder head (A-line in Fig. 10.a). This is even worse for exhaust valves where the skin temperature at the exhaust valve center is 200 K higher than its surroundings (B-line in Fig. 10.b). The exhaust valve shaft only sees burned gases during the whole engine cycle. On the contrary, the valve tip is cooled down by the cylinder head. The resulting temperature profile in the valve can not be guessed using *empirical* approaches and *CHT* is required to provide consistent temperature fields for LES.

3.3. Impact of CHT on combustion

In order to investigate the effect of using realistic wall temperatures, a first multi-cycle LES is performed with *empirical* wall temperatures. Then each individual cycle is re-played with different wall temperatures from *CHT* simulations. Table 5 summarize the different cases. Figure 11 shows the pressure evolution for 3 engine cycles with highing knock intensity in *A-case* and *B-case*. In both experiments and LES, knocking cycles are characterized by pressure oscillations: pressure records are used to determine the occurrence of knocking and its onset. For a fair comparison between experiments (where 500 cycles are captured) and LES (which only contains 15 cycles) samples of 15 experimental cycles are used to compute the same statistics (Tab. 6). These statistics show that the numerical setup including TFLES and IPRS model for combustion modeling is able to reproduce the knocking behavior in the

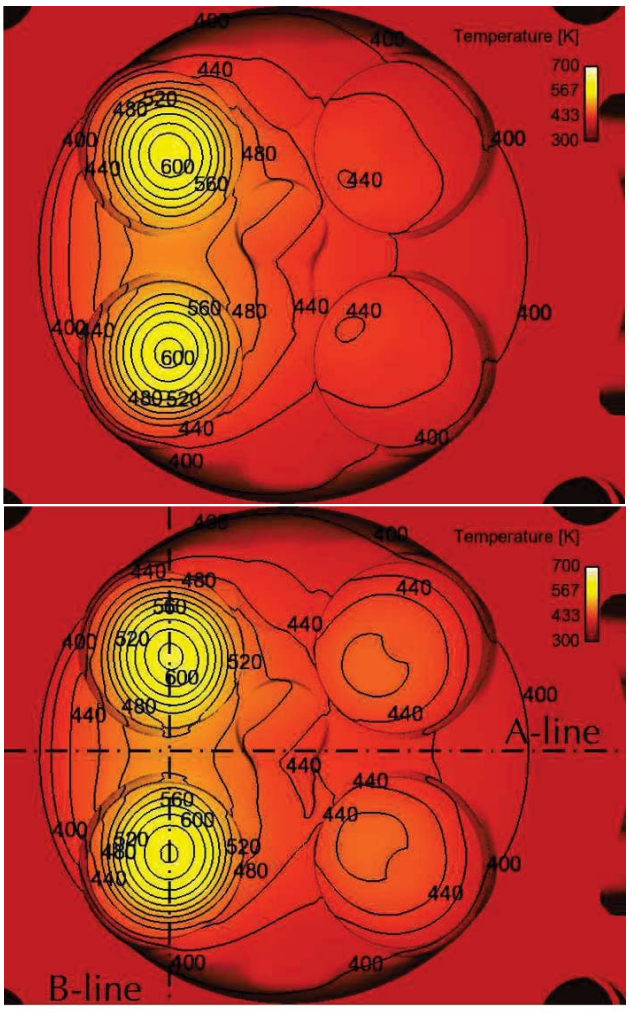

Figure 9: Convergence of the CHT simulation. (a) Converged solution in the solid after the first CHT iteration and (b) converged solution after the fourth CHT iteration.

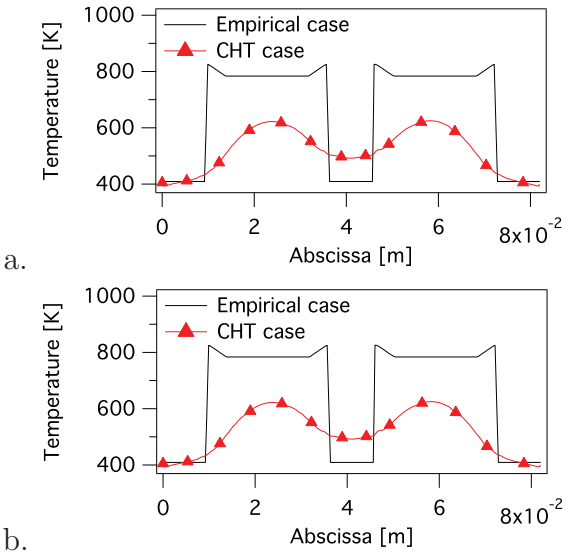

Figure 10: Temperature profiles on cylinder head and exhaust valves for *empirical* and *CHT*. A-line (a) and B-line (b). The *empirical* profiles are specified by the user as boundary condition while the *CHT* profiles are a result of the coupled simulation.

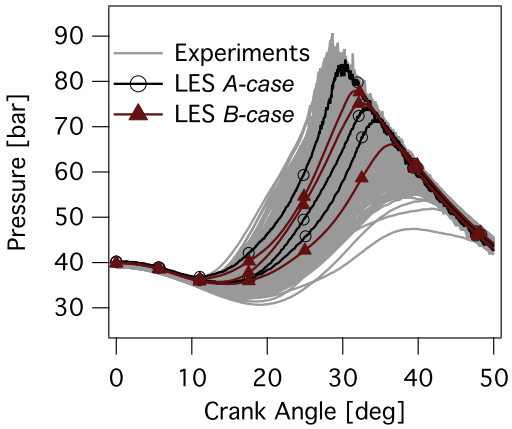

Figure 11: Temporal evolution of the in-cylinder pressure recorded by a pressure probe for 3 engine cycles with high knocking intensity. (a) corresponds to *A-case* and (b) corresponds to *B-case*.

Case	Spark Timing [CAD]	Wall Temperature	Nu_c	Knocking
A-case	+6	*Empirical*	-	Yes
B-case	+6	*CHT*	0.3	No
C-case	+6	*CHT*	0.6	Yes
D-case	0	*CHT*	0.6	Yes
E-case	-4	*CHT*	0.6	Yes

Table 5: Definition of LES cases. Spark timing is given with reference to TDC.

	Knocking cycles [%]	Knock onset [CA aTDC]
Exp. (500 cycles)	51.51	31.61
Exp. (15 cycles)	[13.34-80.0]	[29.91-35.24]
LES *A-case*	40.0	32.56
LES *B-case*	0	-
LES *C-case*	53	32.9

Table 6: Comparison of knocking statistics between experiments and LES.

A-case. For the *B-case* simulation however, no knocking cycles are observed. The cycles plotted are the same for the two cases. The combustion process differs between the two simulations even during the propagation of the flame but the most remarkable result is that in *B-case*, no oscillations representative of knocking are observed. The difference in the combustion process can be attributed to slight changes due to the different temperature of the walls. These skin temperature differences induce not only gas temperature differences but also flow modifications (Fig. 12): the combination of temperature and flow variations between *A* and *B-Cases* eventually leads to very different knocking results. Under the same

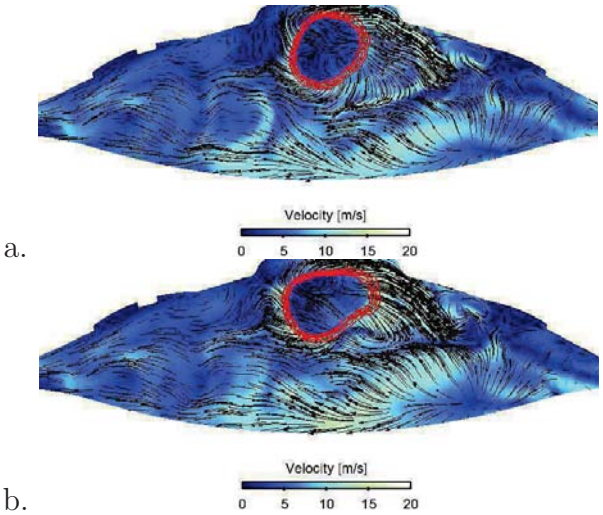

Figure 12: Aerodynamic field in a $(\vec{x}, \vec{z})$ cut-plane and iso-surfaces of temperature 2 CAD after ignition for *A-case* (a) and *B-case* (b). This cycle corresponds to the cycle with the highest knocking intensity for *A-case*.

operating conditions, [34] observed that auto-ignition of the end-gas mainly occured near hot exhaust valves. In the present results, the absence of knocking in *B-case* is indeed due to the lower exhaust valve temperature compared to *A-case*. In *A-case*, the exhaust valve temperature was set to 784K while it shows large local variations in the CHT simulation but does not exceed 620K (Fig. 9 and 10). Figure 13 shows iso-surfaces of temperature at 780K and 800 K for the same cycle as in Fig. 12, 2 CAD after ignition for the *empirical* (*A-case*) and the CHT (*B-case*) LES. The distribution of hot spots clearly differs between the two

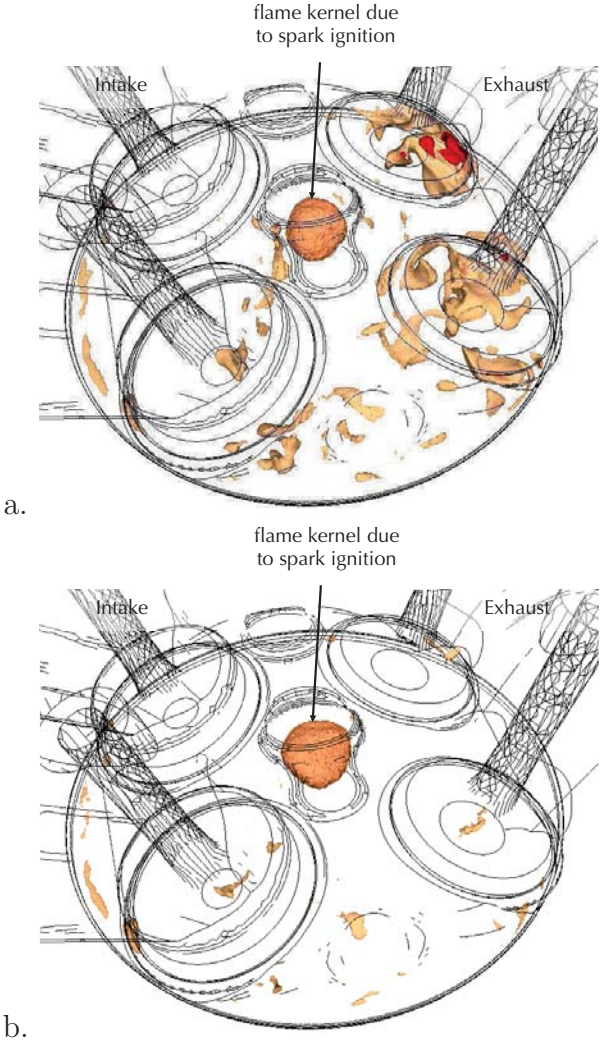

Figure 13: 780K and 800K temperature iso-surfaces 2 CAD after spark timing for the cycle with highest knock intensity in *A-case* (a) and *B-case* (b). This cycle corresponds to the cycle with the highest knocking intensity.

simulations and more particularly, the large hot spot observed above the hot exhaust valve in *A-case* disappears in *B-case*. This zone corresponds to the location where auto-ignition eventually occurs in *A-case* explaining why *B-case* does not create knocking. This simulation shows that autoignition is extremely sensitive to local temperature properties: improving

the boundary conditions (going from an empirical temperature field to a fully computed temperature field) on the engine walls is sufficient to inhibit knocking. This confirms that wall boundary conditions are crucial to predict knocking. Even if the CHT methodology provides a better description of wall temperatures, it actually degrades knocking predictions because it lead to too low temperature of the exhaust valves. It suggests that the CHT approach used in this section must be improved. The next section shows that the most critical part of this method is the description of the contact between exhaust valves and cylinder head.

3.4. Improvement of the CHT model.

This section shows how to improve the CHT approach and capture knocking when it should occur. For the sake of simplicity, the model previously used for the CHT simulation assumed:

- a closed position of the valves during the whole cycle;
- no contact resistance between cylinder head and valves when valves are closed.

These assumptions have a major impact on heat fluxes between cylinder head and exhaust valves. The main problem is that assuming closed position and perfect contact between head and valves during the whole cycle over-predicts the cooling of the hot valves by the water-cooled cylinder head. The heat flux in this region actually follows a cyclic evolution: it is high when the valve is closed and it is zero when the valve is open. The typical exhaust phase duration is 200 CAD which represents 28% of the whole cycle. Heat diffusion inside the solid does not see the valve motion because of its high frequency but this motion has an impact on the mean fluxes through the cylinder head-valve interface. This section describes a simple improvement technique to account for the reduced valve heat fluxes due to the period when valves are open and to the contact resistance between the two parts. The flux Φ between cylinder head and valve can be expressed as follows:

$$\Phi = \tau_{closed} \frac{T_h - T_v}{R_c} \tag{3}$$

with τ_{closed} the ratio between the duration when the valve is closed to the cycle duration (τ_{closed}=0.3). T_h and T_v represent the cylinder head and valves temperature and R_c is the contact resistance R_c between head an valves. Eq. 3 suggests a simple method (called here *fictitious layer*) to account for the reduced heat flux due to contact resistance and valve opening without having to actually use a geometry where the valves move. A small 'contact' zone of thickness e ($e = 0.3mm$ here) and conductivity $\lambda_{contact}$ (Fig. 14) can be placed between valves and cylinder head. The conductivity $\lambda_{contact}$ can be chosen so that the heat flux through this layer $\Phi_{contact} = \lambda_{contact}.(T_h - Tv)/e$ matches the flux given in Eq. 3. This is obtained for: $\lambda_{contact} = \tau_{closed}.e/R_c$. It is convenient to scale $\lambda_{contact}$ by the conductivity of the valves to have:

$$\frac{\lambda_{contact}}{\lambda_{valves}} = \frac{\tau_{closed}}{Nu_c} \tag{4}$$

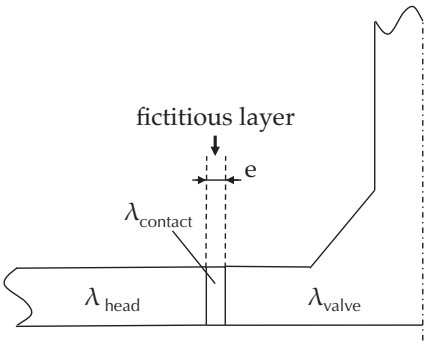

Figure 14: Illustration of the fictitious layer model to account for teat transfer between cylinder head and valves.

where Nu_c is a contact Nusselt number. This allows to mimic the effect of valve opening on the valve temperature while still using a fixed geometry. Nu_c is difficult to evaluate and remains an input for the simulation. In the following (*C-case*, *D-case* and *E-case*) it is set to $Nu_c = 0.6$. For *B-case* where the layer of thickness e was supposed to be made of steel, Nu_c is equal to $\tau_{closed} = 0.3$ by construction.

The convergence of this modified CHT simulation is displayed Fig. 15. As in the previous

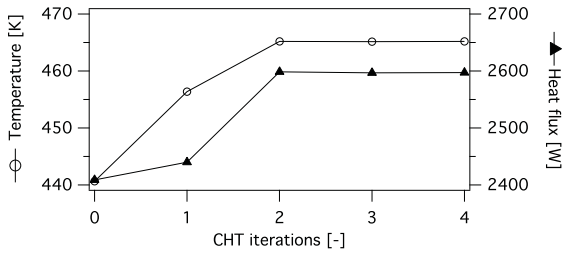

Figure 15: Convergence of the mean temperature and heat fluxes at the interface between the fluid and solid domains with $Nu_{contact} = 0.6$.

case, a steady state in terms of mean temperature and mean heat flux is obtained after the second CHT iteration. Fig. 16 shows the spatial distribution of temperature after the fourth CHT iteration. Compared to the *B-case* simulation (Fig. 9.b) higher temperatures are observed. The temperature of the exhaust valve center increases from 605K to 690K. It is interesting to see that, once one tries to compute wall temperatures with precision, details become important: the present results show that assuming that valves remain closed all the time leads to under predicted wall temperatures and, as shown above, to underestimated knocking. Correcting this problem with the model of Fig. 14 and Eq. 4 is sufficient to capture knocking cycles again: for a third multi-cycle simulation called *C-case*, 53% of knocking cycles are found with a mean onset at 32.9 CAD which matches experimental results (Fig. 17).

Finally, the same wall temperatures (from *C-case*) are kept to compute *D-case* and *E-case* with variable spark timing. Figure 18 shows the evolution of the local pressure for three knocking cycles with high knocking intensity. The global trends from [34] are retrieved.

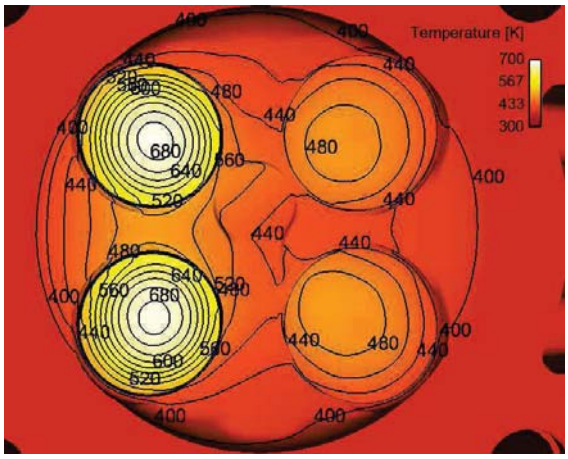

Figure 16: Temperature field at the fluid/solid interface after the fourth CHT iteration.

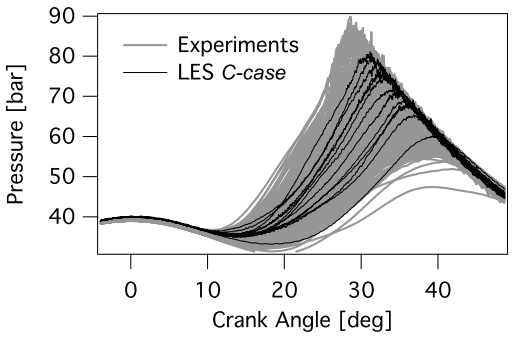

Figure 17: Temporal evolution of the in-cylinder pressure recorded by a pressure probe in *C-case*(15 cycles).

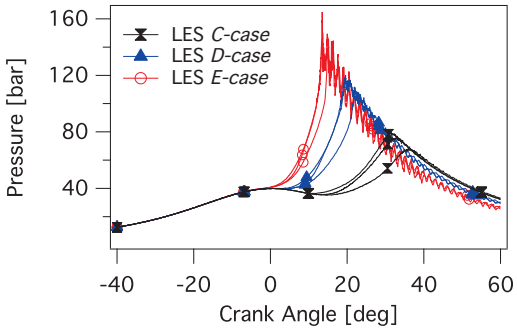

Figure 18: Temporal evolution of the in-cylinder pressure for 3 cycle with high knocking intensity for *C-case*, *D-case* and *E-case*.

When the spark timing is reduced, higher pressure levels are observed inside the cylinder. Auto-ignition occurs sooner in the cycle and knocking intensity is increased.

These simulations show that wall temperatures have a direct impact on the flow motion and on the combustion process. Especially when dealing with abnormal combustions, the auto-ignition delay can vary dramatically as a function of the local temperature conditions and an accurate prediction of the thermal boundary conditions is necessary. Even though the proposed model including a CHT simulation still uses some assumptions such as the definition of a contact Nusselt number, it replaces a complete field of uncertainties (the wall temperature field) by only one input (the contact Nusselt number). This permits to obtain local distributions of temperature that should be close to the physical behavior and compatible with LES precision.

4. Conclusions

In order to increase the precision of LES of knocking in piston engines, this paper focuses on a strategy that permits to access to a realistic wall temperature field in the combustion chamber. The proposed methodology relies on a full Conjugate Heat Transfer (CHT) simulation between cylinder head, valves and the combustion chamber which provides all wall temperatures. These temperatures control the engine behavior, especially in terms of knocking showing the importance of this input for precise LES. The second part of this paper addresses the issue of heat transfer between cylinder head and moving valves. A simple methodology is proposed to account for this moving geometry and contact resistance in this region. LES simulations are then performed with these realistic temperature field and experimental knocking behaviors are retrieved.

5. Aknowledgments

This work was granted access to the HPC resources of CCRT under allocations x20142b5031 made by GENCI (Grand Equipement National de Calcul Intensif) and PRACE (Partnership for Advance Computing in Europe) project N2013091887 SolitonCycLES. The authors acknowledge the financial support by the French ANR under grant ANR-10-VPTT-0002 ICAMDAC.

References

[1] Aabdel-Fattah, Y. 2009 The mechanics of valves cooling in internal-combustion engines: Investigation into the effect of valve-seat inserts on the heat flow from valves towards the cooling jacket. Phd thesis, University of Bradford.

[2] Ball, George A. 1955 Photographic studies of cool flames and knock in an engine. *Proc. Combust. Inst.* **5** (1), 366–372.

[3] Bradley, D. & Kalghatgi, G. T. 2009 Influence of autoignition delay time characteristics of different fuels on pressure waves and knock in reciprocating engines. *Combust. Flame* **156** (12), 2307–2318.

[4] Butler, T. D. & O'Rourke, P. J. 1977 A numerical method for two-dimensional unsteady reacting flows. *Proc. Combust. Inst.* **16** (1), 1503 – 1515.

[5] Chun, K. M. & Heywood, J. B. 1989 Characterization of knock in a spark-ignition engine. *SAE paper* (890156).
[6] Clavin, P. & He, L. 1996 Stability and nonlinear dynamics of one-dimensional overdriven detonations in gases. *J. Fluid Mech.* **306**, 353–378.
[7] Colin, O. & Rudgyard, M. 2000 Development of high-order Taylor-Galerkin schemes for unsteady calculations. *J. Comput. Phys.* **162** (2), 338–371.
[8] Donea, J. & Huerta, A. 2003 *Finite element methods for flow problems*. John Wiley & Sons.
[9] Duchaine, F., Maheu, N., Moureau, V., Balarac, G. & Morea, S. 2013 Large-eddy simulation and conjugate heat transfer around a low-mach turbine blade. *Journal of Turbomachinery* **136** (5), 051015–051015.
[10] Enaux, B., Granet, V., Vermorel, O., Lacour, C., Pera, C., Angelberger, C. & Poinsot, T. 2011 LES and experimental study of cycle-to-cycle variations in a spark ignition engine. *Proc. Combust. Inst.* **33**, 3115–3122.
[11] Fieweger, K., Blumenthal, R. & Adomeit, G. 1997 Self-ignition of s.i. engine model fuels: A shock tube investigation at high pressure. *Combust. Flame* **109** (4), 599–619.
[12] Frayssé, V., Giraud, L., Gratton, S. & Langou, J. 2005 Algorithm 842: A set of GMRES routines for real and complex arithmetics on high performance computers. *ACM Trans. Math. Softw.* **31** (2), 228–238.
[13] Gicquel, L. Y. M., Staffelbach, G. & Poinsot, T. 2012 Large eddy simulations of gaseous flames in gas turbine combustion chambers. *Progress in Energy and Combustion Science* **38** (6), 782–817.
[14] Granet, V., Vermorel, O., Lacour, C., Enaux, B., Dugué, V. & Poinsot, T. 2012 Large-eddy simulation and experimental study of cycle-to-cycle variations of stable and unstable operating points in a spark ignition engine. *Combust. Flame* **159** (4), 1562–1575.
[15] Granet, V., Vermorel, O., Leonard, T., Gicquel, L., & Poinsot, T. 2010 Comparison of nonreflecting outlet boundary conditions for compressible solvers on unstructured grids. *AIAA Journal* **48** (10), 2348–2364.
[16] Hirt, C. W., Amsden, A.A. & Cook, J. L. 1974 An arbitrary lagrangian-eulerian computing method for all flow speeds. *J. Comput. Phys.* **131** (4), 371–385.
[17] Kalghatgi, G. T. 1995 Combustion chamber deposits in sparkignition engines – a literature review. *SAE -Transactions–J Fuels and Lubricants* **105** (952443).
[18] Kanti, M., Kawahara, N. & Tomita, E. 2010 Visualization of knocking combustion in a hydrogen spark-ignition engine. *Proc. World Hydrogen Energy Comb.* **78** (6).
[19] Kawahara, N., Tomita, E. & Sakata, Y. 2007 Auto-ignited kernels during knocking combustion in a spark-ignition engine. *Proc. Combust. Inst.* **31** (2), 2999–3006.
[20] K.Chun, Heywood, J.B. & Keck, J.C. 1989 Prediction of knock occurrence in a spark-ignition engine. *Proc. Combust. Inst.* **22** (1), 455–463.
[21] Lacaze, G., Richardson, E. & Poinsot, T. J. 2009 Large eddy simulation of spark ignition in a turbulent methane jet. *Combust. Flame* **156** (6), 1993–2009.
[22] Lax, P. D. & Wendroff, B. 1964 Difference schemes for hyperbolic equations with high order of accuracy. *Com. Pure App. Math.* **17**, 381–398.
[23] Lefebvre, A. H. 1999 *Gas Turbines Combustion*. Taylor & Francis.
[24] Li, Y. & Kong, S.C. 2011 Coupling conjugate heat transfer with in-cylinder combustion modeling for engine simulation. *Int. J. Heat and Mass Transfer* **54** (11–12), 2467–2478.
[25] Linse, D., Kleemann, A. & Hasse, C. 2014 Probability density function approach coupled with detailed chemical kinetics for the prediction of knock in turbocharged direct injection spark ignition engines. *Combust. Flame* **161** (4), 997–1014.
[26] Litzinger, T. 1990 A review of experimental studies of knock chemistry in engines. *Prog. Energy Comb. Sci.* **16** (3), 155–167.
[27] Misdariis, A., Robert, A., Vermorel, O., Richard, S. & Poinsot, T. 2014 Numerical methods and turbulence modeling for LES of piston engines: Impact on flow motion and combustion. *Oil Gas Sci. Technol. – Rev. IFP Energies nouvelles* **69** (1), 83–105.

[28] Misdariis, A., Vermorel, O. & Poinsot, T. 2015 A methodology based on reduced schemes to compute autoignition and propagation in internal combustion engines. *Proc. Combust. Inst.* **35** (3), 3001–3008.

[29] Pera, C. & Angelberger, C. 2011 Large eddy simulation of a motored single-cylinder engine using system simulation to define boundary conditions: Methodology and validation. *SAE paper* (2011-01-0834).

[30] Peters, N., Kerschgens, B. & Paczko, G. 2012 Super-knock prediction using a refined theory of turbulence. *SAE paper* (2013-01-1109).

[31] Poinsot, T. & Lele, S. 1992 Boundary conditions for direct simulations of compressible viscous flows. *J. Comput. Phys.* **101** (1), 104–129.

[32] Richard, S., Colin, O., Vermorel, O., Benkenida, A., Angelberger, C. & Veynante, D. 2007 Towards large eddy simulation of combustion in spark ignition engines. *Proc. Combust. Inst.* **31**, 3059–3066.

[33] Robert, A. 2014 Simulation aux grandes echelles des combustions anormales dans les moteurs downsizés à allumage commandé. Phd thesis, INP Toulouse.

[34] Robert, A., Richard, S., Colin, O., Martinez, L. & Francqueville, L. De 2015 {LES} prediction and analysis of knocking combustion in a spark ignition engine. *Proceedings of the Combustion Institute* **35** (3), 2941 – 2948.

[35] Schønfeld, T. & Poinsot, T. 1999 Influence of boundary conditions in LES of premixed combustion instabilities. In *Annual Research Briefs* , pp. 73–84. Center for Turbulence Research, NASA Ames/Stanford Univ.

[36] Smagorinsky, J. 1963 General circulation experiments with the primitive equations: 1. the basic experiment. *Mon. Weather Rev.* **91**, 99–164.

[37] Zeldovich, Y. B. 1980 Regime classification of an exothermic reaction with nonuniform initial conditions. *Combust. Flame* **39** (2), 211–214.

Partie III

Conclusion

CHAPITRE 9

Conclusion générale

La modélisation de la combustion dans les moteurs à piston est un domaine d'application particulier pour la LES: à cause du mode de fonctionnement instationnaire du moteur et de la nécessité d'avoir un nombre de cycles suffisamment grand pour être représentatif du fonctionnement moteur, des temps physiques importants doivent être simulés. Les modèles de combustion doivent reproduire les différentes phases de la combustion: l'allumage puis la phase de croissance laminaire du noyau et la transition vers la propagation pleinement turbulente du front de flamme ainsi que l'auto-allumage dans certains cas. Le temps de résidence des gaz frais dans la chambre de combustion est important avant la combustion du mélange, ce qui accroit l'importance des transferts thermiques à la paroi et leur effet sur les conditions thermodynamiques locales. Pour cette raison, il est important d'utiliser des températures de paroi réalistes pour avoir un état gaz frais réaliste. Différentes études, réalisées avant cette thèse ont mis en place des méthodologies de calcul pour reproduire la combustion dans des moteurs automobiles (Moureau, 2004; Richard, 2005; Thobois, 2006; Vermorel *et al.*, 2007; Enaux, 2010; Enaux *et al.*, 2011*b*; Pera & Angelberger, 2011; Granet, 2011). Ces différentes études ont montré la pertinence et la fiabilité de cette méthodologie LES en permettant notamment de reproduire l'aérodynamique et la combustion dans plusieurs configurations moteur différentes, en particulier les moteurs expérimentaux XU-10 et F7P.

Les travaux présentés dans cette thèse ont eu pour objectif d'améliorer cette méthodologie: (1) en utilisant des schémas numérique plus précis, (2) en ajoutant la possibilité de prédire l'auto-allumage dans le cas de cliquetis et (3) en proposant une méthode pour décrire précisément les températures de parois. Un travail important de développement de modèles a donc tout d'abord été nécessaire pour répondre à ces objectifs:

– le premier point traité a été l'amélioration de la précision des méthodes numériques utilisées. Ce point est critique dans les simulations de moteurs à piston où un temps physique important (de l'ordre de quelques secondes) doit être simulé, ce qui rend l'utilisation de schémas précis pénalisante en termes de coûts de calculs et de temps de restitution. En se basant sur une comparaison de différentes méthodologies numériques, la première étude de cette thèse a permis de montrer que l'utilisation de schémas d'ordre plus élevé uniquement pendant la phase de combustion permet d'améliorer la précision des résultats et diminue le poids des modèles de sous maille. La méthodologie alors proposée, nommée ESO_2, est de conserver un schéma numérique d'ordre faible pendant les phases aérodynamiques et de n'utiliser les schémas plus précis uniquement lorsque la combustion

a lieu.

- le second développement important réalisé dans cette thèse est le modèle d'auto-allumage: pour prédire l'apparition des combustions anormales, prédire la propagation de la flamme est nécessaire mais insuffisant. Il faut également que la modélisation de la combustion soit capable de rendre compte des délais d'auto-allumage. Pour des raisons de simplicité et de continuité avec les études précédentes, le choix a été d'utiliser le modèle de combustion turbulente de flamme épaissie et de décrire la cinétique chimique à l'aide d'un schéma réduit à deux étapes. Pour prédire le délai d'auto-allumage avec cette méthodologie, un nouveau modèle a été développé. En modifiant les constantes des loi d'Arrhénius (utilisées pour exprimer le taux de réaction) à basse température uniquement, ce modèle appelé IPRS permet de reproduire le délai d'auto-allumage en plus de la propagation de la flamme dans des configurations simples. Ce modèle permet également de retrouver les différents régimes de combustion après l'auto-allumage en fonction des conditions thermodynamiques locales dans une configuration mono-dimensionnelle présentant un gradient initial de température.
- enfin, sachant que l'auto-allumage est un phénomène très sensible aux conditions locales de température, une méthodologie permettant d'obtenir des températures de parois réalistes est proposée. Un couplage avec un code de thermique solide est mis en place pour rendre compte des transferts thermiques ayant lieu à l'interface entre le fluide et le solide. De cette façon, les températures de paroi fixées jusqu'à présent de manière empirique dans la LES sont remplacées par un champ de température représentatif des échanges entre le solide et le fluide.

En plus des temps de calculs importants, le fonctionnement instationnaire des moteurs à piston et les parties mobiles de la géométrie mobile rendent la mise en données complexe et coûteuse en temps humain. En plus des développement cités ci-dessus, cette thèse a également été l'occasion d'améliorer cette étape de pré-traitement. Premièrement, une approche de type frontières immergées a été appliquée pour prendre en compte des variations géométriques de la configuration (Annexe A). Alors que l'approche classique aurait nécessité de régénérer un jeu entier de maillages (40 environ), cette approche a permis de s'affranchir de cette étape coûteuse en temps humain. Deuxièmement, pour faciliter la génération des maillages, un outil de génération automatique a été créé. Grace à cet outil, environ une semaine a été nécessaire pour générer les maillages du moteur ECOSURAL alors que cette étape avait pris plusieurs mois dans le cas des calculs LES XU-10 et F7P précédents. Cet outil a ensuite été amélioré et pérennisé par l'*IFP Energies Nouvelles* pour être utilisé dans les futures études LES moteur.

Ces différents modèles et méthodologies ont ensuite permis d'étudier le cliquetis dans le moteur expérimental ECOSURAL installé à l'*IFP Energies Nouvelles* dans le cadre du projet ICAMDAC. Une première étude sur un point de fonctionnement à froid a permis de valider les résultats LES avec les mesures expérimentales de l'aérodynamique dans le cylindre. Les deux modèles de combustion disponibles pour la description des combustions anormales dans *AVBP* (*i.e.* CFM-TKI et TFLES-IPRS) ont ensuite été utilisés pour étudier plus en détails les combustions anormales. Dans une première étude, les modèles CFM-TKI ont été appliqués à deux points de fonctionnement de la base de données ICAMDAC. Ces simulations ont permis de comprendre certaines tendances au cliquetis difficiles à comprendre à l'aide des résultats expérimentaux uniquement. La seconde étude du cliquetis a été réalisée avec les modèles de combustion TFLES-IPRS et a permis de mettre en avant l'intérêt d'une représentation réaliste des températures de parois pour simuler les combustions anormales dans un moteur. La détermination de ce champ de température à l'interface fluide-solide est faite à l'aide d'un

couplage thermique entre le fluide et le solide. Cette étude a également mis en avant un second point qui est la difficulté de prédire les transferts thermiques entre les soupapes et la culasse. Une solution est proposée pour modéliser les transferts thermiques dans cette région et le champ de température à l'interface fluide-solide est utilisé pour de nouvelles simulations LES. La tendance au cliquetis prédite par la LES avec cette méthodologie est en bon accord avec les résultats expérimentaux.

En résumé, un grande partie de cette thèse a été consacrée au développement de méthodologies innovantes pour améliorer la précision ou pour rendre compte de nouveaux phénomènes physiques dans les simulations de moteurs à piston. Ces nouvelles méthodologies ont été appliquées avec succès à un moteur expérimental. Néanmoins certaines voies d'amélioration sont encore à investiguer:

- La motivation qui a poussé au développement du modèle IPRS a été de reproduire l'auto-allumage en conservant une description très simple de la chimie. Grâce à ce modèle, une seule formulation est utilisée pour décrire à la fois l'auto-allumage et la propagation de la flamme. Néanmoins, il permet de reproduire le comportement macroscopique de l'auto-allumage uniquement, *i.e.* le délai d'auto-allumage. Le chemin menant à l'auto-allumage n'est quant à lui pas reproduit par ce modèle. En particulier, la flamme froide présente dans certaines conditions n'est pas reproduite. Dans le cas présent de cliquetis, il semble que cette simplification n'a pas d'impact sur le comportement du moteur mais la flamme froide peut avoir un rôle plus important pour d'autres points de fonctionnement ou d'autres configurations. Il pourrait alors être intéressant d'améliorer le modèle IPRS pour accroître sa précision dans ce type de configurations.
- Le couplage thermique proposé permet de disposer de champs de température de parois réalistes pour la LES, là où des méthodes plus ou moins empiriques étaient utilisées avec pour seul objectif de reproduire des comportements globaux du moteur. La méthode proposée réduit la part des paramètres empiriques et permet donc d'accroître la précision des simulations mais nécessite toujours la spécification d'un paramètre pour caractériser la zone de contact entre les soupapes et la culasse. Pour s'affranchir de ce problème, une solution est de réaliser un couplage avec maillage mobile. En plus de la complexité accrue de ce type de couplage (nécessité de calculer à chaque itération les coefficients d'interpolation entre les noeuds fluides et le noeuds solides), le coût de calcul est aujourd'hui un obstacle important. En effet, reproduire les phases d'ouverture et fermeture des soupapes nécessite l'utilisation d'un couplage synchronisé et des simulations de plusieurs dizaines de secondes sont nécessaires pour atteindre un état convergé dans le solide. Le coût d'un tel calcul est donc aujourd'hui prohibitif.

Le travail réalisé dans cette thèse a donc permis d'améliorer certains points de la méthodologie existante pour la simulation de moteurs à piston. Il reste cependant certains aspects à traiter pour disposer d'un outil de simulation complet dans un contexte de moteurs à piston et en particulier l'aspect diphasique. Il parait, en effet, indispensable de disposer de modèles pour décrire l'injection de carburant sous forme d'un spray liquide mais également pour décrire les films liquides pouvant apparaitre lorsque le spray impacte le piston par exemple. Afin d'échelonner les difficultés, il a été choisi dans cette thèse de supposer le carburant totalement évaporé et un mélange parfaitement homogène au moment de la combustion. Mais cette hypothèse est une hypothèse très forte. Dans la pratique le mélange n'est pas parfait et les stratifications de richesse du mélange peuvent avoir un effet important sur la combustion. Pour répondre à ces questions, la thèse de N. Iafrate réalisée à l'*IFP Energies Nouvelles* a pour objectif de mettre au point les méthodologies et modèles nécessaires à la prise en compte de

l'injection directe dans les moteurs.

De manière plus générale, les outils développés dans cette thèse ne se limitent pas aux simulations de moteurs à piston. Le point le plus flagrant est l'étude de couplage, déjà largement utilisée dans le domaine aéronautique où le confinement de la flamme proche des parois nécessite de traiter les transferts thermiques pariétaux avec attention. De même, le modèle ESO_2 est, d'une certaine façon, déjà utilisé dans de nombreuse configurations où un premier calcul est généralement réalisé à l'aide de schéma numérique d'ordre réduit mais peu couteux pour passer la phase transitoire ('remplissage' d'une chambre de combustion de turbine à gaz par exemple) avant de changer de schéma numérique pour simuler la combustion de manière plus précise. Enfin, une perspective intéressante de ces travaux de thèse est l'application du modèle d'auto-allumage à certaines configurations où ce mode de combustion semble être présent. Par exemple, l'auto-allumage peut être à l'origine des phénomènes de flash-back dans les turbines à gaz à fort taux de compression (Lieuwen *et al.*, 2008). Diverses études ont montrées que le modèle de combustion TFLES permet de correctement modéliser la combustion dans ce type de configurations (Wolf *et al.*, 2009; Esclapez *et al.*, 2015). Dans ce contexte, le modèle IPRS pourra permettre d'ajouter la possibilité de prédire l'auto-allumage en conservant la même méthodologie de calcul.

Bibliography

Abdel-Gayed, R. G., Bradley, D., Hamid, M. N. & Lawes, M. 1984 Lewis number effects on turbulent burning velocity. *Proc. Combust. Inst.* **20**, 505–512. (Cited on page 159.)

Affleck, W. S. & Fish, A. 1968 Knock: Flame acceleration or spontaneous ignition? *Combustion and Flame* **12** (3), 243–252. (Cited on page 18.)

Alasfour, F. N. 1998 Nox emission from a spark ignition engine using 30% iso-butanol–gasoline blend: Part 2—ignition timing. *Applied Thermal Engineering* **18** (8), 609–618. (Cited on page 17.)

Amsden, A. A. 1997 KIVA-3: A KIVA program with block-structured mesh for complex geometries. *Tech. Rep.* UC-1412. (Cited on page 23.)

Bailly, C. & Comte-Bellot, G. 2003 *Turbulence*. CNRS Editions. (Cited on page 51.)

Ball, G. A. 1955 Photographic studies of cool flames and knock in an engine. *Symposium (International) on Combustion* **5** (1), 366–372. (Cited on page 15.)

Baum, M., Poinsot, T., Haworth, D. & Darabiha, N. 1994 Using direct numerical simulations to study $H_2/O_2/N_2$ flames with complex chemistry in turbulent flows. *J. Fluid Mech.* **281**, 1–32. (Cited on page 53.)

Baya Toda, H., Truffin, K. & Nicoud, F. 2010 Is the dynamic procedure appropriate for all SGS models? *Fifth European Conference on Computational Fluid Dynamics - ECCOMAS CFD* . (Cited on page 51.)

Boger, M. & Veynante, D. 2000 Large eddy simulations of a turbulent premixed v-shape flame. In *Advances in Turbulence VIII* (ed. C. Dopazo), pp. 449 – 452. Barcelona, Spain: CIMNE. (Cited on page 57.)

Bohbot, J., Gillet, N. & Benkenida, A. 2009 Un code parallèle non structuré pour la résolution des équations compressibles réactives avec spray. *Oil and Gas Science Tech. - Rev. IFP* **64** (3), 309–335. (Cited on page 23.)

Bonhomme, A. 2014 Numerical study of laminar and turbulent flame propagating in a fan-stirred vessel. Phd thesis, INP Toulouse. (Cited on pages 25, 231, 234, 235, 237 et 238.)

Borée, J., Maurel, S. & Bazile, R. 2002 Disruption of a compressed vortex. *Physics of Fluids* **14**, 2543–2556. (Cited on page 159.)

Bracewell, R. 1986 *The Fourier transform and its applications*. McGraw-Hill New York. (Cited on page 151.)

Bradley, D., Gaskell, P. H. & Gu, X. J. 1996 Burning velocities, Markstein lengths, and flame quenching for spherical methane-air flames: a computational study. *Combust. Flame* **104** (1/2), 176–198. (Cited on pages 20 et 24.)

Bradley, D. & Kalghatgi, G. T. 2009 Influence of autoignition delay time characteristics of different fuels on pressure waves and knock in reciprocating engines. *Combust. Flame* **156** (12), 2307–2318. (Cited on pages 105, 106, 107, 108 et 110.)

Braza, M., Chassaing, P. & Minh, H. Ha 1986 Numerical study and physical analysis of the pressure and velocity fields in the near wake of a circular cylinder. *Journal of Fluid Mechanics* **165**, 79–130. (Cited on page 237.)

Butler, T. D. & O'Rourke, P. J. 1977 A numerical method for two-dimensional unsteady reacting flows. *Proc. Combust. Inst.* **16** (1), 1503 – 1515. (Cited on pages 21 et 54.)

Butterworth, S. 1930 On the theory of filter amplifiers. *Wireless Engineer* **7**, 536–541. (Cited on page 151.)

Candel, S. M. & Poinsot, T. 1990 Flame stretch and the balance equation for the flame surface area. *Combust. Sci. Tech.* **70**, 1–15. (Cited on pages 21 et 57.)

CERFACS 2012 *AVBP Handbook - http://cerfacs.fr/∼ avbp/AVBP_V6.X/HANDBOOK*. CERFACS. (Cited on page 48.)

Charlette, F., Veynante, D. & Meneveau, C. 2002 A power-law wrinkling model for LES of premixed turbulent combustion: Part I - non-dynamic formulation and initial tests. *Combust. Flame* **131**, 159–180. (Cited on page 55.)

Chassaing, P. 2000 *Turbulence en mécanique des fluides, analyse du phénomène en vue de sa modélisation à l'usage de l'ingénieur*. Toulouse, France: Cépaduès-éditions. (Cited on page 90.)

Chun, K., Heywood, J. B. & Keck, J. C. 1989 Prediction of knock occurrence in a spark-ignition engine. *Symposium (International) on Combustion* **22** (1), 455–463. (Cited on page 15.)

Chun, K. M. & Heywood, J. B. 1989 Characterization of knock in a spark-ignition engine. *SAE paper* (890156). (Cited on page 18.)

Colin, O. 2000 Simulations aux grandes échelles de la combustion turbulente prémélangée dans les statoréacteurs. Phd thesis, INP Toulouse. (Cited on page 137.)

Colin, O., Benkenida, A. & Angelberger, C. 2003 3D modeling of mixing, ignition and combustion phenomena in highly stratified gasoline engine. *Oil and Gas Science Tech.* **58** (1), 47–62. (Cited on page 59.)

Colin, O., Ducros, F., Veynante, D. & Poinsot, T. 2000 A thickened flame model for large eddy simulations of turbulent premixed combustion. *Phys. Fluids* **12** (7), 1843–1863. (Cited on pages 54, 55 et 56.)

Colin, O., Pires da Cruz, A. & Jay, S. 2005 Detailed chemistry-based auto-ignition model including low temperature phenomena applied to 3-d engine calculations. *Proc. Combust. Inst.* **30** (2), 2649–2656. (Cited on pages 21, 23, 60 et 96.)

Colin, O. & Rudgyard, M. 2000 Development of high-order Taylor-Galerkin schemes for unsteady calculations. *J. Comput. Phys.* **162** (2), 338–371. (Cited on page 52.)

Colin, O. & Truffin, K. 2011 A spark ignition model for large eddy simulation based on an FSD transport equation (ISSIM-LES). *Proceedings of the Combustion Institute* **33** (2), 3097 – 3104. (Cited on page 147.)

Cook, A. 2013 Reserve growth of oil and gas fields—investigations and applications. *U.S. Geological Survey Scientific Investigations Report* **5063**, 29. (Cited on page 9.)

Corti, E., Cavina, N., Cerofolini, A., Forte, C., Mancini, G., Moro, D., Ponti, F. & Ravaglioli, V. 2014 Transient spark advance calibration approach. *Energy Procedia* **45** (0), 967–976. (Cited on pages 17 et 23.)

Dabireau, F. 2002 étude des transferts de chaleur aux parois dans les moteurs-fusées. Phd thesis, INP Toulouse. (Cited on page 119.)

Dahnz, C & Spicher, U 2010 Irregular combustion in supercharged spark ignition engines – pre-ignition and other phenomena. *International Journal of Engine Research* **11** (6), 485–498. (Cited on page 19.)

Davidson, D. F., Oehlschlaeger, M. A., Herbon, J. T. & Hanson, R. K. 2002 Shock tube measurements of iso-octane ignition times and oh concentration time histories. *Proc. Combust. Inst.* **29**, 1295–1301. (Cited on pages 96 et 97.)

Deardorff, J. 1970 A numerical study of three-dimensional turbulent channel flow at large reynolds numbers. *J. Fluid Mech.* **41**, 453–480. (Cited on page 51.)

D.G.Goodwin 2002 *Cantera C++ Users Guide*. http://sourceforge.net/pro jects/cantera. (Cited on page 53.)

Donea, J. & Huerta, A. 2003 *Finite element methods for flow problems*. John Wiley & Sons. (Cited on page 118.)

Dopazo, C. 1994 Recent developments in pdf methods. In *Turbulent Reacting Flows* (ed. P. A. Libby & F. A. Williams), pp. 375 – 474. London: Academic. (Cited on page 54.)

Downs, D. & Pignéguy, J. H. 1950 An experimental investigation into pre-ignition in the spark-ignition engine. *Proceedings of the Institution of Mechanical Engineers: Automobile Division* **4** (1), 125–149. (Cited on page 19.)

Duchaine, F., Corpron, A., Pons, L., Moureau, V., Nicoud, F. & Poinsot, T. 2009 Development and assessment of a coupled strategy for conjugate heat transfer with large eddy simulation: Application to a cooled turbine blade. *Int. J. Heat Fluid Flow* **30** (6), 1129–1141. (Cited on page 121.)

Duchaine, F., Maheu, N., Moureau, V., Balarac, G. & Moreau, S. 2013 Large-eddy simulation and conjugate heat transfer around a low-mach turbine blade. *Journal of Turbomachinery* **136** (5), 051015–051015. (Cited on page 118.)

Duclos, J. M., Veynante, D. & Poinsot, T. 1993 A comparison of flamelet models for premixed turbulent combustion. *Combust. Flame* **95**, 101–117. (Cited on page 159.)

Eckert, Peter, Kong, Song-Charng & Reitz, Rolf D 2003 Modeling autoignition and engine knock under spark ignition conditions. *Tech. Rep.*. SAE Technical Paper. (Cited on pages 21 et 23.)

Egerton, A. C. 1928 Engine knock and related problems. *Journal of the Franklin Institute* **206** (6), 871–872. (Cited on page 15.)

Enaux, B. 2010 Simmulation aux grandes échelles d'un moteur à allumage commandé - evaluation des variabilités cycliques. Phd thesis, Université de Toulouse - Ecole doctorale MEGeP. (Cited on pages 37, 62, 133, 181 et 209.)

Enaux, B., Granet, V., Vermorel, O., Lacour, C., Pera, C., Angelberger, C. & Poinsot, T. 2011*a* LES and experimental study of cycle-to-cycle variations in a spark ignition engine. *Proc. Combust. Inst.* **33**, 3115–3122. (Cited on pages 54, 97, 137 et 230.)

Enaux, B., Granet, V., Vermorel, O., Lacour, C., Thobois, L., Dugué, V. & Poinsot, T. 2011*b* Large eddy simulation of a motored single-cylinder piston engine: Numerical strategies and validation. , vol. 86, pp. 153–177. (Cited on pages 21, 56 et 209.)

Ern, A. & Giovangigli, V. 1994 *Multicomponent Transport Algorithms*. Heidelberg: Springer Verlag. (Cited on page 42.)

Errera, M. & Baqué, B. 2013 A quasi-dynamic procedure for coupled thermal simulations. *International Journal for Numerical Methods in Fluids* **72** (11), 1183–1206. (Cited on page 120.)

Esclapez, L., Riber, E. & Cuenot, B. 2015 Ignition probability of a partially premixed burner using {LES}. *Proc. Combust. Inst.* **35** (3), 3133 – 3141. (Cited on page 212.)

Fernandez-Tarrazo, E., Sanchez, A., Linan, A. & Williams, F. A. 2006 A simple one-step chemistry model for partially premixed hydrocarbon combustion. *Combust. Flame* **147** (1-2), 32–38. (Cited on page 98.)

Fieweger, K., Blumenthal, R. & Adomeit, G. 1997 Self-ignition of s.i. engine model fuels: A shock tube investigation at high pressure. *Combustion and Flame* **109** (4), 599–619. (Cited on page 19.)

Fiorina, B., Vicquelin, R., Auzillon, P., Darabiha, N., Gicquel, O. & Veynante, D. 2010 A filtered tabulated chemistry model for les of premixed combustion. *Combustion and Flame* **157** (3), 465–475. (Cited on page 54.)

Fogleman, M., Lumley, J., Rempfer, D. & Haworth, D. 2004 Application of the proper orthogonal decomposition to datasets of internal combustion engine flows. *J. Turb.* **5(023)**. (Cited on page 159.)

Fontanesi, S., D'Adamo, A., Paltrinieri, S. & Cantore, G. 2013 Assessment of the potential of proper orthogonal decomposition for the analysis of combustion ccv and knock tendency in a high performance engine. *SAE paper* (2013-24-0031). (Cited on pages 22 et 23.)

Fontanesi, S., Paltrinieri, S., D'Adamo, A. & Duranti, S. 2014 Investigation of boundary condition and field distribution effects on the cycle-to-cycle variability of a turbocharged gdi engine using les. *Oil Gas Sci. Technol. –Rev. IFP Energies nouvelles* **69** (1), 107–128. (Cited on page 21.)

Franzelli, Benedetta, Riber, Eleonore, Gicquel, Laurent YM & Poinsot, Thierry 2012 Large eddy simulation of combustion instabilities in a lean partially premixed swirled flame. *Combust. Flame* **159** (2), 621–637. (Cited on page 98.)

Franzelli, B., Riber, E., Sanjosé, M. & Poinsot, T. 2010 A two-step chemical scheme for Large-Eddy Simulation of kerosene-air flames. *Combust. Flame* **157** (7), 1364–1373. (Cited on page 97.)

Frayssé, Valérie, Giraud, Luc, Gratton, Serge & Langou, Julien 2005 Algorithm 842: A set of gmres routines for real and complex arithmetics on high performance computers. *ACM Trans. Math. Softw.* **31** (2), 228–238. (Cited on page 119.)

Galmiche, B. 2014 Caractérisation expérimentale des flammes laminaires et turbulentes en expansion. Phd thesis, EMSTU - Orléans. (Cited on page 25.)

García, M., Riber, E., Simonin, O. & Poinsot, T. 2007 Comparison between Euler/Euler and Euler/Lagrange les approaches for confined bluff-body gas-solid flow. (Cited on page 231.)

Ge, H., Juneja, H., Shi, Y., Yang, S. & Reitz, R. 2010 A two-zone multigrid model for si engine combustion simulation using detailed chemistry. *Journal of Combustion* **2010** (201780,). (Cited on pages 21 et 23.)

Germano, M., Piomelli, U., Moin, P. & Cabot, W. 1991 A dynamic subgrid-scale eddy viscosity model. *Phys. Fluids* **3** (7), 1760–1765. (Cited on page 51.)

Ghias, R., Mittal, R. & Dong, H. 2007 A sharp interface immersed boundary method for compressible viscous flows. *J. Comput. Phys.* **225** (1), 528–553. (Cited on page 230.)

Gicquel, L. Y. M., Staffelbach, G. & Poinsot, T. 2012 Large eddy simulations of gaseous flames in gas turbine combustion chambers. *Progress in Energy and Combustion Science* **38** (6), 782–817. (Cited on page 23.)

Giles, M.B. 1997 Stability analysis of numerical interface conditions in fluid-structure thermal analysis. *Int. J. Numer. Meth. Fluids* **25** (4), 421–436. (Cited on page 120.)

Goldstein, D., Handler, R. & Sirovich, L. 1993 Modeling a no-slip flow boundary with an external force field. *Journal of Computational Physics* **105** (2), 354–366. (Cited on pages 231, 232 et 233.)

Goodwin, D. G. 2009 Cantera. (Cited on page 99.)

Goryntsev, D., Klein, M., Sadiki, A. & Janicka, J. 2007 Large eddy simulation of fuel-air mixing in a direct injection SI engine. Munich, Germany. (Cited on page 37.)

Goryntsev, D., Nishad, K., Sadiki, A. & Janicka, J. 2014 Application of les for analysis of unsteady effects on combustion processes and misfires in disi engine. *Oil Gas Sci. Technol. –Rev. IFP Energies nouvelles* **69** (1), 129–140. (Cited on page 21.)

Goryntsev, D., Sadiki, A., Klein, M. & Janicka, J. 2009 Large eddy simulation based analysis of the effects of cycle-to-cycle variations on air-fuel mixing in realistic DISI IC-engines. *Proc. Combust. Inst.* **32**, 2759–2766. (Cited on page 137.)

Granet, V. 2011 La simulation aux grandes echelles : un outil pour la prédiction des variabilités cycliques dans les moteurs à allumage commandé ? Phd thesis, Université de Toulouse - Ecole doctorale MEGeP. (Cited on pages 17, 24, 37, 118, 157, 171, 181 et 209.)

Granet, V., Vermorel, O., Lacour, C., Enaux, B., Dugué, V. & Poinsot, T. 2012 Large-eddy simulation and experimental study of cycle-to-cycle variations of stable and unstable operating points in a spark ignition engine. *Combust. Flame* **159** (4), 1562–1575. (Cited on pages 21, 54, 97, 133, 137 et 230.)

Granet, V., Vermorel, O., Leonard, T., Gicquel, L., & Poinsot, T. 2010 Comparison of nonreflecting outlet boundary conditions for compressible solvers on unstructured grids. *AIAA Journal* **48** (10), 2348–2364. (Cited on page 136.)

Gu, X. J., Emerson, D. R. & Bradley, D. 2003 Modes of reaction front propagation from hot spots. *Combst. Flame* **133** (1–2), 63–74. (Cited on page 105.)

Guibert, P., Keromnes, A. & Legros, G. 2010 An experimental investigation of the turbulence effect on the combustion propagation in a rapid compression machinebulence effect on the combustion propagation in a rapid compression machine. *Flow, Turbulence and Combustion* **84** (1), 79–95. (Cited on page 159.)

Gupta, H.N. 2011 *Fundamentals of Internal Combustion Engines*. PHI Learning Private Limited. (Cited on page 13.)

Halstead, M. P., Kirsch, L. J., Prothero, A. & Quinn, C. P. 1975 A mathematical model for hydrocarbon autoignition at high pressures. *Proceedings of the Royal Society of London. A. Mathematical and Physical Sciences* **346** (1647), 515–538. (Cited on pages 21, 23 et 96.)

Hasse, C., Bollig, M., Peters, N. & Dwyer, H. A. 2000 Quenching of laminar isooctane flames at cold walls. *Combust. Flame* **122** (1-2), 117–129. (Cited on page 97.)

Hasse, C., Sohm, V. & Durst, B. 2010 Numerical investigation of cyclic variations in gasoline engines using a hybrid URANS/LES modeling approach. *Computers & Fluids* **39** (1), 25 – 48. (Cited on page 137.)

Hawkes, E. R. & Cant, S. R. 2000 A flame surface density approach to large eddy simulation of premixed turbulent combustion. pp. 51–58. The Combustion Institute, Pittsburgh. (Cited on page 54.)

Haworth, D. 1999 Large-eddy simulation of in-cylinder flows. *Oil and Gas Science Tech.- Rev de l'IFP* **54** (2), 175–185. (Cited on pages 21 et 37.)

Haworth, D.C. & Jansen, K. 2000 Large-eddy simulation on unstructured deforming meshes: towards reciprocating IC engines. *Comput. Fluids* **29**, 493–524. (Cited on page 235.)

Heywood, J. B. 1988 *Internal combustion engine fundamentals*. New-York: McGraw-Hill. (Cited on pages 12, 13, 153 et 167.)

Hinze, J. O. 1975 *Turbulence*. New-York: McGraw-Hill. (Cited on page 50.)

Hirschfelder, J., Curtis, C. & Bird, B. 1954 *Molecular Theory of Gases and Liquids*, 1954th edn. John Wiley & Sons. (Cited on page 42.)

Hirt, C. W., Amsden, A.A. & Cook, J. L. 1974 An arbitrary lagrangian-eulerian computing method for all flow speeds. *J. Comput. Phys.* **131** (4), 371–385. (Cited on page 62.)

Iaccarino, G. & Verzicco, R. 2003 Immersed boundary technique for turbulent flow simulations. *App. Mech. Rev.* **56** (3), 331–347. (Cited on page 231.)

Jerzembeck, S., Peters, N., Pepiot-Desjardins, P. & Pitsch, H. 2009 Laminar burning velocities at high pressure for primary reference fuels and gasoline: Experimental and numerical investigation. *Combust. Flame* **156** (2), 292–301. (Cited on pages 53, 99, 100, 101, 102 et 147.)

Kalghatgi, G.T. & Bradley, D. 2012 Pre-ignition and 'super-knock' in turbo-charged spark-ignition engines. *International Journal of Engine Research* **13** (4), 399–414. (Cited on page 19.)

Kalghatgi, G. T. 1995 Combustion chamber deposits in spark ignition engines – a literature review. *SAE -Transactions–J Fuels and Lubricants* **105** (952443). (Cited on page 19.)

Kanti, M., Kawahara, N. & Tomita, E. 2010 Visualization of knocking combustion in a hydrogen spark-ignition engine. *Proc. WHEC* **78** (6). (Cited on page 17.)

Kawahara, N., Tomita, E. & Sakata, Y. 2007 Auto-ignited kernels during knocking combustion in a spark-ignition engine. *Proceedings of the Combustion Institute* **31** (2), 2999–3006. (Cited on page 15.)

Keck, J. C. 1982 Turbulent flame structure and speed in spark-ignition engines. pp. 1451–1466. The Combustion Institute, Pittsburgh. (Cited on page 57.)

Kolmogorov, A. N. 1941 The local structure of turbulence in incompressible viscous fluid for very large reynolds numbers. *C. R. Acad. Sci. , USSR* **30**, 301. (Cited on page 45.)

Kulkarni, R. & Polifke, W. 2012 Large eddy simulation of autoignition in a turbulent hydrogen jet flame using a progress variable approach. *Journal of Combustion* . (Cited on page 96.)

Kuo, K. K. 2005 Second Edition *Principles of combustion*. Hoboken, New Jersey: John Wiley & Sons, Inc. (Cited on pages 43 et 54.)

Lacaze, G., Richardson, E. & Poinsot, T. J. 2009 Large eddy simulation of spark ignition in a turbulent methane jet. *Combust. Flame* **156** (6), 1993–2009. (Cited on page 59.)

Lafossas, F., Castagne, M., Dumas, J. & Henriot, S. 2002 Development and validation of a knock model in spark ignition engines using a CFD code . (Cited on pages 21 et 23.)

Lamarque, N. 2007 Schémas numériques et conditions limites pour la simulation aux grandes échelles de la combustion diphasique dans les foyers d'hélicoptère. Phd thesis, INP Toulouse. (Cited on pages 52 et 91.)

Lax, P. D. & Wendroff, B. 1960 Systems of conservation laws. *Commun. Pure Appl. Math.* **13**, 217–237. (Cited on pages 52 et 137.)

Lecocq, G., Richard, S., Michel, J. & Vervisch, L. 2011 A new LES model coupling flame surface density and tabulated kinetics approaches to investigate knock and pre-ignition in piston engines. *Proc. Combust. Inst.* **33** (6), 1215–1226. (Cited on pages 22, 23 et 28.)

Lefebvre, A. H. 1999 *Gas Turbines Combustion*. Taylor & Francis. (Cited on page 24.)

Légier, J.-Ph., Poinsot, T. & Veynante, D. 2000 Dynamically thickened flame LES model for premixed and non-premixed turbulent combustion. pp. 157–168. Center for Turbulence Research, NASA Ames/Stanford Univ. (Cited on pages 54 et 56.)

Légier, J.-Ph., Varoquié, B., Lacas, F., Poinsot, T. & Veynante, D. 2002 Large eddy simulation of a non-premixed turbulent burner using a dynamically thickened flame model. In *IUTAM Symposium on Turbulent Mixing and Combustion* (ed. A. Pollard Eds & S. Candel), pp. 315 – 326. Kluwer Academic Publishers. (Cited on page 56.)

Li, Yuanhong & Kong, Song-Charng 2011 Coupling conjugate heat transfer with in-cylinder combustion modeling for engine simulation. *International Journal of Heat and Mass Transfer* **54** (11–12), 2467–2478. (Cited on pages 24 et 118.)

Li, Y., Yun, A. & Kim, J. 2012 An immersed boundary method for simulating a single axisymmetric cell growth and division. *J. Math. Biol.* **65** (4). (Cited on page 229.)

Lieuwen, T., McDonell, V., Petersen, E. & Santavicca, D. 2008 Fuel flexibility influences on premixed combustor blowout, flashback, autoignition, and stability. *Journal of Engineering for Gas Turbines and Power* **130** (1), 011506–011506. (Cited on page 212.)

Lightfoot, N. S. & Negus, C. R. 1985 Investigation of the 'knock' phenomenon in an optically-accessed engine. *Symposium (International) on Combustion* **20** (1), 111–122. (Cited on pages 15 et 18.)

Lilly, D. K. 1992 A proposed modification of the Germano sub-grid closure method. *Phys. Fluids* **4** (3), 633–635. (Cited on page 51.)

Linse, D., Kleemann, A. & Hasse, C. 2014 Probability density function approach coupled with detailed chemical kinetics for the prediction of knock in turbocharged direct injection spark ignition engines. *Combustion and Flame* **161** (4), 997–1014. (Cited on pages 21, 23, 24 et 118.)

Litzinger, T. A. 1990 A review of experimental studies of knock chemistry in engines. *Progress in Energy and Combustion Science* **16** (3), 155–167. (Cited on page 15.)

Livengood, J. C. & Wu, P. C. 1955 Correlation of autoignition phenomena in internal combustion engines and rapid compression machines. *Proc. Combust. Inst.* **5** (1), 347–356. (Cited on page 21.)

Magnussen, B. F. & Hjertager, B. H. 1977 On mathematical modeling of turbulent combustion with special emphasis on soot formation and combustion. *Proc. Combust. Inst.* **16** (1), 719–729. (Cited on pages 21 et 23.)

Maly, R. & Vogel, M. 1979 Initiation and propagation of flame fronts in lean CH4-air mixtures by the three modes of the ignition spark. *Symposium (International) on Combustion* **17** (1), 821–831. (Cited on pages 58 et 60.)

Marc, D., Boree, J. & Charnay, R. Bazile G. 2013 Tumbling vortex flow in a model square piston compression machine: PIV and LDV measurements. *SAE paper* (2013-24-0031). (Cited on page 159.)

Misdariis, A., Robert, A., Vermorel, O., Richard, S. & Poinsot, T. 2014 Numerical methods and turbulence modeling for LES of piston engines: Impact on flow motion and combustion. *Oil Gas Sci. Technol. – Rev. IFP Energies nouvelles* **69** (1), 83–105. (Cited on page 147.)

Morse, A. P., Whitelaw, J. H. & Yianneskis, M. 1979 Turbulent flow measurements by laser-doppler anemometry in motored piston-cylinder assemblies. *Journal of Fluids Engineering* **101** (2), 208–216. (Cited on pages 8, 235, 239, 241, 242, 243, 244, 245, 246 et 247.)

Moureau, V. 2004 Simulation aux grandes échelles de l'aérodynamique interne des moteurs à piston. Phd thesis, INP Toulouse. (Cited on pages 37, 62 et 209.)

Moureau, V., Fiorina, B. & Pitsch, H. 2009 A level set formulation for premixed combustion LES considering the turbulent flame structure. *Combust. Flame* **156** (4), 801–812. (Cited on page 54.)

Moureau, V., Lartigue, G., Sommerer, Y., Angelberger, C., Colin, O. & Poinsot, T. 2005 Numerical methods for unsteady compressible multi-component reacting flows on fixed and moving grids. *J. Comput. Phys.* **202** (2), 710 – 736. (Cited on page 62.)

Moureau, V. R., Vasilyev, O. V., Angelberger, C. & Poinsot, T. J. 2004 Commutation errors in Large Eddy Simulations on moving grids: Application to piston engine flows. pp. 157–168. Center for Turbulence Research, NASA AMES/Stanford University, USA. (Cited on page 63.)

Naitoh, K., Kaneko, Y. & Iwata, K. 2004 Cycle-resolved large eddy simulation of actual 4-valve engine based on quasi-gridless approach. *SAE* (2004-01-3006). (Cited on pages 230 et 247.)

Naitoh, K., Ono, M., Kuwahara, K. & Krause, E. 2002 Cycle-resolved computations of compressible flow in engine. *SAE* (2002-01-2694). (Cited on pages 230 et 247.)

Oefelein, J.C. 2006 Mixing and combustion of cryogenic oxygen-hydrogen shear-coaxial jet flames at supercritical pressure. *Combustion science and technology* **178** (1-3), 229–252. (Cited on page 259.)

Oefelein, Joseph C 2005 Thermophysical characteristics of shear-coaxial lox–h¡ sub¿ 2¡/sub¿ flames at supercritical pressure. *Proceedings of the Combustion Institute* **30** (2), 2929–2937. (Cited on page 259.)

Oppenheim, A. & Soloukhin, R. 1973 Experiments in gasdynamics of explosions. *Annual Review of Fluid Mechanics* pp. 31–58. (Cited on page 105.)

Ozdor, N., Dulger, M. & Sher, E. 1994 Cyclic variability in spark ignition engines. A literature survey. *SAE* (950683). (Cited on page 11.)

Passot, T. & Pouquet, A. 1987 Numerical simulation of compressible homogeneous flows in the turbulent regime. *J. Fluid Mech.* **181**, 441–466. (Cited on page 90.)

Patnaik, G., Kailasanath, K., Laskey, K. & Oran, E. 1988 Detailed numerical simulations of cellular flames. pp. 1517–1526. The Combustion Institute, Pittsburgh. (Cited on page 53.)

Pera, C. & Angelberger, C. 2011 Large eddy simulation of a motored single-cylinder engine using system simulation to define boundary conditions: Methodology and validation. *SAE paper* (2011-01-0834). (Cited on page 209.)

Peskin, C. S. 1972 Flow patterns around heart valves: A numerical method. *J. Comput. Phys.* **10**, 252–271. (Cited on page 229.)

Peters, N. 1999 The turbulent burning velocity for large-scale and small-scale turbulence. *J. Fluid Mech.* **384**, 107 – 132. (Cited on page 23.)

Peters, N., Kerschgens, B. & Paczko, G. 2012 Super-knock prediction using a refined theory of turbulence. *SAE paper* (2013-01-1109). (Cited on pages 20, 21 et 24.)

Pickett, Lyle M, Genzale, Caroline L, Bruneaux, Gilles, Malbec, Louis-Marie, Hermant, Laurent, Christiansen, Caspar Ask & Schramm, Jesper 2010 Comparison of diesel spray combustion in different high-temperature, high-pressure facilities. *SAE International Journal of Engines* **3** (2), 156–181. (Cited on page 259.)

Pitsch, H 2005 A consistent level set formulation for large-eddy simulation of premixed turbulent combustion. *Combustion and Flame* **143** (4), 587–598. (Cited on page 54.)

Poinsot, T. & Lele, S. 1992 Boundary conditions for direct simulations of compressible viscous flows. *J. Comput. Phys.* **101** (1), 104–129. (Cited on pages 136, 147 et 239.)

Poinsot, T. & Veynante, D. 2011 *Theoretical and Numerical Combustion*. (Cited on pages 46, 102 et 175.)

Pope, S. B. 2000 *Turbulent flows*. Cambridge University Press. (Cited on page 90.)

Pöschl, M. & Sattelmayer, T. 2008 Influence of temperature inhomogeneities on knocking combustion. *Combustion and Flame* **153** (4), 562–573. (Cited on page 20.)

Quillatre, P., Vermorel, O., Poinsot, T. & Ricoux, P. 2013 Large eddy simulation of vented deflagration. *Ind. Eng. Chem. Res.* **52** (33), 11414–11423. (Cited on page 97.)

Rejniak, Katarzyna A. 2007 An immersed boundary framework for modelling the growth of individual cells: An application to the early tumour development. *Journal of Theoretical Biology* **247** (1), 186–204. (Cited on page 229.)

Renouard, V. & Pera, C. 2011 Caractérisation d'une base de données expérimentales dédiées à la simulation aux grandes echelles des instabilités en moteur downsizé à allumage commandé. *Tech. Rep.*. IFPEN. (Cited on page 136.)

Réveillé, B. & Duparchy, A. 2009 Analyse par MFN 3d d'un phenomene de combustion anormalement rapide sur moteurs essence eco-suralimentes. *Oil and Gas Science Tech. - Rev. IFP* **64** (3), 431–444. (Cited on pages 21 et 23.)

Richard, S. 2005 Simulation aux grandes échelles de la combustion dans les moteurs à allumage commandé. Phd thesis, Ecole Centrale Paris. (Cited on pages 37, 57, 58 et 209.)

Richard, S., Vermorel, O. & Veynante, D. 2005 Development of LES models based on the flame surface density approach for ignition and combustion in SI engines. pp. 1–20. (Cited on page 54.)

Robert, A. 2014 Simulation aux grandes echelles des combustions anormales dans les moteurs downsizés à allumage commandé. Phd thesis, INP Toulouse. (Cited on pages 22, 23, 25, 27, 30, 57, 96, 131, 137, 138, 146, 151, 153, 154, 155, 159, 179, 180 et 181.)

Rutland, C J 2011 Large-eddy simulations for internal combustion engines –a review. *International Journal of Engine Research* . (Cited on page 21.)

Rutland, C. J. & Cant, R. S. 1994 Turbulent transport in premixed flames. In *Proc. of the Summer Program* , pp. 75–94. Center for Turbulence Research, NASA Ames/Stanford Univ. (Cited on page 53.)

Rutland, C. J. & Ferziger, J. 1991 Simulation of flame-vortex interactions. *Combust. Flame* **84**, 343–360. (Cited on page 53.)

Sagaut, P. 2002 *Large eddy simulation for incompressible flows*. Springer. (Cited on pages 51 et 165.)

Saiki, E. M. & Biringen, S. 1996 Numerical simulation of a cylinder in uniform flow: Application of a virtual boundary method. *Journal of Computational Physics* **123** (2), 450–465. (Cited on pages 231 et 237.)

Sánchez, A.L., Lépinette, A., Bollig, M., Linán, A. & Lázaro, B. 2000 The reduced kinetic description of lean premixed combustion. *Combust. Flame* **123**, 436–464. (Cited on page 98.)

Sazhina, E. M., Sazhin, S. S., Heikal, M. R. & Marooney, C. J. 1999 The shell autoignition model: applications to gasoline and diesel fuels. *Fuel* **78** (4), 389–401. (Cited on page 96.)

Schmitt, P., Poinsot, T., Schuermans, B. & Geigle, K. P. 2007 Large-eddy simulation and experimental study of heat transfer, nitric oxide emissions and combustion instability in a swirled turbulent high-pressure burner. *J. Fluid Mech.* **570**, 17–46. (Cited on pages 97 et 136.)

Selle, L., Lartigue, G., Poinsot, T., Koch, R., Schildmacher, K.-U., Krebs, W., Prade, B., Kaufmann, P. & Veynante, D. 2004 Compressible large-eddy simulation of turbulent combustion in complex geometry on unstructured meshes. *Combust. Flame* **137** (4), 489–505. (Cited on page 56.)

Shiga, S., Ehara, H., Karasawa, T. & Kurabayashi, T. 1988 Effect of exhaust gas recirculation on diesel knock intensity and its mechanism. *Combustion and Flame* **72** (3), 225–234. (Cited on page 17.)

Shu, C., Liu, N. & Chew, Y. T. 2007 A novel immersed boundary velocity correction–lattice boltzmann method and its application to simulate flow past a circular cylinder. *Journal of Computational Physics* **226** (2), 1607–1622. (Cited on page 237.)

Smagorinsky, J. 1963 General circulation experiments with the primitive equations: 1. the basic experiment. *Mon. Weather Rev.* **91**, 99–164. (Cited on pages 50, 51 et 137.)

Smolarkiewicz, P. K., Sharman, R., Weil, J., Perry, S. G., Heist, D. & Bowker, G. 2007 Building resolving large-eddy simulations and comparison with wind tunnel experiments. *J. Comput. Phys.* **227** (1), 633–653. (Cited on page 230.)

Sokolik, A. & Voinov, A. 1940 Knocking in an internal-combustion engine. *NASA Technical Reports* (NACA-TM-928). (Cited on page 18.)

Tanahashi, M., Nada, Y., Fujimura, M. & Miyauchi, T. 1999 Fine scale structure of H2-air turbulent premixed flames. pp. 59–64. Santa Barbara, Sept 12-15. (Cited on page 53.)

Tennekes, H. & Lumley, J. L. 1972 *A first course in turbulence*. Cambridge: M.I.T. Press. (Cited on page 50.)

Teraji, A., Tsuda, T., Noda, T., Kubo, M. & Itoh, T. 2005 Development of a novel flame propagation model (UCFM: Universal coherent flamelet model) for SI engines and its application to knocking prediction . (Cited on pages 21 et 23.)

Thobois, L. 2006 Intérêt et faisabilité de la simulation aux grandes échelles dans les moteurs automobiles. Phd thesis, INP Toulouse. (Cited on pages 37 et 209.)

Thobois, L., Lauvergne, R. & Poinsot, T. 2007 Using LES to investigate reacting flow physics in engine design process. *SAE* (2007-01-0166). (Cited on page 54.)

Toninel, S., Forkel, H., Frank, T., Durst, B., Hasse, C. & Linse, D. 2009 Implementation and validation of the g-equation model coupled with flamelet libraries for simulating premixed combustion in i.c. engines. *SAE paper* (2009-01-0709). (Cited on page 23.)

Trouvé, A. & Poinsot, T. 1994 The evolution equation for the flame surface density. *J. Fluid Mech.* **278**, 1–31. (Cited on page 53.)

Tseng, Yu-Heng & Ferziger, Joel H. 2003 A ghost-cell immersed boundary method for flow in complex geometry. *Journal of Computational Physics* **192** (2), 593–623. (Cited on page 237.)

Uhlmann, Markus 2005 An immersed boundary method with direct forcing for the simulation of particulate flows. *J. Comput. Phys.* **209** (2), 448–476. (Cited on page 230.)

Vermorel, O., Richard, S., Colin, O., Angelberger, C., Benkenida, A. & Veynante, D. 2007 Multi-cycle LES simulations of flow and combustion in a PFI SI 4-valve production engine. *SAE* (2007-01-0151). (Cited on pages 37 et 209.)

Vermorel, O., Richard, S., Colin, O., Angelberger, C., Benkenida, A. & Veynante, D. 2009 Towards the understanding of cyclic variability in a spark ignited engine using multi-cycle LES. *Combust. Flame* **156** (8), 1525–1541. (Cited on page 54.)

Verzicco, R., Mohd-Yusof, J., Orlandi, P. & Haworth, D. 2000 Large eddy simulation in complex geometric configurations using boundary body forces. *AIAA Journal* **38** (3), 427–433. (Cited on pages 62, 230 et 247.)

Wei, H., Zhu, T., Shu, G., Tan, L. & Wang, Y. 2012 Gasoline engine exhaust gas recirculation –a review. *Applied Energy* **99** (0), 534–544. (Cited on page 17.)

Westbrook, C. K., Pitz, W. J., Herbinet, O., Curran, H. J. & Silke, E. J. 2009 A comprehensive detailed chemical kinetic reaction mechanism for combustion of n-alkane hydrocarbons from n-octane to n-hexadecane. *Combust. Flame* **156** (1), 181–199. (Cited on pages 96 et 97.)

Williams, F. A. 1985 *Combustion Theory*. Menlo Park, CA: Benjamin Cummings. (Cited on pages 21, 23 et 54.)

Wolf, P., Staffelbach, G., Balakrishnan, R., Roux, A. & Poinsot, T. 2010 Azimuthal instabilities in annular combustion chambers. pp. 259–269. (Cited on page 56.)

Wolf, P., Staffelbach, G., Roux, A., Gicquel, L., Poinsot, T. & Moureau, V. 2009 Massively parallel LES of azimuthal thermo-acoustic instabilities in annular gas turbines. *Comptes Rendus Mécanique* **337** (6-7), 385–394. (Cited on pages 97 et 212.)

Yeung, P. K., Girimaji, S. S. & Pope, S. B. 1990 Straining and scalar dissipation on material surfaces in turbulence: implications for flamelets. *Combust. Flame* **79**, 340–365. (Cited on page 55.)

Young, M. B. 1981 Cyclic dispersion in the homogeneous charge spark-ignition engine. a literature survey. *SAE* (810020). (Cited on page 167.)

Zeldovich, Ya. B. 1980 Regime classification of an exothermic reaction with nonuniform initial conditions. *Combustion and Flame* **39** (2), 211–214. (Cited on pages 20, 21, 24, 105 et 249.)

Partie IV

Annexes

APPENDIX A

Méthodologie de frontières immergées

A.1 Introduction

La méthode des frontières immergées (IBM pour *Immersed Boundary Method*) est une approche communément utilisée pour la simulation des frontières mobiles telles qu'il en existe dans les moteurs à piston. Dans *AVBP*, le choix s'est porté sur l'utilisation de maillages conformants (BC pour *Body Conformal*) avec une méthodologie de type ALE. Cependant, dans certains cas, l'approche de frontières immergées peut s'avérer être une alternative intéressante. Cette approche permet de dissocier les frontières du maillage des frontières géométriques du domaine de calcul ainsi qu'illustré Fig. A.1.

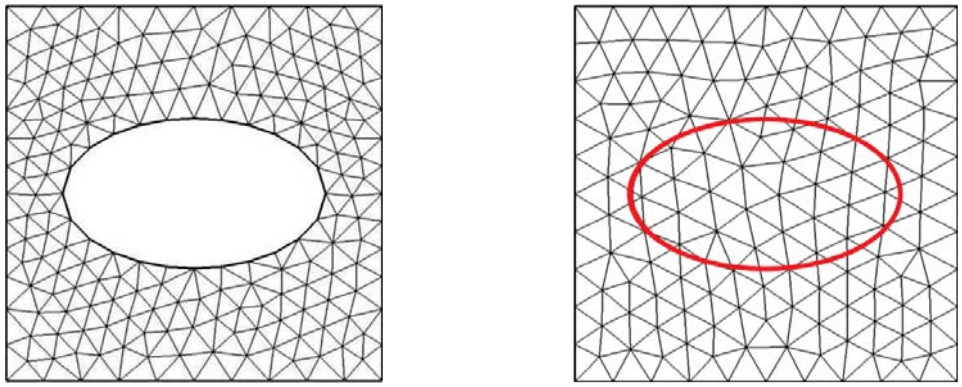

(a) Maillage conformant.

(b) Frontière immergée.

Figure A.1: Comparaison des méthodes avec maillage conformant (BC) et frontières immergées (IBM)

Historiquement Peskin (1972) est le premier à introduire cette méthode en 1972 pour étudier les mécanismes cardiaques et les écoulements sanguins associés. Depuis, la méthode IBM a largement été reprise notamment dans le domaine biologique et médical afin de simuler le développement initial des tumeurs (Rejniak, 2007) ou la croissance et division de cellules animales (Li *et al.*, 2012) par exemple. Cette méthode a également été largement reprise dans d'autres domaines tels que l'étude des écoulements supersoniques autour de géométries

complexes sur maillage cartésien (Ghias *et al.*, 2007), les écoulements autour de particules solides (Uhlmann, 2005) ou encore les écoulements autour de bâtiments (Smolarkiewicz *et al.*, 2007). Dans la communauté moteurs à piston, l'approche IBM est également largement utilisée comme alternative aux méthodes de mouvement de maillage pour la modélisation des pièces mobiles telles que les soupapes ou le piston (Verzicco *et al.*, 2000; Naitoh *et al.*, 2002, 2004).

Lors de précédentes études proposées par Granet *et al.* (2012) ou Enaux *et al.* (2011*a*), l'approche ALE associée à des maillages non structurés a démontré une bonne capacité à reproduire l'aérodynamique interne des moteurs à combustion interne. Chacune de ces deux approches, i.e. frontières immergées et maillage conformant avec déformation de maillage, présente ses propres avantages et défauts. Un des principaux avantages de la méthode IBM est sa plus grande simplicité de mise en données: alors que de nombreux maillages sont à réaliser pour décrire un cycle moteur entier avec phases d'ouvertures et de fermetures des soupapes, un seul maillage peut être suffisant avec l'approche IBM même si une étape supplémentaire est nécessaire pour initialiser un traceur de frontières. De plus, pendant la simulation il suffit simplement d'utiliser une loi de déplacement du traceur de frontière alors que des modifications plus importantes sont nécessaires avec la stratégie de déformation de maillage. Avec une méthode de type ALE, les schémas numériques doivent être modifiés pour prendre en compte la vitesse de grille dans l'expression des flux aux frontières des cellules. La déformation du maillage peut également poser des problèmes de stabilité du calcul si celle-ci est trop importante. En revanche, il est difficile d'assurer des flux nuls à travers les frontières immergées (thermiques, convectifs et diffusifs) dans certains cas, notamment lorsque l'écoulement est fortement turbulent. Ce point pose particulièrement problème dans les simulations de moteurs à piston où la masse enfermée dans le piston et les transferts thermiques à la paroi jouent un rôle important sur la phase de combustion et sur les niveaux de pression atteints dans le cylindre.

Pour les simulations présentées dans ce manuscrit, il a donc été choisi de conserver un maillage conformant pour la modélisation des parois mobiles. Dans le cas du moteur ECOSURAL, le cycle moteur est décrit par 40 phases de calcul. Pour chacune d'elles, un maillage est généré puis déformé pour obtenir un maillage initial et un maillage final. Cette étape de mise en données est fastidieuse et nécessite un temps humain important. Dans le cadre du projet ICAMDAC, la variation géométrique des conduits d'admission est réalisée expérimentalement par l'ajout d'une pièce appelée *masque de tumble* illustrée Fig. A.2. Dans ce chapitre, l'intérêt de la méthode

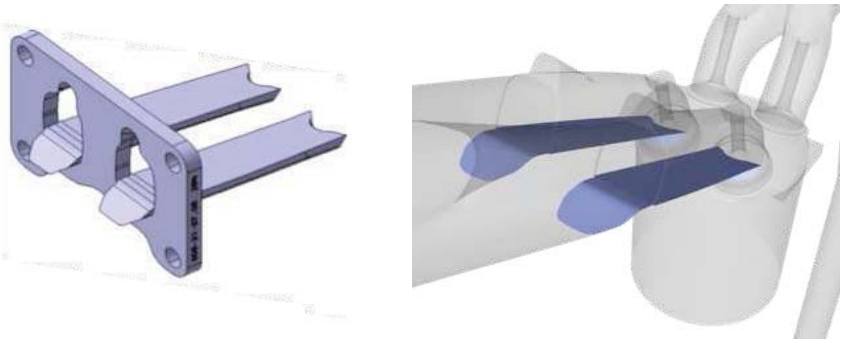

Figure A.2: Masque de tumble installé dans les conduits d'admission pour modifier l'écoulement pour le point de fonctionnement *aéro+*.

IBM pour prendre en compte de telles variations de la géométrie est évaluée afin d'éviter de répéter l'étape de génération de maillages pour le point de fonctionnement *aéro+*.

A.2 Implémentation de la méthode de frontières immergées

Pour modéliser la présence d'une frontière solide immergée dans le domaine, des termes sources (ou termes de forçage) sont ajoutés aux équations de transport. Il est possible de distinguer deux types de méthodes IBM par la façon dont sont formulés ces termes sources:

- **Le forçage direct**: avec cette méthode, la vitesse est imposée directement sur la frontière immergée. Le terme de forçage est calculé de façon à directement annuler la différence entre la vitesse calculée et celle désirée sur la frontière immergée.
- **Le forçage continu**: un terme source est ajouté au membre de droite des équations de transport à résoudre (Euler ou Navier-Stokes) pour forcer la vitesse située sur la frontière à être égale à la vitesse de déplacement de la frontière.

Un état de l'art de la méthode IBM pour des frontières solides est proposé par Iaccarino & Verzicco (2003). L'implantation de la méthode IBM dans le code de calcul *AVBP* débutée par Bonhomme (2014) a été reprise et poursuivie dans le cadre de ce travail. La formulation du forçage continu proposée par Goldstein *et al.* (1993) et reprise par Saiki & Biringen (1996) repose sur une description Lagrangienne des termes de forçage: le mur est discrétisé par un champ de particules qui interagit avec le champ Eulerien pour imposer une condition de mur à la position souhaitée. Cette formulation qui nécessite peu de développements en plus du module diphasique Lagrangien est retenue dans *AVBP*.

A.3 Le module Lagrangien d'*AVBP*

Le module Lagrangien a été introduit dans *AVBP* par García *et al.* (2007) pour traiter des écoulements diphasiques par une approche Euler-Lagrange. Ce module comporte:

- une structure de données dédiée,
- un algorithme de localisation des particules,
- un algorithme pour connaitre les propriétés du gaz à la position de la particule, obtenues à partir d'une interpolation de ces variables aux noeuds de la cellule contenant la particule,
- un couplage à double sens entre les champs Eulerien et Lagrangien: la vitesse de déplacement de la particule est impactée par l'écoulement porteur mais la phase gazeuse est également impactée par les forces de trainée introduites par la particule.

Dans les simulations diphasiques Lagrangiennes, les équations de Navier-Stokes présentées Chap. 2 sont modifiées pour prendre en compte les échanges de masse, de quantité de mouvement et d'énergie entre les particules et la phase gazeuse. Pour cela des termes supplémentaires sont ajoutés aux membres de droite des équations de Navier-Stokes:

$$\frac{\partial \overline{\rho}}{\partial t} + \frac{\partial}{\partial x_i}(\overline{\rho}\tilde{u}_i) = \dot{\rho}_p \tag{A.1}$$

$$\frac{\partial \overline{\rho}\tilde{u}_j}{\partial t} + \frac{\partial}{\partial x_j}(\overline{\rho}\tilde{u}_i\tilde{u}_j) = -\frac{\partial}{\partial x_j}(\overline{P}\delta_{ij} - \overline{\tau}_{ij} - \overline{\tau}^t_{ij}) + \dot{F}_{p,i} \tag{A.2}$$

$$\frac{\partial \overline{\rho}\tilde{E}}{\partial t} + \frac{\partial}{\partial x_j}(\overline{\rho}E\tilde{u}_j) = -\frac{\partial}{\partial x_j}[\overline{u_i(P\delta_{ij} - \tau_{ij})} + \overline{q}_j + \overline{q}^t_j] + \overline{\dot{\omega}}_T + \overline{Q}_r + \dot{Q}_p \tag{A.3}$$

$$\frac{\partial \overline{\rho}\tilde{Y}_k}{\partial t} + \frac{\partial}{\partial x_j}(\overline{\rho}\tilde{Y}_k\tilde{u}_j) = -\frac{\partial}{\partial x_j}[\overline{J}_{j,k} + \overline{J}^t_{j,k}] + \overline{\dot{\omega}}_k + \dot{S}_{p,k} \tag{A.4}$$

où $\dot{\rho}_p$, $\dot{F}_{p,i}$, $\dot{Q}_p$ et $\dot{S}_{p,k}$ représentent respectivement les termes source de masse, de quantité de mouvement, d'énergie et de fraction massique.

A.4 Adaptation du module Lagrangien pour la méthode IBM

Basée sur un formalisme Lagrangien, la formulation IBM en forçage continu proposé par Goldstein *et al.* (1993) et reprise dans *AVBP* est très proche de la formulation du module Lagrangien. Dans cette formulation IBM, le mur est modélisé par des particules dans le maillage Eulerien ainsi qu'illustré Fig. A.3. Pour modéliser le mur, chacune des cellules du maillage dans lesquelles

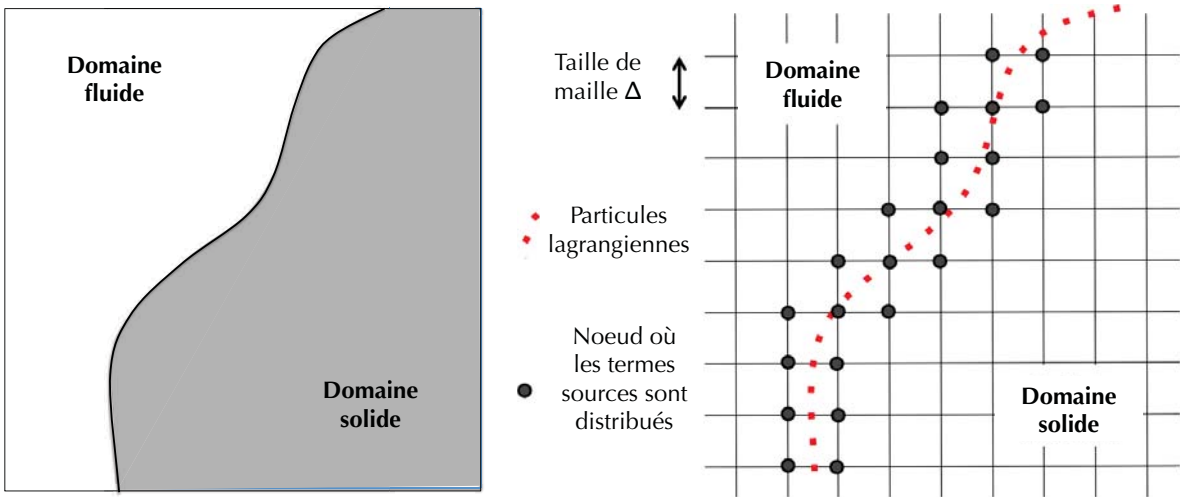

Figure A.3: Configuration à modéliser à gauche et modélisation d'un mur par particules Lagrangiennes à droite.

le mur passe doit contenir au minimum une particule. Deux options sont possibles: soit les particules sont uniquement disposées à la surface du mur à modéliser, soit le domaine solide est entièrement rempli de particules. Dans ce travail, il a été choisi de ne discrétiser que la surface du mur par des particules afin de limiter le surcoût de calcul lié au suivi d'un grand nombre de particules Lagrangiennes. Afin de reproduire le comportement du mur il suffit alors de forcer la vitesse du fluide à la position de chaque particule à être égale à la vitesse de cette particule. On obtient ainsi une condition de mur non glissant.

Les équations du module Lagrangien Eq. A.1 à A.4 peuvent être reprises en imposant les variations de masse $\dot{\rho}_p$ et d'espèces $\dot{S}_{p,k}$ à zéro. En fonction des cas à simuler, l'utilisateur peut soit imposer une loi pour la vitesse des particules si le mur est mobile, soit imposer une vitesse nulle. L'adaptation majeure à apporter au module Lagrangien porte sur le terme d'interaction fluide-particule $\dot{F}_{p,i}$. Dans l'approche IBM, ce terme source ne représente plus une force de trainée comme c'est le cas pour les écoulements diphasiques mais la force à appliquer au fluide pour obtenir la condition de non glissement au mur. Le terme source dans l'équation de l'énergie $\dot{Q}_p$ représentant la puissance de la force appliquée par la particule sur le fluide s'exprime, comme dans le cas d'une particule diphasique comme le produit de la force appliquée par la particule sur le fluide et de la vitesse de cette particule.

A.4.1 Terme source de quantité de mouvement

Différentes formulations sont disponibles pour l'expression de la force d'interaction fluide-particule $\dot{F}_{p,i}$. Il a été choisi d'implémenter le terme de forçage de Goldstein *et al.* (1993) dans le code *AVBP*. Pour chaque noeud m des cellules contenant au minimum une particule,

l'expression du terme source dans l'équation de quantité de mouvement du champ Eulerien (Eq. A.2) s'écrit:

$$\dot{F}^m_{p,i} = \frac{1}{\sum_{n=1}^{Np} W(x^n_i, x^m_i)} \sum_{n=1}^{Np} f^n_i . W(x^n_i, x^m_i) \tag{A.5}$$

où N_p est le nombre de particules associé au volume de contrôle, f^n_i est la force de la particule n située en x^i_n et W est le poids de la particule n pour la projection de la force Lagrangienne sur le noeud m. Le poids des particules dans l'opération de projection est déterminé de façon géométrique comme l'inverse de la distance d_j entre la particule et le noeud m:

$$W_j = \frac{1/d_j}{\sum_{k=1}^{N} 1/d_k} W_p \tag{A.6}$$

avec j l'indice du noeud dans la cellule et N le nombre de noeuds par cellule du maillage. La figure A.4 représente la façon dont sont projetées les contributions Lagrangiennes sur le maillage Eulerien. Le terme source dans l'équation de l'énergie s'écrit:

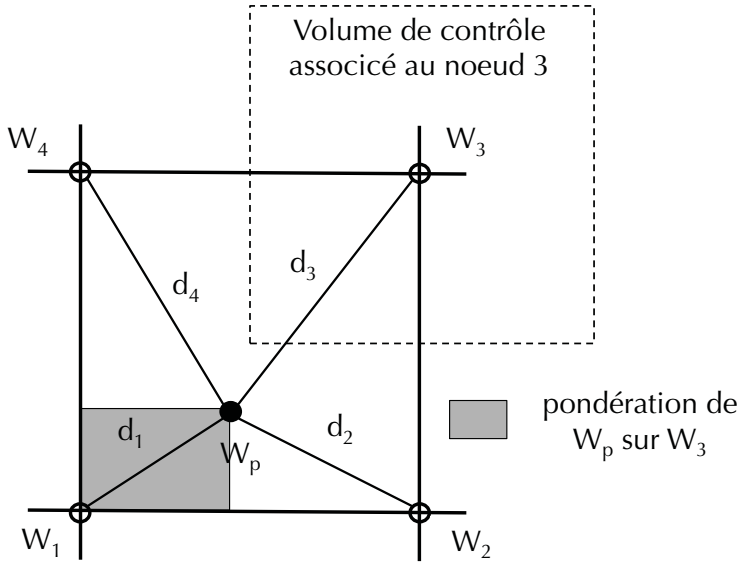

Figure A.4: Exemple de projection des contributions Lagrangiennes sur les noeuds du maillage Eulerien basée sur une méthode de volume inverse.

$$\dot{Q}_p = \sum_i \dot{F}_{p,i} u_{p,i} \tag{A.7}$$

où $\dot{F}_{p,i}$ est la projection des termes de forçage f^n_i sur le maillage. La formulation de Goldstein *et al.* (1993) permet d'écrire le terme de forçage à la position de la particule en fonction de la vitesse du fluide à la position de la particule $u_{f@p,i}$:

$$f^n_i = \beta^{IBM} \int_0^t (u^n_{p,i} - u_{f@p,i})\ \mathrm{d}t' + \alpha^{IBM}(u^n_{p,i} - u_{f@p,i}) \tag{A.8}$$

Cette expression permet d'imposer la vitesse du fluide égale à la vitesse de la particule à la position de la particule, ce qui revient à imposer une condition de non glissement à la paroi.

Dans certains cas, il peut être intéressant d'imposer une condition de glissement. Dans ce cas, il suffit de projeter les vitesses du fluide et de la particule dans la direction normale à la particule et d'annuler la composante normale uniquement. Dans la pratique, la normale du mur à modéliser en IBM $\vec{n}_p$ est calculée et sauvegardée pour chaque particule. L'expression A.8 devient:

$$f_i^n = \beta^{IBM} \int_0^t ((u_{p,i}^n - u_{f@p,i}).\vec{n}_p)\ \mathrm{d}t' + \alpha^{IBM}((u_{p,i}^n - u_{f@p,i}).\vec{n}_p) \tag{A.9}$$

α^{IBM} et β^{IBM} sont les coefficients des correcteurs proportionnels et intégraux décrits ci-dessous. Ces expressions du terme de forçage sont équivalentes à un forçage direct du champs de vitesse Eulerien à la vitesse de la particule $\mathbf{u_p}$. Une analogie peut être réalisée avec les contrôleurs de type Proportionnel-Intégral (PI) en automatisme de systèmes. Chacun des deux termes des équations A.8 ou A.9 représente un correcteur faisant tendre la vitesse du fluide à la position de la particule $u_{f@p,i}$ vers une consigne représentée par la vitesse de la particule.

1. **Le correcteur proportionnel (P):**
   Le terme proportionnel s'exprime directement en fonction de la différence de vitesse entre la particule et le fluide:

   $$f_i^n = \alpha^{IBM}(u_{p,i}^n - u_{f@p,i}) \tag{A.10}$$

   Le terme α^{IBM} contrôle la raideur du correcteur: si $\alpha^{IBM} \to 0$ la correction est nulle et l'écoulement ne verra pas d'obstacle. A l'inverse, le cas $\alpha^{IBM} \to 1$ impose la condition $\mathbf{u_{f@p}} = \mathbf{u_p}$, ce qui revient à une condition de non glissement à la paroi de l'obstacle IBM. Si aucune porosité n'est souhaitée à travers le mur à modéliser, il faut choisir α^{IBM} proche de 1, ce qui est fait dans le cas d'écoulements laminaires. Dans des cas à nombre de Reynolds élevé, la vitesse $u_{f@p}$ peut fluctuer de façon importante. Dans ce cas le coefficient α^{IBM} doit être diminué pour éviter les fluctuations du terme de forçage qui mèneraient à l'instabilité du calcul.
2. **Le correcteur Intégral (I):**
   Il s'exprime comme l'intégrale de la force appliquée par les particules sur le fluide:

   $$f_i^n = \beta^{IBM} \int_0^t u_{p,i}^n - u_{f@p,i}\ \mathrm{d}t' \tag{A.11}$$

   Cette formulation accumule la force depuis zéro jusqu'à la valeur qui permet d'obtenir $u_{f@p} = u_p$. Naturellement, ce correcteur semble très adapté aux cas laminaires où la force à appliquer tend vers une valeur constante. Dans le cas d'écoulements turbulents, la vitesse du fluide fluctue localement, ce qui empêche le correcteur proportionnel de converger et peut le rendre instable. Il est possible d'améliorer ce comportement en ajustant le coefficient β^{IBM}. En général, β^{IBM} est fixé à une valeur suffisamment grande pour agir comme un filtre passe bas afin que le correcteur ne réagisse pas aux plus petites fluctuations de vitesse du fluide mais seulement aux plus grandes échelles.

L'approche de frontières immergées est très adaptée aux cas laminaires ou faiblement turbulents. Les coefficients α^{IBM} et β^{IBM} doivent être adaptés au cas simulé afin d'imposer de façon plus ou moins raide la condition limite. Si des valeurs trop élevées sont utilisées, le terme source peut faire apparaitre de forts gradients et déstabiliser le calcul. A l'inverse, des coefficients trop faibles ne permettront pas d'imposer une condition de mur étanche.

Bonhomme (2014) montre que les coefficients α^{IBM} and β^{IBM} peuvent être ré-exprimés à partir d'une analyse temporelle en supprimant les termes spatiaux de l'Eq. A.2:

$$\rho\frac{\partial u}{\partial t} = \frac{F_p}{V_m} \tag{A.12}$$

avec F_p la force appliquée par les particules et V_m le volume estimé au noeud. En remplaçant la force volumique par le terme proportionnel, l'expression précédente devient:

$$\rho\frac{\partial u}{\partial t} = \frac{\alpha^{IBM}}{V_m}(u_p - u) \tag{A.13}$$

La solution de cette équation aux dérivées partielles fait apparaitre le temps de relaxation de la particule IBM qui s'exprime comme:

$$\tau_P = \frac{\rho V_m}{\alpha^{IBM}} \tag{A.14}$$

en introduisant le nombre d'itération $N = \tau_P/\Delta t$:

$$\alpha^{IBM} = \frac{\rho V_m}{N\Delta t} \tag{A.15}$$

Une analyse similaire sur le correcteur intégral permet d'obtenir une expression pour β^{IBM}:

$$\beta^{IBM} = \frac{\rho V_m}{M^2\Delta t^2} \tag{A.16}$$

avec M le temps de relaxation du correcteur intégral exprimé en nombre d'itérations $M = \tau_I/\Delta t$. Finalement, l'expression de la force appliquée sur le fluide par les particules devient:

$$f_i^n = \frac{\rho V_m}{N\Delta t}\left(u_{p,i}^n - u_{f@p,i}\right) + \frac{\rho V_m}{M^2\Delta t^2}\int_0^t \left(u_{p,i}^n - u_{f@p,i}\right)\ \mathrm{d}t' \tag{A.17}$$

Les paramètres M et N sont des paramètres fournis par l'utilisateur qu'il convient d'ajuster en fonction du cas étudié. Un nombre d'itérations de relaxation (M ou N) égal à 1 signifie que la consigne de vitesse est imposée en une itération. Dans la pratique, ce cas idéal ne peut être utilisé que dans des cas laminaires. Pour des écoulements turbulents, un nombre d'itérations plus important est nécessaire pour appliquer la consigne. Le terme proportionnel, exprimé en fonction de la dérivée, est par nature réactif aux variations de l'écoulement, tandis que le terme intégral voit un écoulement moyen. Les temps de relaxation sont donc en général fixés tels que le terme intégral applique une force moyenne et le terme proportionnel prend en compte les fluctuations de vitesse. En général N est compris entre 2 et 10 tandis que M est compris entre 50 et 500.

A.5 Validation de la méthode de frontières immergées

Les cas test classiquement utilisés pour la validation de la méthode de frontières immergées ont été réalisés dans le cadre de la thèse de Bonhomme (2014). Ces cas test incluent des écoulement de Poiseuille, de Couette, de plaque plane inclinée et autour d'un cylindre pour lesquels de bons résultats ont été obtenus. Quelques résultats obtenus sur l'écoulement autour d'un cylindre sont d'abord rappelés ici avant de s'intéresser au cas test de Morse *et al.* (1979) classiquement utilisé pour valider les méthodes numériques utilisées pour la simulation de moteurs à piston (Haworth & Jansen, 2000).

A.5.1 Ecoulement autour d'un cylindre

La géométrie étudiée correspond à un domaine rectangulaire au centre duquel se trouve un cylindre fixe de diamètre D (Fig. A.5). L'écoulement traverse le domaine de la droite vers

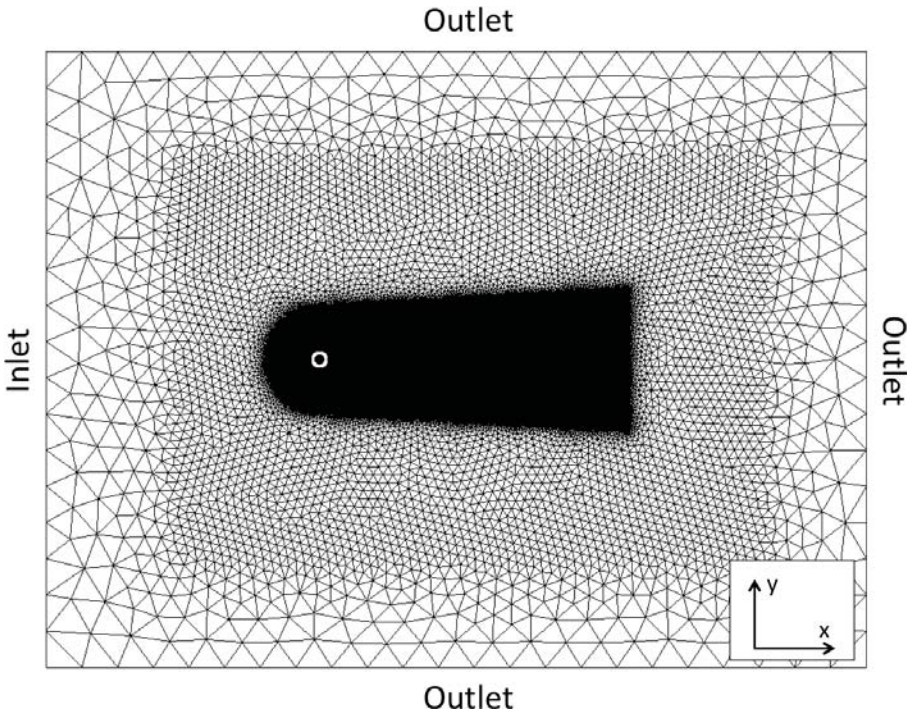

Figure A.5: Géométrie du cas d'écoulement autour d'un cylindre.

la gauche. Les parois supérieures et inférieures sont modélisées par des conditions de sortie tandis que pour le cylindre une condition de mur non glissant est utilisée pour la simulation en maillage conformant ainsi que pour la simulation avec frontières immergées. La figure A.6 permet d'illustrer la différence entre les deux simulations. Avec l'approche IBM, l'écoulement à l'intérieur du cylindre est également résolu. Deux points de fonctionnement sont simulés, un premier cas laminaire avec un nombre de Reynolds basé sur le diamètre du cylindre $Re = 20$ et un second cas transitoire $Re = 100$. Tab. A.1 résume les paramètres des deux cas.

	Re = 20	**Re = 100**
D	2 mm	2 mm
P_0	101325 Pa	101325 Pa
T_0	300 K	300 K
U_{inlet}	$10\,\mathrm{m{\cdot}s^{-1}}$	$10\,\mathrm{m{\cdot}s^{-1}}$
μ	$1.17 \times 10^{-3}\,\mathrm{kg{\cdot}m^{-1}{\cdot}s^{-1}}$	$2.34 \times 10^{-4}\,\mathrm{kg{\cdot}m^{-1}{\cdot}s^{-1}}$

Table A.1: Caractéristiques du cas d'écoulement autour d'un cylindre.

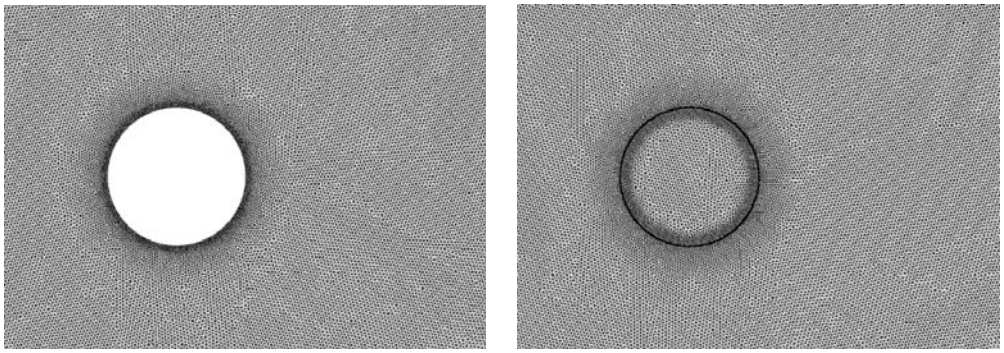

Maillage conforme Frontières immergées

Figure A.6: Zoom sur les maillages utilisés pour le cas d'écoulements autour d'un cylindre. Maillage conformant à gauche et maillage frontières immergées à droite.

A.5.1.a Cas laminaire $Re = 20$

La figure A.7 présente les champs de vitesse et de pression pour les deux méthodes testées. Qualitativement un très bon accord est obtenu entre les deux méthodes aussi bien sur les champs de pression que de température. Pour une comparaison plus qualitative, des profils de vitesse pris en aval du cylindre à $x = 2D$ et $x = 4D$ sont également montrés Fig. A.8 ($x = 0$ correspond au centre du cylindre). Pour la vitesse axiale u ainsi que pour les champs de pression, les deux méthodes donnent les mêmes résultats. Les mêmes conclusions sont obtenues sur les profils de vitesse transverse (Bonhomme, 2014).

A.5.1.b Cas transitoire $Re = 100$

Lorsque le nombre de Reynolds augmente, des lâchés de tourbillons de Von Karman apparaissent dans le sillage du cylindre. Ces tourbillons sont bien reproduits avec les deux méthodes comme illustré Fig. A.9 où sont représentés des iso-contours de vorticité. Dans ce type de configurations, la fréquence des lâchés tourbillonnaires f est caractérisée par le nombre de Strouhal $St = f.D/U_{inlet}$. La transformée de Fourier est utilisée sur le signal de vitesse enregistré par une sonde placée en aval du cylindre pour déterminer la fréquence f. Les résultats des deux simulations ainsi que de plusieurs études similaires publiées dans la littérature sont regroupés dans le Tab. A.2.

Cas	**f_d [Hz]**	**St**
Cas maillage conformant	821	0.164
Cas frontières immergées	827	0.165
Saiki & Biringen (1996)	-	0.171
Shu *et al.* (2007)	-	0.16
Tseng & Ferziger (2003)	-	0.164
Braza *et al.* (1986)	-	0.16

Table A.2: Fréquence de lâchés tourbillonnaires pour le cas test d'écoulement autour d'un cylindre. Comparaison du cas à RE=100 avec les principaux résultats de la littérature.

Les différentes études publiées sur ce cas test trouvent une fréquence de lâchés tourbillon-

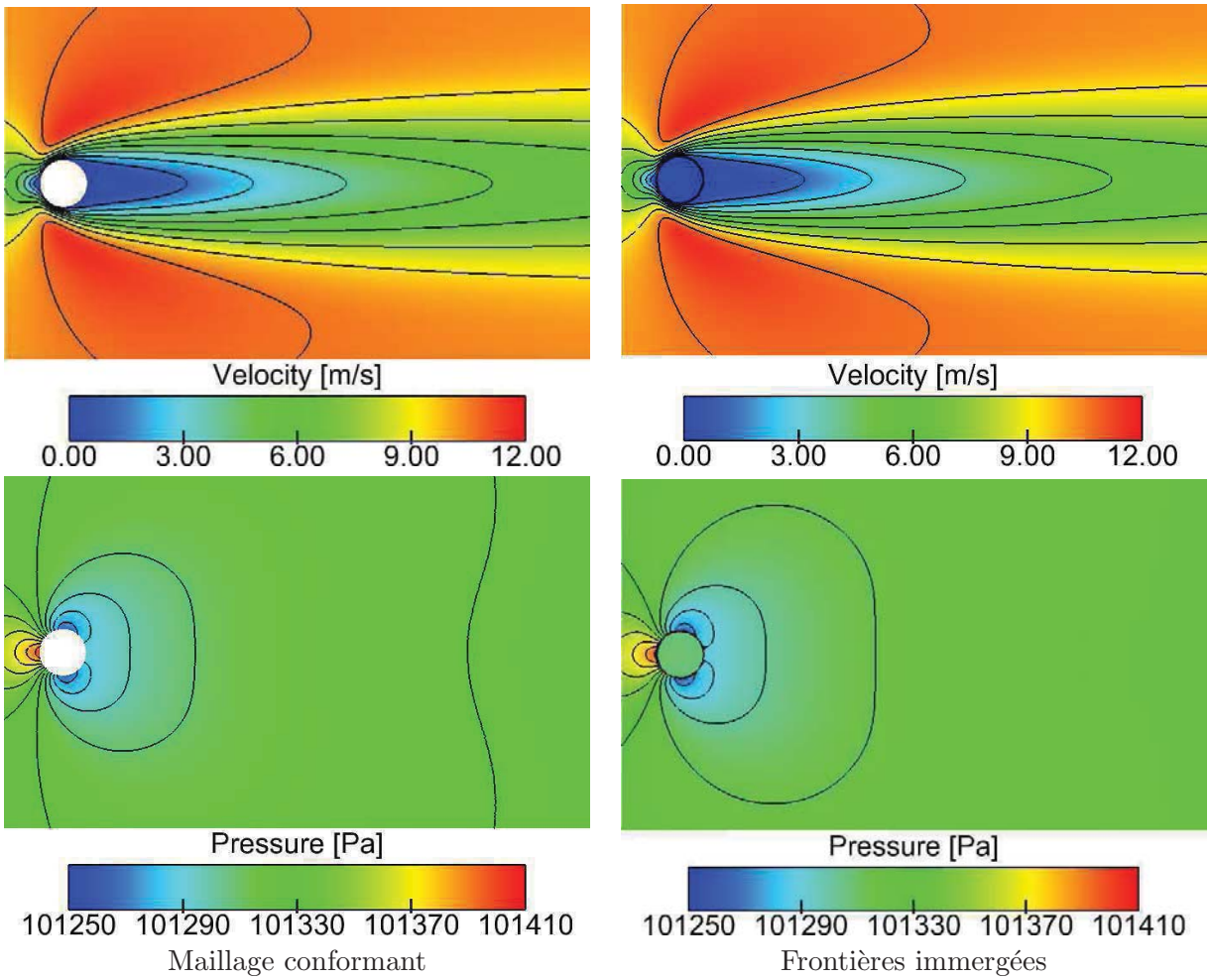

Figure A.7: Comparaison des champs moyens de vitesse et de pression entre les méthodes de maillages conformant et de frontières immergées.

naires adimensionnée comprise entre 0.16 et 0.171. Les valeurs trouvées dans les deux simulations sont très proches et se situent également entre ces deux bornes. Plus de détails sur ce cas test sont disponibles dans la thèse de Bonhomme (2014). De manière générale, la méthode de frontières immergées fournit de très bons résultats dans les différents cas test académiques, bien résolus et à nombre de Reynolds modéré. Avant d'appliquer la méthode à un moteur réel, un cas test intermédiaire de soupape placée dans un écoulement turbulent est investigué dans la prochaine section.

A.5.2 Cas test type Morse et Whitelaw

Ce cas test est une adaptation du cas Morse et Whitelaw, classiquement utilisé pour la validation de simulations numériques de moteurs à piston. Il correspond à un assemblage de deux plénums entre lesquels se trouve une restriction de passage avec une soupape positionnée au col. Une coupe de la géométrie axi-symmétrique est présentée Fig. A.10. Les maillages utilisés pour valider la méthode de frontières immergées sont présentés Fig. A.11. Les tailles de mailles utilisées sont similaires aux maillages utilisés pour les simulations moteur. Les paramètres de

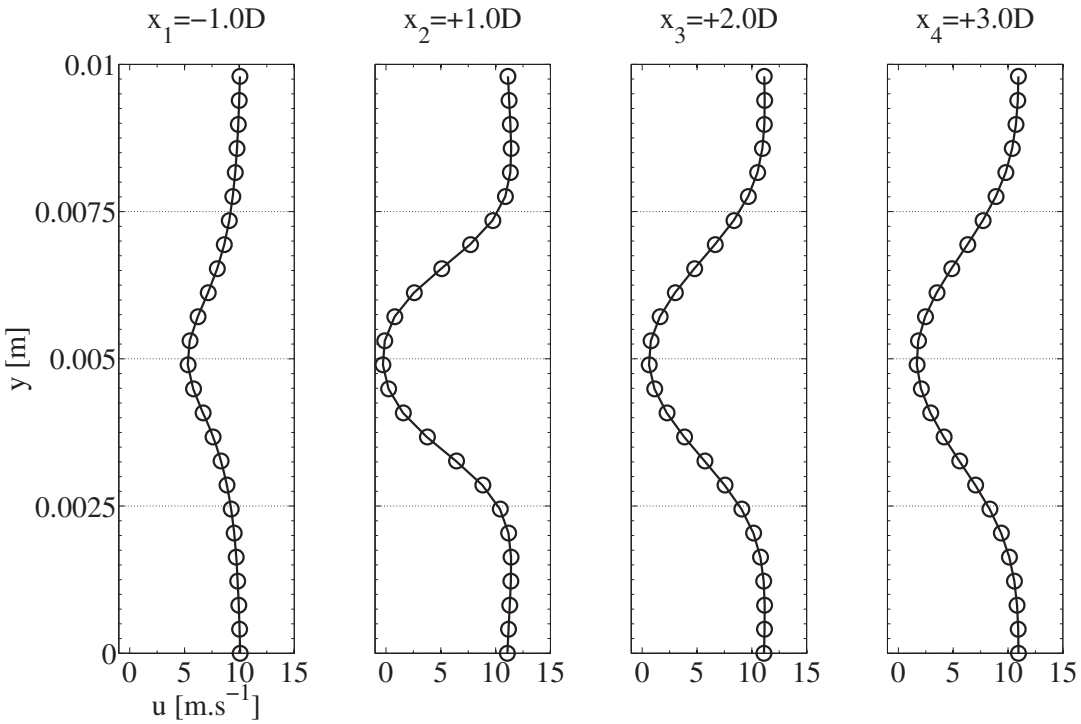

Figure A.8: Vitesse axiale moyenne u. ◯ Maillage conformant ; —— Frontières immergées

maillage sont résumés Tab. A.3. Pour la simulation frontières immergées, 5753 particules sont utilisées de façon à avoir une densité moyenne de une particule par maille. L'objectif ici n'est

	Maillage conformant	Maillage IBM
Nombre de mailles	624 760	667 481
Nombre de noeuds	117 565	122 674
Taille de maille dans le plenum d'admission	4 mm	4 mm
Taille de maille dans le plenum d'échappement	1.8 mm	1.8 mm
Taille de maille au col de soupape	0.8 mm	0.8 mm

Table A.3: Caractéristiques des maillages du cas test Morse *et al.* (1979).

pas de valider la méthode pour remplacer le maillage de la soupape dans une configuration moteur mais d'évaluer la capacité de la méthode à prendre en compte un obstacle de géométrie complexe dans un écoulement représentatif des conditions moteur. Pour cette raison, la soupape reste fixe avec un raffinement du maillage au col de sorte à avoir 8 mailles dans le passage de soupape. Les parois sont modélisées comme des murs adiabatiques non glissants. Des conditions limites non réfléchissantes sont utilisées (Poinsot & Lele, 1992) pour imposer une vitesse de 10 m/s à l'entrée et une pression de 1 bar en sortie.

La figure A.12 montre les champs moyens de vitesse pour les deux simulations. La dynamique générale de l'écoulement est correctement reproduite par la méthode de frontières immergées mais des différences existent. Dans la région située sous la soupape, l'écoulement est altéré par un écoulement résiduel à travers la face inférieure de la soupape et des niveaux de vitesse plus importants sont observés entre les zones de recirculation des jets de soupape. Ces phénomènes

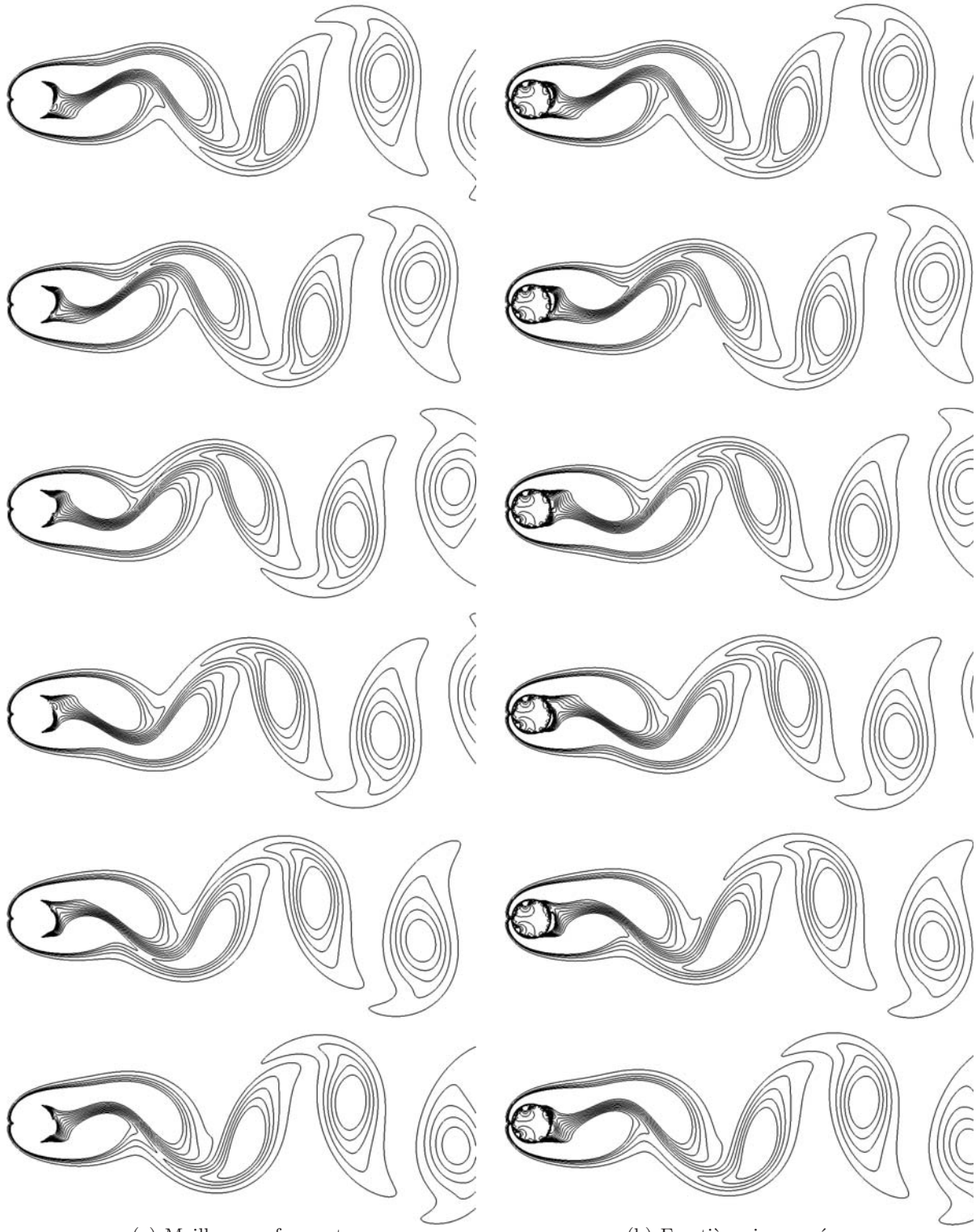

(a) Maillage conformant (b) Frontières immergées

Figure A.9: Iso-contours de vorticité pour une période de lâchés tourbillonnaires sur le cas $Re = 100$.

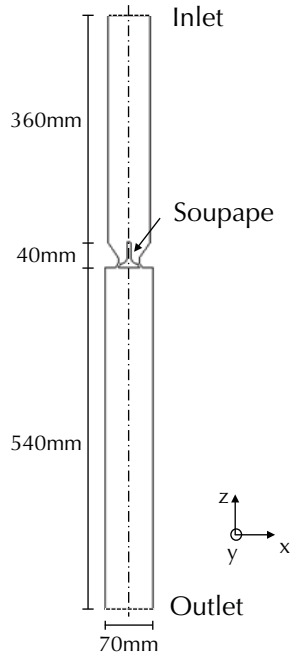

Figure A.10: Configuration du cas test Morse et Whitelaw.

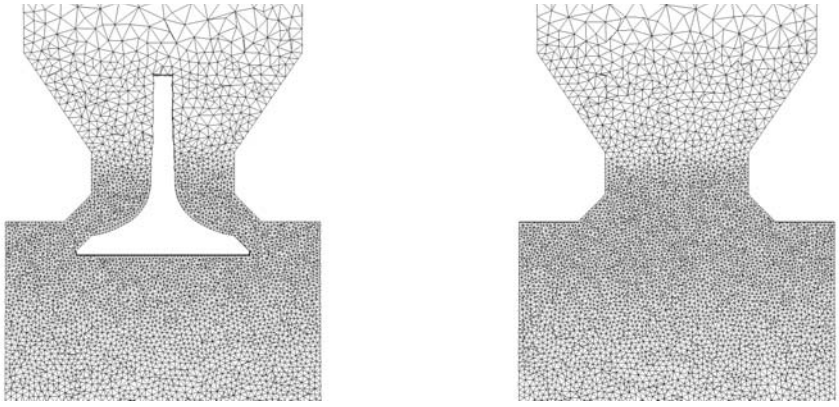

Figure A.11: Maillages de la configuration Morse *et al.* (1979), maillage conformant à gauche et maillage frontières immergées à droite.

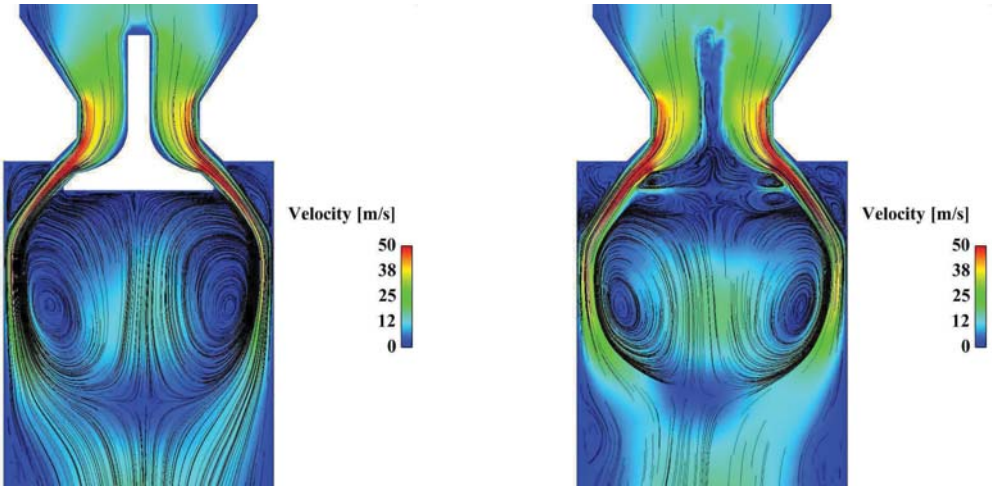

Maillage conforme Frontières immergées

Figure A.12: Champs de vitesse moyenne pour la configuration Morse *et al.* (1979), maillage conformant à gauche et maillage frontières immergées à droite.

sont dus à l'écoulement interne à la soupape qui, bien que non physique, reste simulé avec la méthode IBM. Pour améliorer les capacités de prédiction de la méthode de frontières immergées, une stratégie est mise en place pour laminariser et diminuer l'écoulement à l'intérieur de l'obstacle IBM. Pour ce faire, un traceur représentant le domaine solide, *i.e.* l'intérieur de m'obstacle IBM, est introduit afin de modifier les caractéristiques locales de l'écoulement.

A.5.3 Traceur du domaine solide sur le champ Eulerien

Pour modifier localement les propriétés de l'écoulement en fonction de l'appartenance ou non d'une cellule au domaine solide, un traceur Ψ est utilisé. L'algorithme suivant est utilisé pour déterminer la valeur du champ Ψ:

1. Les coordonnées du vecteur normal au mur à modéliser en chaque particule sont calculées et sauvegardées avec les informations de la particule.
2. A l'initialisation du calcul, pour chaque cellule contenant une particule de force, un produit scalaire est réalisé pour connaitre la position de chaque noeud de la cellule par rapport au mur à modéliser. La figure A.13 illustre cette étape: le produit scalaire est effectué entre le vecteur particule-noeud et le vecteur normal au mur, orienté vers le domaine fluide. Un produit scalaire positif signifie que le noeud est positionné dans le domaine fluide tandis qu'un noeud situé dans le domaine solide sera discriminé par un produit scalaire négatif.
3. La dernière étape vise à propager l'information à l'intérieur du solide. Pour ce faire, une boucle sur toutes les cellules du maillage est réalisée plusieurs fois et un test est effectué sur les valeurs du champs Ψ dans la cellule. Les conditions de propagation sont regroupées Tab. A.4. Plusieurs itérations de propagation du champs Ψ sont réalisées jusqu'à atteindre la condition d'équilibre $\sum_{N_{nodes}} \Psi = K$ avec N_{nodes} le nombre de noeuds total du maillage et K une constante.

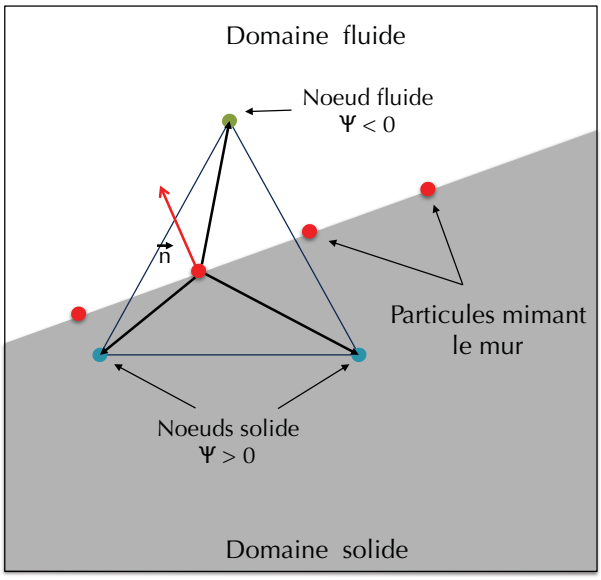

Figure A.13: Exemple 2D de la définition du champ Ψ pour chaque cellule contenant des points de force.

Test	Valeur Ψ imposée	Signification
$\max(\Psi) = \min(\Psi)$	-	la cellule contient des noeuds appartenant au fluide et au solide
$\sum_{N_{vert}} (\Psi) >= 2 \max(\Psi)$	$\max(\Psi)$	la cellule ne contient que des noeuds solides
$\sum_{N_{vert}} (\Psi) <= 2 \min(\Psi)$	$\min(\Psi)$	la cellule ne contient que des noeuds fluides

Table A.4: Conditions de propagation du champs Eulerien de points de force IBM Ψ. N_{vert} représente le nombre de noeuds dans chaque cellule.

Le champ Ψ obtenu pour la soupape du cas Morse *et al.* (1979) illustré Fig. A.14 donne une idée de la soupape telle qu'elle est vue par l'écoulement avec cette méthode. Il apparait clairement que la résolution du maillage joue un rôle important dans la précision de cette méthode. Il n'est pas possible avec cette méthode de représenter des détails plus petits que la taille de maille. Il faut cependant noter que la méthode de projection des forces est pondérée par la distance noeud-particule. La figure A.14 donne donc une idée détériorée de la soupape vue par l'écoulement.

A.5.4 Résultats du cas Morse *et al.* (1979) avec champ Eulerien IBM

Afin de réduire localement l'écoulement dans la soupape, le champ Ψ est utilisé comme un senseur de viscosité artificielle. Une viscosité $\nu_m = 10\ \nu_{lam}$ est utilisée pour les points de maillage où $\Psi > 0$. Les champs de vitesse moyenne et fluctuante sont présentés Fig. A.15. Une nette amélioration des résultats est obtenue grâce à l'augmentation de la viscosité dans la soupape mais certaines différences subsistent. La dynamique globale de l'écoulement semble correctement captée avec la méthode de frontières immergées, les vitesses au niveau du col

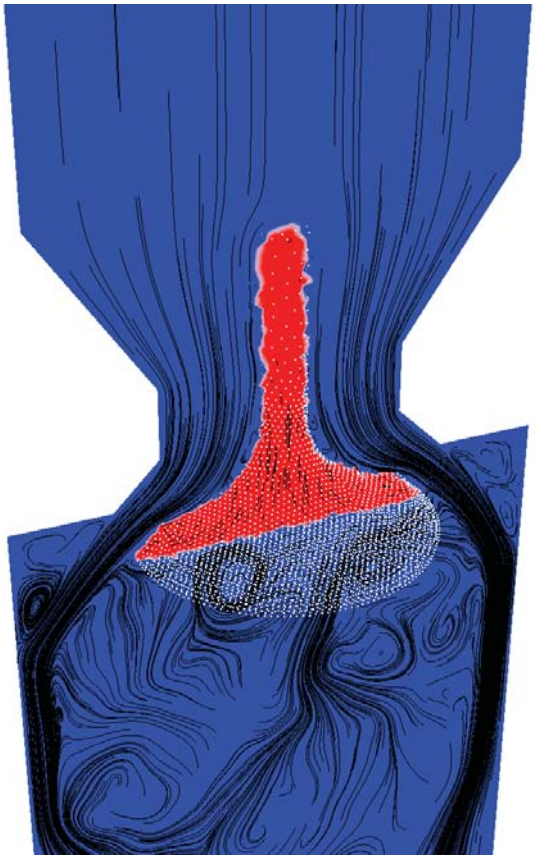

Figure A.14: Champ Eulerien Ψ des points de force de la soupape sur le cas Morse *et al.* (1979).

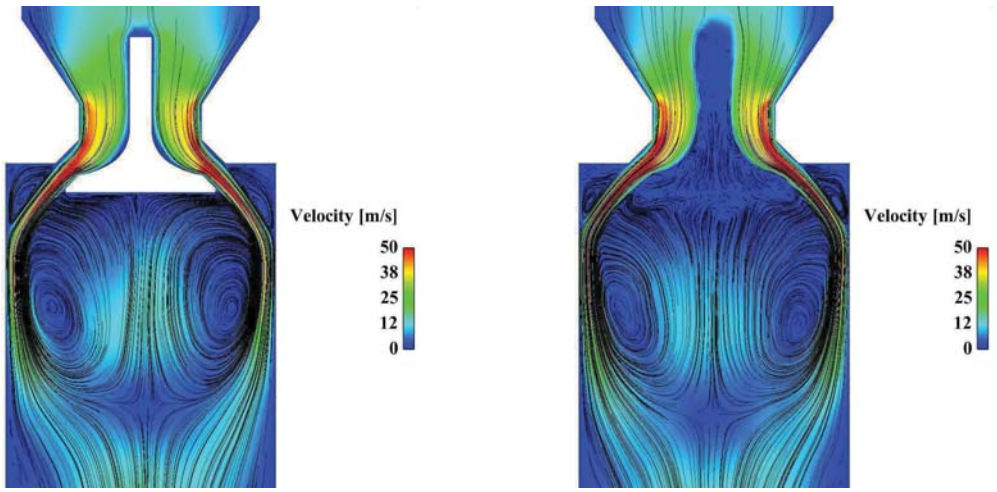

Maillage conforme Frontières immergées

Figure A.15: Comparaison des champs de vitesse moyenne et fluctuante entre un maillage conformant et frontières immergées sur le cas Morse *et al.* (1979).

semblent identiques ainsi que la pénétration des jets de soupapes. Cependant, au niveau de la tige de soupapes, la zone de vitesse nulle semble plus importante et la zone de recirculation située sous la soupape apparait moins intense que dans le cas de maillage conformant. Pour ce qui est de la région de la tige de soupapes, la différence peut être imputée à l'utilisation d'un maillage grossier comparé au diamètre de la tige. Cependant, en comparaison à la précédente simulation frontières immergées, une nette amélioration est obtenue. L'écoulement dans la tige de soupape est fortement réduit ce qui permet de réduire la porosité du mur sous la soupape. Pour une comparaison plus quantitative, les profils de vitesse pour différentes abscisses dans le cylindre (Fig. A.16) sont tracés Fig. A.17.

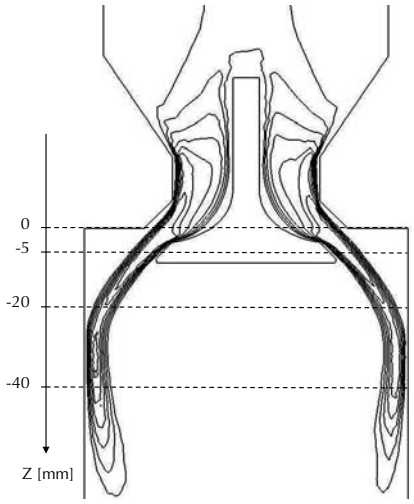

Figure A.16: Positions des profils de vitesse tracés Fig. A.17 sur le cas Morse *et al.* (1979).

Aussi bien pour les vitesses moyennes que pour les fluctuations, les deux simulations sont en bon accord. Seules de très légères différences sont à noter: les profils de vitesse moyenne montrent une ouverture des jets de soupape légèrement surestimée avec la méthodologie de frontières immergées (notamment à la position $z = -20mm$). A la position $z = -5mm$, un écart notable est également trouvé sur les fluctuations de vitesse entre les deux simulations mais le manque de symétrie dans les profils laisse penser que cet écart est dû à un manque de convergence des statistiques. Enfin, pour comparer les résultats obtenus avec et sans la description Eulerienne du champ de particules, la Fig. A.18 compare les vitesses de glissement du fluide sur les particules. La vitesse de glissement correspond à l'écart entre la consigne de non glissement voulue et la condition réellement imposée par la méthode frontières immergées. Les résultats montrent une nette amélioration avec description Eulerienne du solide (cas B) en comparaison au cas sans cette description (cas A). Dans le cas B, les oscillations du glissement maximal dues aux fluctuations turbulentes sont très nettement diminuées. De même, le glissement moyen sur les particules est diminué de quelques dixièmes mètres par seconde dans le cas A à environ 1.10^{-3} m/s dans le cas B. Dans l'ensemble, la méthode frontières immergées avec description Eulerienne semble fournir de très bons résultats sur ce cas test avec un surcoût très faible (inférieur à 0.5% du temps CPU total). Cette méthode a donc été retenue pour modéliser la modification de la géométrie des tubulures d'admission du moteur ECOSURAL en conservant les maillages initiaux.

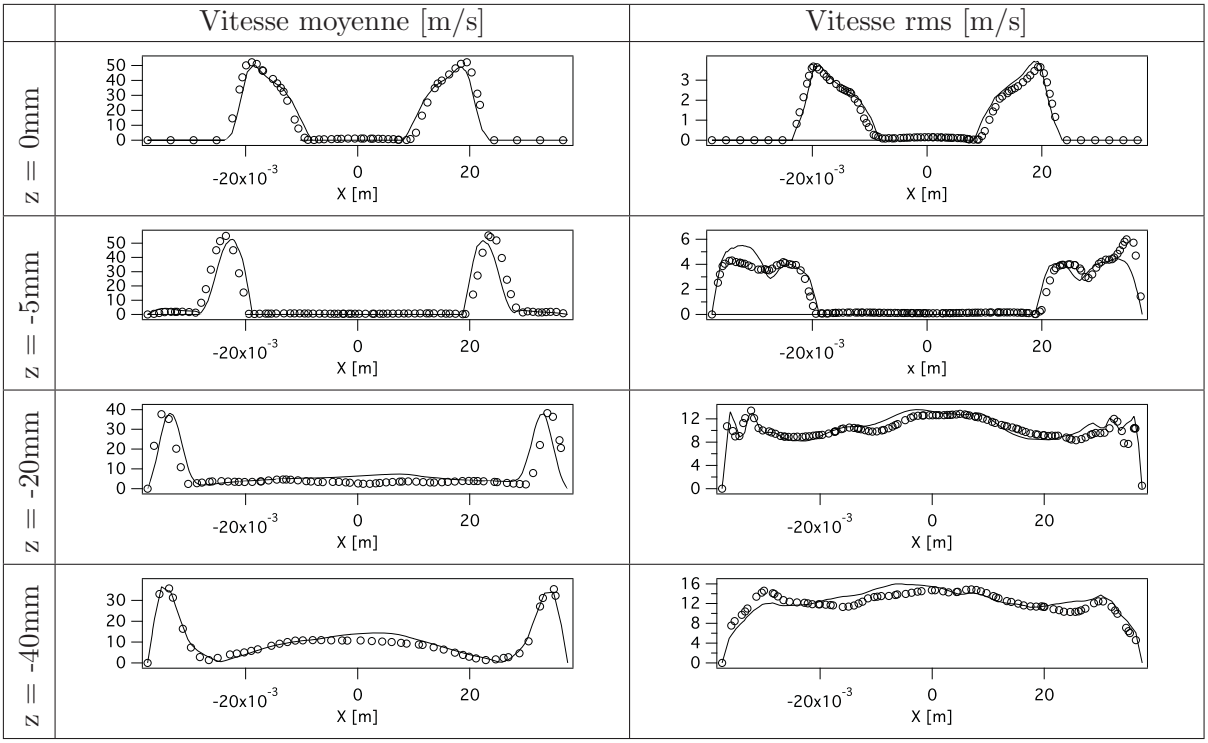

Figure A.17: Comparaison des profils de vitesse moyenne et fluctuante entre un maillage conformant et frontières immergées sur le cas Morse *et al.* (1979).

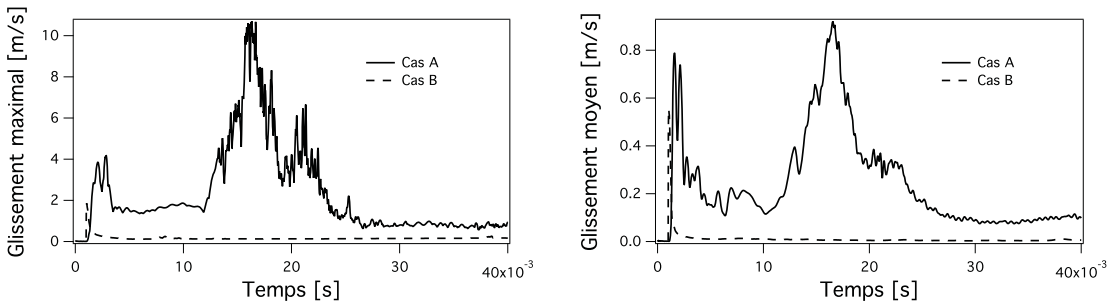

Figure A.18: Vitesses de glissement maximal à gauche et moyen à droite sur les particules. Le cas A correspond au cas sans description Eulerienne et le cas B avec description Eulerienne du champ du domaine solide.

A.5.5 Frontières immergées pour modéliser les parties mobiles en configuration moteur à piston?

Bien que certaines simulations numériques de moteurs à piston utilisent le formalisme IBM pour représenter les parties mobiles de la géométrie (Verzicco *et al.*, 2000; Naitoh *et al.*, 2002, 2004), l'approche de déformation de maillage a été retenue dans *AVBP* pour s'affranchir des difficultés inhérentes à l'utilisation de cette méthode. En particulier, le cas test issu de Morse *et al.* (1979) a mis en évidence la difficulté d'imposer une étanchéité parfaite à travers les frontières immergées. Cette étanchéité est par exemple importante lors des phases de simulation soupapes fermées pour prédire les bons niveaux de pression dans le cylindre. De plus, en dépit de l'utilisation d'un maillage non conforme, il n'est pas possible avec la méthode de frontières immergées de rendre compte des détails géométriques plus petits que la taille de maille. Par exemple, dans le cas du moteur ECOSURAL, la géométrie de la tête de soupape présentée Fig. A.19 présente des détails

Figure A.19: Caractéristiques géométriques de la tête de soupape d'échappement du moteur ECOSURAL.

de l'ordre de 0.3 mm qui jouent un rôle important dans la dynamique des jets de soupapes. Ces détails nécessitent donc l'utilisation d'un maillage très fin, non seulement à la position de la soupape, mais également dans tous les lieux de passage de la soupape afin de rendre compte de ces détails pendant l'intégralité des phases d'admission ou d'échappement. En se basant sur le volume balayé par les soupapes, le surcoût en terme de nombre de mailles est de l'ordre de la dizaine de millions de mailles, soit la taille des plus gros maillages utilisés. Ce raffinement est pénalisant à double titre: en plus des points de maillage supplémentaires à calculer, les mailles supplémentaires étant de taille plus petite que les plus petites mailles utilisées pendant les phases de déplacement de soupapes d'un facteur compris entre 2 et 3, le pas de temps de la simulation est pénalisé par ce même facteur. Au final, malgré une complexité légèrement plus importante, la méthode ALE actuellement retenue est nettement plus intéressante en termes de temps de calcul et de précision des résultats. La méthodologie de frontières immergées semble donc une bonne solution pour évaluer des différences géométriques non mobiles mais l'approche ALE, largement validée dans *AVBP*, reste la méthode privilégiée pour modéliser les parties mobiles de la géométrie.

APPENDIX B

Article sur le modèle IPRS présenté au *35th Symposium (Int) on Combustion*

Introduction

Cette annexe est constituée de l'article présentée au *35th Symposium (Int) on Combustion* (San Francisco, CA). Il décrit le modèle d'auto-allumage IPRS, présente les résultats de validation sur les cas simples homogènes ainsi que l'analyse d'auto-allumage de point chaud selon la théorie de Zeldovich (1980).

ARTICLE IN PRESS

Available online at www.sciencedirect.com

ScienceDirect

Proceedings of the Combustion Institute xxx (2014) xxx–xxx

Proceedings of the Combustion Institute

www.elsevier.com/locate/proci

A methodology based on reduced schemes to compute autoignition and propagation in internal combustion engines

Antony Misdariis [a,b,*], Olivier Vermorel [b], Thierry Poinsot [c]

[a] Renault SAS, 1 Allée Cornuel, 91570 Lardy, France
[b] CERFACS, CFD Team, 42 Avenue G. Coriolis, 31057 Toulouse Cedex 01, France
[c] Institut de Mécanique des Fluides de Toulouse, CNRS, Avenue C. Soula, 31400 Toulouse, France

Abstract

The prediction of autoignition (AI) delay is an essential prerequisite to account for abnormal combustions (e.g. knock or super knock) that can appear in Internal Combustion (IC) engines. In this paper, a simple model called Ignition to Propagation Reduced Scheme (IPRS) is proposed to add AI predictions in reduced chemical schemes, which are classically used to compute in-cylinder combustion in the context of Large Eddy Simulations (LES). The IPRS principle is to use a single two-reaction reduced scheme and adapt the pre-exponential factor of the fuel oxidation reaction as a function of the temperature: one value is used at low temperatures to correctly predict AI delays and an other one can be used at higher temperatures, where heat release occurs, to keep the flame propagation properties of the chemical scheme. After a first section that introduces the model, Perfectly Stirred Reactors and 1D flames simulations are used to verify that: (1) the modification of the pre-exponential constant of the Arrhenius law at low temperature does not alter the propagation properties of the reduced scheme and (2) this modification is sufficient to accurately predict AI delays. The IPRS model captures autoignition times exactly like a full chemical scheme in a compressed zero dimensional test case representative of engine compression. In the last section this model is applied to 1D single hot spot simulations to investigate the modes of reaction after autoignition.

Keywords: LES; Knock; Autoignition; Internal combustion engine; Reduced scheme

1. Introduction

During the last decade engine downsizing has revealed to be a useful path to improve the efficiency of Internal Combustion (IC) engines. This technique allows to operate engines in a zone of higher efficiency by reducing the cylinders size and by increasing the pressure inside the chamber thanks to turbo chargers. It is commonly used in the industry up to a downsizing level of about 25%. Beyond this level abnormal combustions such as knock or super knock start occurring due to the high pressure and temperature conditions inside the cylinder. Understanding abnormal combustions is a main field of research inside the IC engine

* Corresponding author at: CERFACS, CFD Team, 42 Avenue G. Coriolis, 31057 Toulouse Cedex 01, France. Fax: +33 0 5 61 19 30 00.
E-mail address: misdariis@cerfacs.fr (A. Misdariis).

http://dx.doi.org/10.1016/j.proci.2014.06.053
1540-7489/

community in order to reach higher levels of downsizing. Previous studies [1–3] proved that LES is a powerful tool able to reproduce unsteady phenomena occurring in piston engines. However, to study abnormal combustion in IC engines, a model able to accurately predict Auto-Ignition (AI) delays has to be added to the LES solver. Because of the complexity of low temperature kinetics [4–7], most modeling approaches rely on tabulation of ignition delays obtained from zero dimensional ignition computations [8] or from representative 1D flamelets [9]. Some reduced schemes compatible with LES (limited to a few reactions and species) for the primary reference fuels are also available [10,11] but they are limited to the AI delay prediction and have to be associated to other models for high temperature reactions. Here an alternative solution is explored: a single two-step reduced scheme is used to describe both AI and propagation. It is called IPRS (Ignition to Propagation Reduced Scheme). The scope is not to reproduce the complex path of chemical reactions leading to AI but only to tune the reduced scheme reactions such that the AI delay is the same as the one obtained with complex chemistries. The model is introduced in the next section and validated on AI cases and 1D premixed flames. Homogeneous zero dimensional flow elements representative of IC engine are then simulated where complex chemistries AI delays are available to assess the accuracy of the IPRS model. In the last section the model is applied to non-homogeneous cases where autoignition phenomena can lead to detonation. The paper focuses on two fuels (pure isooctane and a gasoline surrogate called Sur95t in Pera et al. [12]) but the methodology can be extended to other fuels.

2. Predicting autoignition delay with a two-step chemistry

In reactive LES the source terms $\dot{\omega}_T$ and $\dot{\omega}_k$ in the energy and the species conservation equations have to be closed. For a mechanism including M reactions between N reactants and with W_k the molar weight of species k:

$$\dot{\omega}_k = \sum_{j=1}^{M} \dot{\omega}_{kj} = W_k \sum_{j=1}^{M} \nu_{kj} Q_j \tag{1}$$

where $\nu_{kj} = \nu''_{kj} - \nu'_{kj}$ is the global stoichiometric coefficient of species k in reaction j. The progress rate Q_j is defined by:

$$Q_j = K_{f,j} \prod_{k=1}^{N} \left(\frac{\rho Y_k}{W_{kj}}\right)^{\nu'_{kj}} - K_{r,j} \prod_{k=1}^{N} \left(\frac{\rho Y_k}{W_k}\right)^{\nu''_{kj}} \tag{2}$$

In this relation ρ is the density, Y_k represents the species mass fractions and $K_{f,j}$ (respectively $K_{r,j}$) is the forward (respectively reverse) rate of reaction j obtained with the Arrhenius law:

$$K_{f,j} = T^{\beta_j} A_{f,j} \exp\left(-\frac{E_{a,j}}{\mathcal{R}T}\right) \tag{3}$$

with R the perfect gas constant, T the temperature, $A_{f,i}$ the pre-exponential constant, $E_{a,j}$ the activation energy and β_j the temperature exponent. For propagating flames the most important parameters that have to be accurately predicted by the source term closure are the laminar flame speed S_L^0, the flame thickness δ_L^0 and the adiabatic flame temperature T_{ad}. Single-step chemical schemes can provide an accurate description of flame propagation process but they can not predict the burned gas temperature over a wide range of equivalence ratios because it depends on the species enthalpies. A simple solution to this problem has been used in the gas turbine community [13,14] by adding a reversible reaction between CO and CO_2. This is sufficient to capture both flame speed and adiabatic temperature over all relevant compositions. The resulting two-step schemes family can be written:

$$C_xH_{2x+2} + \left(x + \frac{x+1}{2}\right)(O_2 + aN_2) \rightarrow \quad xCO_2 + (x+1)H_2O + \left(x + \frac{x+1}{2}\right)aN_2 \tag{4}$$

$$CO + \frac{1}{2}O_2 \rightarrow CO_2 \tag{5}$$

Table 1 summarizes the Arrhenius coefficients of the two-step mechanism classically used to compute isooctane/air flames propagation. The reaction exponents differ from the stoichiometric coefficients and are adjusted to obtain the right dependence of the flame speed in pressure. This scheme was designed to reproduce the Hasse et al. experiments [15]. Reduced schemes are widely used and several authors point out their accuracy in a wide range of configurations [2,16]. However they obviously fail to capture AI delays which are driven by low temperature chain reactions and the chemistry of radicals such as alkylperoxy or hydroperoxyalkyl [4–7]. All studies show a correlation between the AI delay τ_{AI} and the pre-exponential of the Arrhenius law:

$$\tau_{AI} \sim \frac{1}{A_{f,j}} \exp\left(\frac{E_{a,j}}{\mathcal{R}T}\right) \tag{6}$$

Table 1
Arrhenius parameters for the C_8H_{18}/air scheme.

	C_8H_{18} oxidation		CO–CO_2 equilibrium	
E_a [cal/mol]	$3.6 \cdot 10^4$		$1.4 \cdot 10^5$	
A [cm^3/mol]	$5.443 \cdot 10^{12}$		$2.0 \cdot 10^5$	
β_j [−]	0.1		0.0	
Reaction exponents [−]	$n_{C_8H_{18}}$	1.1	n_{CO}	1.00
	n_{O_2}	0.54	n_{O_2}	0.50

Please cite this article in press as: A. Misdariis et al., *Proc. Combust. Inst.* (2014), http://dx.doi.org/10.1016/j.proci.2014.06.053

Equation (6) suggests that a simple adjustment of the pre-exponential constant $A_{f,j}$ may give correct predictions of AI delays, even for basic chemical schemes. Of course, the values of the pre-exponential constant A_{prop} that ensure the right laminar flame speed S_L^0 and the values A_{AI} that will provide the right AI delay are different but the two modes of combustion previously described (i.e. propagation and AI) are driven by processes occurring in two different ranges of temperature: AI is initiated at low temperatures while the flame propagation is mainly driven by high temperature mechanisms. In order to predict both propagation and AI with a reduced mechanism, the idea of IPRS is to take advantage of this decoupling in temperature and make the pre-exponential constant vary with temperature (Fig. 1):

$$A_{f,j} = A_{AI} + (A_{prop} - A_{AI})\left[\frac{1+\tanh\left(\frac{T-T_c}{\sigma}\right)}{2}\right] \qquad (7)$$

T_c is the cross-over temperature where $A_{f,j}$ goes from A_{AI} to A_{prop}. σ is a parameter introduced to adjust the steepness of the constant change with temperature. The idea of making chemical constants change with the local conditions is not new [17–19] but it is introduced here to capture both AI and propagation in an IC engine. Of course, such a reduced scheme will not reproduce all details of an actual AI process and in particular the cold flame phenomena but the AI delay will match the one computed with complex chemistry as shown in Fig. 2. Note that methods based on tabulation of AI times are also limited to the objective of correctly capturing the AI delays and nothing more. One advantage of IPRS is that the same chemical scheme can be used during the whole combustion process, avoiding to couple two models as often done with tabulation techniques: one before AI (using tabulated times) and another one after ignition.

The methodology followed to determine A_{AI} is to first characterize each fuel in terms of AI times over the range of pressure and temperature of interest using complex chemistries and a set of Perfectly Stirred Reactors (PSR) computations

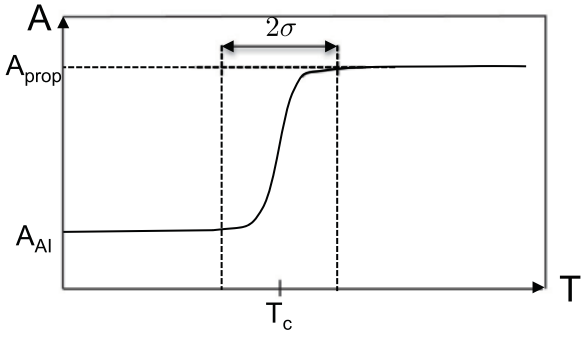

Fig. 1. Schematic of the evolution of the pre-exponential constant across the flame front with the IPRS model.

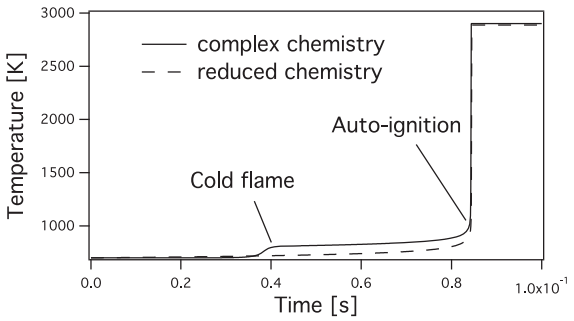

Fig. 2. Temperature evolution in a stoichiometric Perfectly Stirred Reactor with a complex chemistry and IPRS for isooctane at $T_1 = 700$ K and $P_1 = 11$ bar.

with a 0D chemistry software. In the present study Cantera was used [20]. The complex schemes used as reference are presented in Table 2. The reference AI delays for isooctane and for the gasoline surrogate are shown in Fig. 3. A series of AI delays is then computed with the two-step mechanism under the same conditions of pressure and temperature to find the values of the pre-exponential constant A_{AI} that will predict the same AI time as the complex chemical scheme. Finally, the A_{AI} values of the pre-exponential constant are tabulated as a function of temperature and pressure of the fresh gas to be used in the 3D LES solver. For isooctane, the table used for the pre-exponential constant of the fuel oxidation reaction (Eq. (4)) to predict AI delays is presented in Fig. 4 while the standard constant from Table 1 is used for the propagation. The tabulation is only performed here versus pressure and temperature because, in the target application, the charge is perfectly premixed but the method can easily include the effect of other parameters such as dilution or equivalence ratio.

An other difficulty arises when applying this model to a configuration with variable volume such as IC engines: the initial pressure and temperature can not be used to read the A_{AI} table because the AI delay is affected by compression and expansion. Using local and instantaneous conditions is not a solution either because the very small heat release that occurs even before AI may change the local temperature. This may be particularly critical if the temperature falls within the Negative Temperature Coefficient (NTC) zone, where small variations of temperature can lead to very different A_{AI}. To obtain the right value

Table 2
Complex chemistry mechanisms used as reference for the IPRS method.

	N species	N reactions
Jerzembeck [21]	104	403
Anderlhor [22]	538	3000

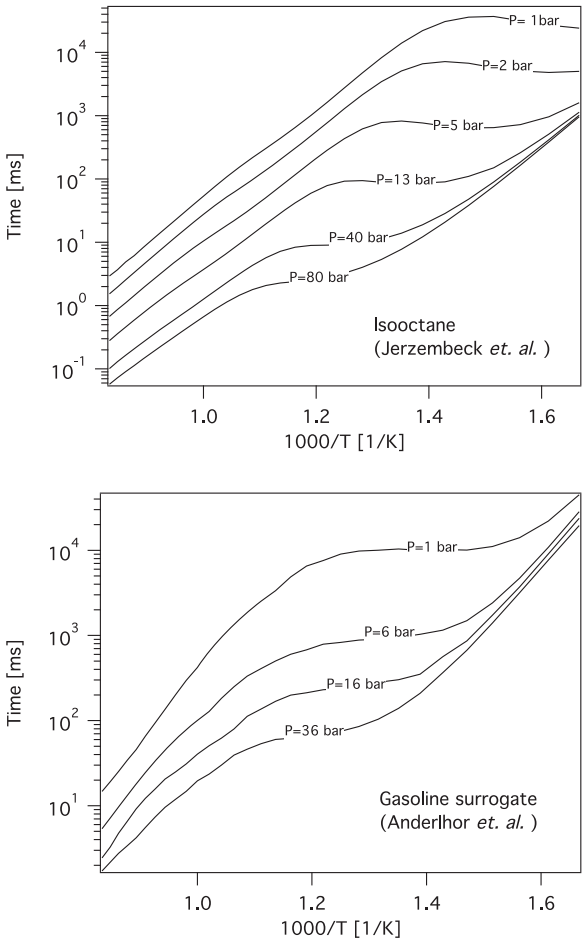

Fig. 3. AI times of isooctane (top) and gasoline surrogate (bottom) in PSR with complex chemistries.

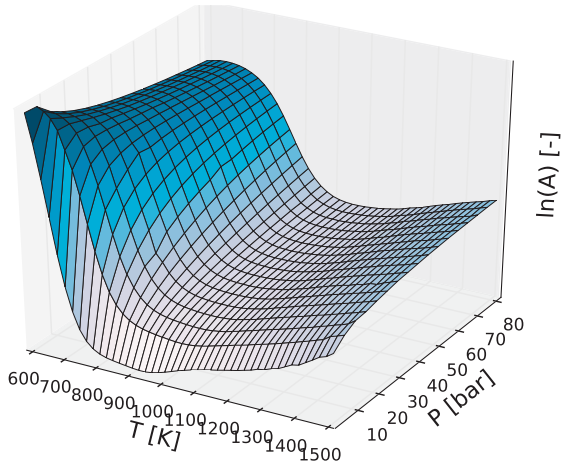

Fig. 4. Pre-exponential constant A_{AI} table used in the 3D LES solver and designed to reproduce the AI delays of isooctane.

for A_{AI}, an estimation of the fresh gas temperature must be used. Here a method similar to the one used in the TKI model [8] is implemented. It consists in the transport of the fresh gas enthalpy with sources terms accounting for heat transfers.

3. Test cases and validation

The IPRS approach is first tested by computing (1) laminar premixed flame speeds (Section 3.1) and (2) AI times (Section 3.2). For both cases, the IPRS two-step scheme is compared to the complex schemes of [21,22] for isooctane or gasoline/air flames. All computations are performed with Cantera.

3.1. Laminar premixed flame speed

To evaluate the capacity of the IPRS scheme to correctly predict laminar flame speeds and determine the proper value of the cross-over temperature T_c used to change the pre-exponential constant, a series of stoichiometric premixed laminar isooctane/air flames was computed for a fresh gas temperature T_1 of 800 K and pressures P_1 varying from 1 bar to 40 bar. Figure 5 shows the laminar flame speed obtained with the IPRS scheme, normalized by its exact value (obtained with the complex scheme) as a function of the normalized cross-over temperature $\theta_c = (T_c - T_1)/(T_2 - T_1)$, with T_2 the burned gas temperature. As soon as θ_c is less than 0.2, the IPRS flame speed matches its exact (complex scheme) value, showing that the pre-exponential constant can, indeed, be modified at low temperature without affecting the flame speed. Another way to verify that $\theta_c = 0.2$ is the cross-over temperature limit to correctly predict the flame propagation is to plot the reduced reaction rate $\dot{\omega}_r$ as a function of the reduced temperature θ in Fig. 6 for a 1D premixed flame. On the same graph, the pre-exponential constant $A_{f,j}$ is plotted as a function of the reduced temperature for the same 1D flame with the IPRS model and $\theta_c = 0.15$: in conditions where $A_{f,j}$ is altered by the IPRS model, i.e. for $\theta < 0.2$, the reaction rate is almost equal to zero. As described in [23], this zone corresponds to the pre-heating zone mainly driven by convection and heat diffusion where the Arrhenius constants play no role. When the heat release starts increasing, $A_{f,j}$ is back to A_{prop} which provides the right propagation properties. $\theta_c = 0.15$ is used for the rest of this work.

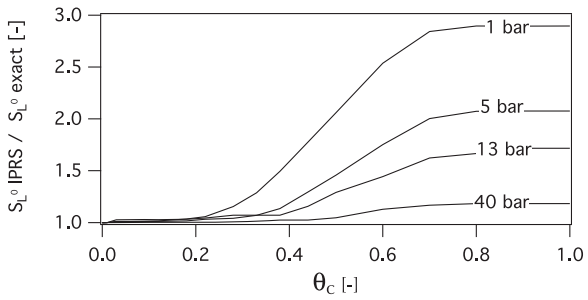

Fig. 5. Normalized laminar flame speed obtained with the IPRS model as a function of the reduced cross-over temperature $\theta_c = (T_c - T_1)/(T_2 - T_1)$. Stoichiometric isooctane/air flames, $T_1 = 800$ K.

Please cite this article in press as: A. Misdariis et al., *Proc. Combust. Inst.* (2014), http://dx.doi.org/10.1016/j.proci.2014.06.053

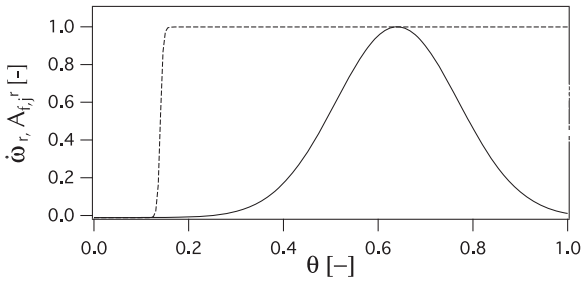

Fig. 6. Reduced reaction rate of the fuel oxydation reaction $\dot{\omega}_r = \dot{\omega}/max(\dot{\omega})$ (solid line) and reduced pre-exponential constant $A^r_{f,j} = (A_{f,j} - A_{prop})/(A_{AI} - A_{prop})$ (dashed line) along a 1D stoichiometric isooctane/air laminar flame with $\theta_c = 0.15$.

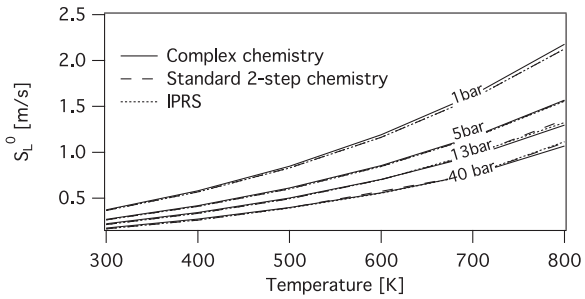

Fig. 7. Comparison of 1D stoichiometric isooctane/air laminar flame speed with complex chemistry, the standard two-step chemistry and the IPRS model.

Table 3
Geometrictal specifications of the compressed cylinder.

Bore	[mm]	86
Stroke	[mm]	82
Connecting rod length	[mm]	137
Compression ratio	[–]	6.32
Engine rotation speed	[rpm]	1200

A new set of 1D flames is then computed to evaluate the model with T_1 varying from 300 K to 800 K and P_1 varying from 1 bar to 40 bar to check the behavior in IC engine like conditions. Results are compared to the same 1D flames computed without the AI model (i.e. with $A_{f,j}$ constant and equal to A_{prop}) and to Cantera computations performed with the complex schemes of Table 2. Figure 7 shows that the differences between the three computations are almost negligible over the whole range of temperature. These results thus validate the assumption that a modification of the pre-exponential constant at low temperatures does not affect the propagation behavior as long as the right constant A_{prop} is used in the range of temperature where heat release occurs i.e. for $\theta > 0.2$.

3.2. Autoignition delays

The AI delays predicted by the IPRS model are compared now to the complex schemes results. A first series of stoichiometric PSR are computed

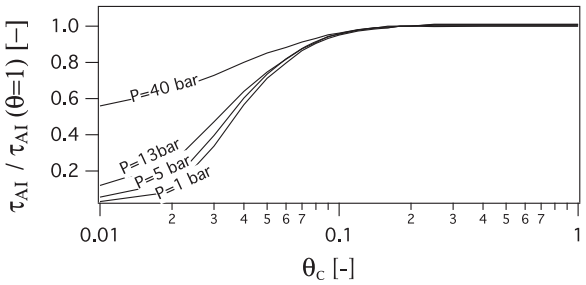

Fig. 8. Non-dimensional AI delay as a function of the reduced cross-over temperature $\theta_c = (T_c - T_1)/(T_2 - T_1)$.

with an initial temperature T_1 of 800 K and an initial pressure P_1 ranging from 1 to 40 bar. For each case the sensitivity of the AI delay to the cross-over temperature T_c is evaluated. Figure 8 shows that for all pressures, if T_c is chosen such that $\theta_c > 0.1$ the error on the AI delay is less than 5% and for $\theta_c = 0.15$, less than 2%. This confirms that the value $\theta_c = 0.15$ chosen in Section 3.1 is a good trade off. This value is retained in the following to compute AI delays under a wide range of pressure and temperature. As shown in Fig. 9, for both fuels, the AI delays predicted by the IPSR model are very close to the ones predicted by the complex schemes of [21,22]. Even the NTC zone of isooctane (when $P < 15$ *bar*) is correctly captured with this approach, demonstrating that a very simple chemical description can be efficient if (1) it is tuned on a complex chemistry scheme and (2) the objective is to capture AI delays only (no cold flame details). Note that, of course, the CPU cost of such an approach is extremely low compared to all other methods.

4. Validation in a compressed zero dimensional autoigniting flow

In order to evaluate the ability of the IPRS model to predict AI events in IC engines, a simplified configuration representing the compression of a flow element typical of a piston engine is computed. This test case corresponds to a zero dimensional evolution of a compressed flow where the initial composition corresponds to a premixed gasoline/air mixture. This mixture is compressed following a law which corresponds to the pressure change in a piston engine. The volume variation versus time is given by:

$$v(\phi) = V_0 + S[0.5\,\mathrm{s}(1 - \cos\phi) + l + (l^2 - (0.5\,\mathrm{s})^2 \sin^2\phi)^{1/2}] \quad (8)$$

where the equivalent Crank Angle (CA) is ϕ, V_0 represents the initial volume, s is the stroke and l is the connecting rod length. The values used for these parameters are summarized in Table 3. The mixture ignites after an autoignition time

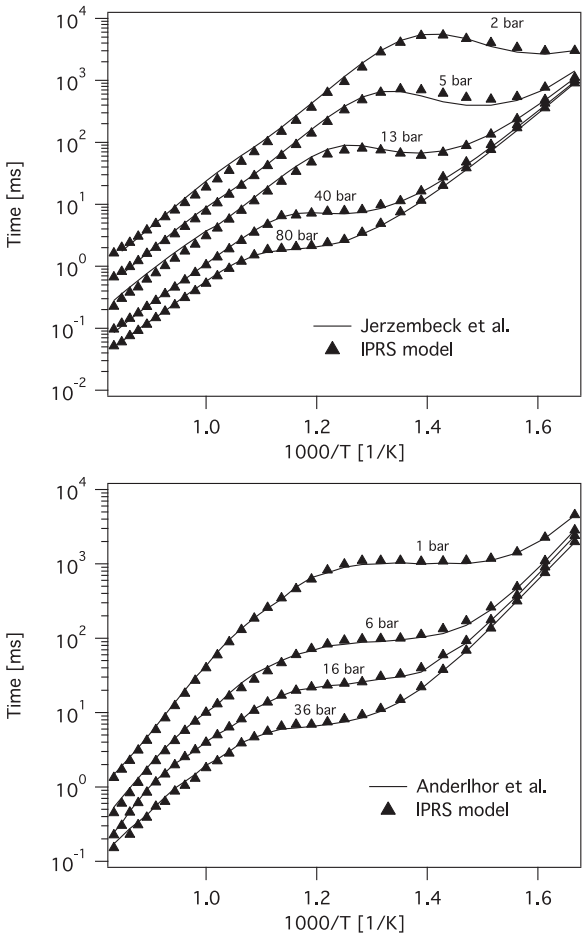

Fig. 9. Comparison of AI delays obtained with the IPSR model and the Cantera software for isooctane (top) and gasoline surrogate (bottom).

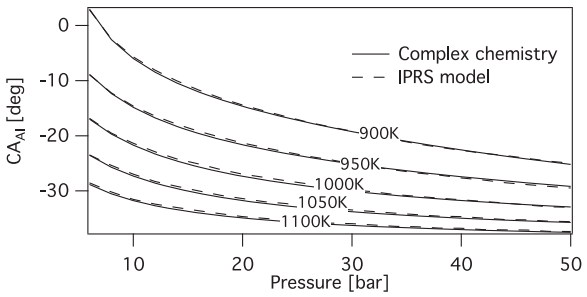

Fig. 10. AI delay in a stoichiometric gasoline/air compressed cylinder obtained with the IPRS model compared to the complex chemistry of [22] computed with Cantera.

τ_{AI} (or a crank angle CA_{AI}). The autoignition crank angle CA_{AI} is plotted as a function of the initial pressure for different temperatures in Fig. 10. For the wide range of initial conditions evaluated here, the IPRS model gives exactly the same results as the complex chemistry validating the ability of the IPRS model to accurately predict AI delays in conditions favorable to abnormal combustions.

5. Validation in a one dimensional flow: transition to detonation

The previous section showed that IPRS can capture autoignition in homogeneous flows. When the flow is not homogeneous, autoignition can lead to complex flame structures and the IPRS model should be able to capture them. A representative test for such cases is autoignition in a one-dimensional mixture, close to autoignition conditions, where the temperature is stratified [24,25]. Here we consider a hot spot zone of size r_0 where the temperature changes with an initial gradient $\frac{\partial T}{\partial x}$ (Fig. 11). In these situations, different modes of reaction can occur. The diagram proposed by Bradley and Kalghatgi [24] (Fig. 12) classifies theses modes depending on the dimensionless temperature gradient ξ (Eq. (9)) and hot spot size ϵ (Eq. (10)).

$$\xi = \left(\frac{\partial T}{\partial x}\right)\left(\frac{\partial T}{\partial x}\right)_c^{-1} \tag{9}$$

$$\epsilon = \frac{r_0}{a\tau_e} \tag{10}$$

In these expressions $\left(\frac{\partial T}{\partial x}\right)_c = \frac{1}{a}\frac{\partial T}{\partial \tau_{AI}}$ is the critical gradient, a is the speed of sound and τ_e the chemical excitation time defined as the time needed to go from 5% to 100% of the maximum heat release

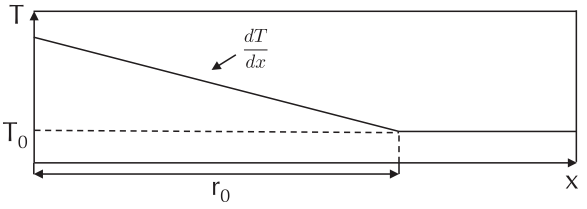

Fig. 11. Initial conditions for the non-homogeneous test case: one-dimensional hot spot.

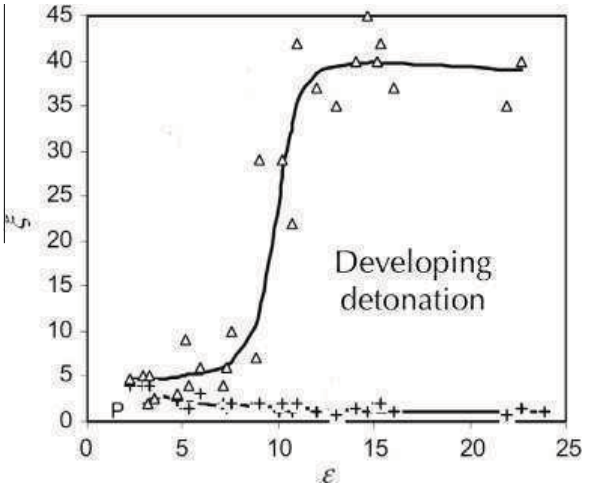

Fig. 12. Modes of reaction after hot spot autoignition as proposed by Bradley and Kalghatgi [24].

Please cite this article in press as: A. Misdariis et al., *Proc. Combust. Inst.* (2014), http://dx.doi.org/10.1016/j.proci.2014.06.053

in a PSR [24]. One can identify four zones from this diagram: (i) if the temperature gradient is large compared to the autoignition delay gradient a subsonic autoignitive front will propagate inside the fresh gas; (ii) if this gradient is very small a thermal explosion will occur as this configuration tends towards PSR configurations. In other regions of the diagram the autoignition front can develop into a detonation wave (iv) or not (iii). To permit a transition to detonation the hot spot must be of a critical size ensuring that the residence time of the pressure wave generated by autoignition inside the hot spot is large enough compared to the chemical time feeding it (in practice several chemical times are needed). All these configurations were computed with the IPRS model: only configurations (iii) and (iv) are discussed here as (i) and (ii) are similar to the test cases shown in Sections 3.1 and 3.2.

The initial conditions consist of a 1D domain filled with a homogeneous stoichiometric isooctane/air mixture at 50 bar and a temperature of 1100 K outside of the hot spot. For (iii) the size of the hot spot is 4 mm with a linear gradient of 5 K/mm. This case corresponds to $\xi = 16$ and $\epsilon = 7$. A weak pressure wave is generated by the hot spot autoignition (Fig. 13) which is amplified up to 200 bar just before exiting the hot spot at $x = 4$ mm due to a coupling with the reaction front. At this point the autoignition/pressure wave speed reaches 1600 m/s meaning that the transition to detonation is close. Outside the hot spot, the pressure wave and the autoignition wave velocities start diverging: the transition to detonation aborts and the peak pressure wave is reduced since it is not sustained by autoignition anymore. The same configuration is then simulated with a larger hot spot size of 10 mm with a temperature gradient

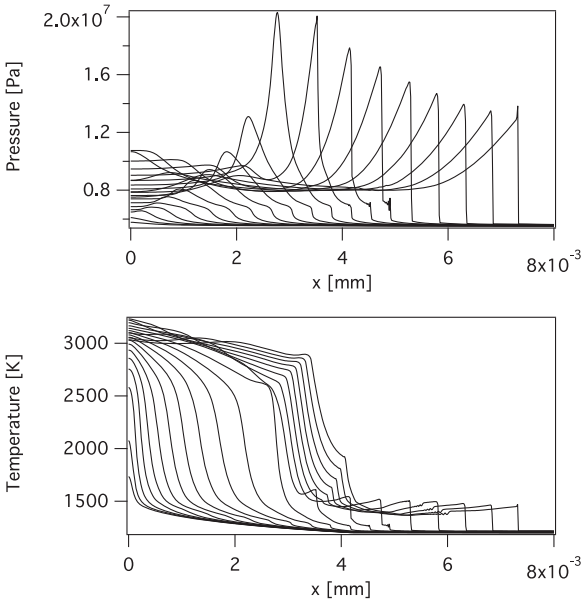

Fig. 13. Hot spot autoignition and failure to sustain a detonation outside the hot spot.

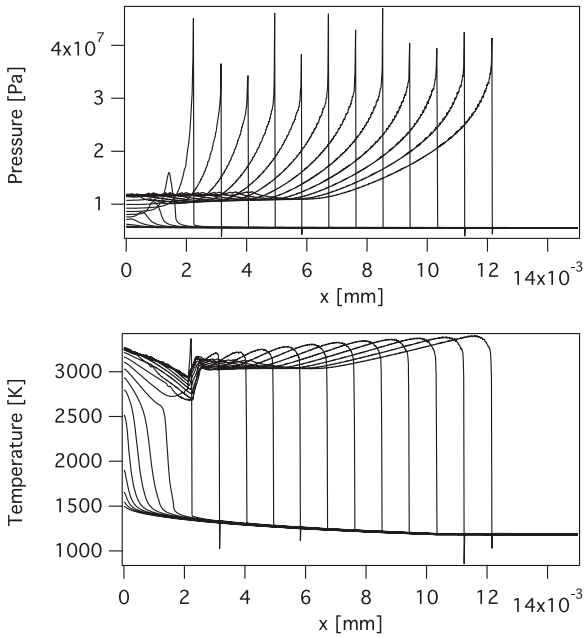

Fig. 14. Hot spot autoignition and transition to detonation outside the hot spot.

of 4 K/mm which corresponds to $\xi = 9$ and $\epsilon = 25$. Figure 14 shows that after autoignition, the pressure wave and the reaction front couple inside the hot spot as in the previous configuration. However, the bigger hot spot radius enables a full coupling between the two waves which eventually propagate together at about 2000 m/s: the pressure/autoignition waves remain coupled outside the hot spot and the strong pressure peak is not dissipated. This simple configuration illustrates the accuracy of the IPRS model: in addition to the prediction of autoignition delays it is able to accurately predict the different modes of propagation after autoignition and to reproduce the coupling between acoustics and chemical reactions when the ambient conditions promote a deflagration to detonation transition.

6. Conclusion

A model called IPRS was introduced to predict abnormal combustions in IC engines in the context of LES. This model uses a single reduced chemical scheme (with two reactions) to describe both autoignition (AI) and propagation. This is obtained by using a different pre-exponential constant of the fuel decomposition Arrhenius law at low and high temperatures. The low temperature value of the constant used for AI does not impact the flame propagation since the main part of the heat release occurs at high temperatures: the constant can be tuned at low temperatures to correctly capture the AI process and be changed at high temperatures to predict propagation. The IPRS model has been successfully applied to several laminar configurations (autoiginition and

Please cite this article in press as: A. Misdariis et al., *Proc. Combust. Inst.* (2014), http://dx.doi.org/10.1016/j.proci.2014.06.053

premixed flames) and to configurations close to IC engines. Its application to one-dimensional single hot spot cases also permits to highlight the different modes of reaction after autoignition and the conclusions of [24,25] were retrieved.

Acknowledgments

The authors gratefully acknowledge IFPEn for fruitful discussions. This work was granted access to the HPC resources of CCRT under allocations 2012–026074 made by GENCI (Grand Equipement National de Calcul Intensif). The authors acknowledge the financial support by the French ANR under grant ANR-10-VPTT-0002 ICAMDAC.

References

[1] V. Granet, O. Vermorel, C. Lacour, B. Enaux, V. Dugué, T. Poinsot, *Combust. Flame* 159 (4) (2012) 1562–1575.
[2] B. Enaux, V. Granet, O. Vermorel, et al., *Proc. Combust. Inst.* 33 (2011) 3115–3122.
[3] O. Vermorel, S. Richard, O. Colin, C. Angelberger, A. Benkenida, D. Veynante, *Combust. Flame* 156 (8) (2009) 1525–1541.
[4] D.F. Davidson, M.A. Oehlschlaeger, J.T. Herbon, R.K. Hanson, *Proc. Combust. Inst.* 29 (2002) 1295–1301.
[5] X. He, M.T. Donovan, B.T. Zigler, et al., *Combust. Flame* 142 (3) (2005) 266–275.
[6] D.C. Horning, D.F. Davidson, R.K. Hanson, *J. Prop. Power* 18 (2) (2002) 363–371.
[7] C.K. Westbrook, W.J. Pitz, O. Herbinet, H.J. Curran, E.J. Silke, *Combust. Flame* 156 (1) (2009) 181–199.
[8] O. Colin, A. Piresda Cruz, S. Jay, *Proc. Combust. Inst.* 30 (2) (2005) 2649–2656.
[9] N. Peters, B. Kerschgens, G. Paczko, SAE Paper (2013-01-1109), 2012.
[10] M.P. Halstead, L.J. Kirsch, C.P. Quinn, *Combust. Flame* (1977) 45–60.
[11] E.M. Sazhina, S.S. Sazhin, M.R. Heikal, C.J. Marooney, *Fuel* 78 (4) (1999) 389–401.
[12] C. Pera, V. Knop, *Fuel* 96 (0) (2012) 59–69.
[13] P. Schmitt, T. Poinsot, B. Schuermans, K.P. Geigle, *J. Fluid Mech.* 570 (2007) 17–46.
[14] B. Franzelli, E. Riber, M. Sanjosé, T. Poinsot, *Combust. Flame* 157 (7) (2010) 1364–1373.
[15] C. Hasse, M. Bollig, N. Peters, H.A. Dwyer, *Combust. Flame* 122 (1-2) (2000) 117–129.
[16] P. Quillatre, O. Vermorel, T. Poinsot, P. Ricoux, *Ind. Eng. Chem. Res.* 52 (33) (2013) 11414–11423.
[17] A. Sánchez, A. Lépinette, M. Bollig, A. Linán, B. Lázaro, *Combust. Flame* 123 (2000) 436–464.
[18] E. Fernandez-Tarrazo, A. Sanchez, A. Linan, F.A. Williams, *Combust. Flame* 147 (1-2) (2006) 32–38.
[19] B. Franzelli, E. Riber, L.Y. Gicquel, T. Poinsot, *Combust. Flame* 159 (2) (2012) 621–637.
[20] D.G. Goodwin, Cantera, 2009.
[21] S. Jerzembeck, N. Peters, P. Pepiot-Desjardins, H. Pitsch, *Combust. Flame* 156 (2) (2009) 292–301.
[22] J.M. Anderlohr, R. Bounaceur, A. Pires DaCruz, F. Battin-Leclerc, *Combust. Flame* 156 (2) (2009) 505–521.
[23] T. Poinsot, D. Veynante, *Theoret. Numer. Combust.* (2011).
[24] D. Bradley, G.T. Kalghatgi, *Combust. Flame* 156 (12) (2009) 2307–2318.
[25] X.J. Gu, D.R. Emerson, D. Bradley, *Combst. Flame* 133 (1–2) (2003) 63–74.

APPENDIX C

Injection supercritique dans les moteurs automobiles

C.1 Introduction

Pendant cette thèse, un échange de trois mois a été fait avec le laboratoire Sandia (Livermore, CA) pour étudier le processus d'injection dans les moteurs diesel. Durant ces trois mois et en collaboration avec l'équipe de J.Oefelein, la configuration Spray-A (Pickett *et al.*, 2010) de l'ECN (Engine Combustion Network) a été simulée à l'aide du code LES Raptor (Oefelein, 2005, 2006). Cette configuration a été créée pour reproduire l'injection dans les moteurs diesel. La simulation réalisée a permis d'étudier le processus de mélange à la sortie de l'injecteur et de déterminer les régions les plus propices à l'auto-allumage. Ce travail a donné lieu à deux publications proposées dans cette annexe: la première a été publiée dans la revue *SAE International* et la seconde a été présentée au 35^{th} Symposium (Int.) on combustion (San Francisco 2014).

C.2 Article publié dans *SAE International*

2014-01-1429
Published 04/01/2014

doi:10.4271/2014-01-1429
saeeng.saejournals.org

Effects of Real-Fluid Thermodynamics on High-Pressure Fuel Injection Processes

Joseph Oefelein, Guilhem Lacaze, Rainer Dahms, and Anthony Ruiz
Sandia National Laboratories

Antony Misdariis
Renault SAS

ABSTRACT

This paper first summarizes a new theoretical description that quantifies the effects of real-fluid thermodynamics on liquid fuel injection processes as a function of pressure at typical engine operating conditions. It then focuses on the implications this has on modeling such flows with emphasis on application of the Large Eddy Simulation (LES) technique. The theory explains and quantifies the major differences that occur in the jet dynamics compared to that described by classical spray theory in a manner consistent with experimental observations. In particular, the classical view of spray atomization as an appropriate model at some engine operating conditions is questionable. Instead, non-ideal real-fluid behavior must be taken into account using a multicomponent formulation that applies to hydrocarbon mixtures at high-pressure supercritical conditions. To highlight the implications and needs related to modeling, we present a series of studies using LES that focus on experiments being conducted in the high-pressure combustion vessel at Sandia National Laboratories. We extend LES studies performed previously to the Engine Combustion Network (www.sandia.gov/ECN) Spray-H and Spray-A injectors using n-heptane and n-dodecane as the respective fuels. The accompanying analysis reveals the structural characteristics associated with the inherent scalar mixing processes at conditions directly relevant to advanced Diesel engines.

CITATION: Oefelein, J., Lacaze, G., Dahms, R., Ruiz, A. et al., "Effects of Real-Fluid Thermodynamics on High-Pressure Fuel Injection Processes," *SAE Int. J. Engines* 7(3):2014, doi:10.4271/2014-01-1429.

INTRODUCTION

Multiphase combustion processes are prevalent in a wide variety of advanced combustion systems; e.g., internal combustion engines and gas turbines for propulsion and power. Treating these processes involves a variety of challenges that include all of the complications associated with turbulent combustion in gas phase systems, plus significant additional complications that arise due to the presence of multiple phases. Multi-scale coupling between processes occurs over a wide range of time and length scales, many being smaller than can be resolved in a numerically feasible manner. Further complications arise when liquid phases are present due to the introduction of dynamically evolving interface boundaries and the complex exchange processes that occur as a consequence. At the device level, high-performance, dynamic stability, low pollutant emissions, and low soot formation must be achieved simultaneously in complex geometries that generate complex flow and acoustic patterns. Flow and combustion processes are highly turbulent; i.e., integral-scale Reynolds numbers of $O(10^5)$ or greater, and the turbulence dynamics are inherently dominated by geometry or various operating transients. In modern systems, operating pressures now approach or exceed the thermodynamic critical pressures of the working fluids. Operation at elevated pressures introduces significant thermodynamic non-idealities and transport anomalies in low-temperature regions. Elevated pressures also significantly increase the system Reynolds number(s), which inherently broadens the range of spatial and temporal scales that interactions occur over.

Research over the past decade has provided significant insights into the structure and dynamics of multiphase flows at high pressures [1, 2, 3, 4, 5, 6, 7, 8, 9, 10, 11, 12]. There are two extremes that must be considered in modern devices. At subcritical, or certain supercritical operating pressures, the classical situation exists where a well-defined molecular interface separates the injected liquid from ambient gases due to the presence of surface tension. Interactions between dynamic shear forces and surface tension promote primary atomization and secondary breakup processes that evolve from a dense state, where the liquid exists as sheets filaments or lattices intermixed with sparse pockets of gas; to a dilute state, where drop-drop interactions are negligible and dilute spray theory can be used. When operating pressures exceed the critical pressure of the injected liquid, however, the situation can become quite different. Under these conditions, interfacial

diffusion layers can develop as a consequence of vanishing surface tension forces, broadening gas-liquid interfaces, and reduced mean free molecular path. These interfaces eventually enter the continuum length scale regime and disappear as interfacial fluid temperatures rise above the critical temperature of the local mixture. Lack of inter-molecular forces, coupled with broadening interfaces, promote diffusion dominated mixing processes prior to atomization. As a consequence, injected jets evolve in the presence of exceedingly large but continuous thermo-physical gradients in a manner markedly different from classical assumptions.

Recent research has shown that the transitional change described above is controlled by the multicomponent nature of the liquid-gas interface [13, 14]. Detailed analysis of the interfacial structure shows how it disintegrates as a function of pressure, temperature, and the local multicomponent mixture properties. A key output are regime diagrams for liquid injection such as the example shown in Fig. 1. This figure shows results for n-dodecane injected at a temperature of 363 *K* into gaseous nitrogen at varying ambient pressures and temperatures relevant to Diesel engine operation. The classical spray regime (highlighted in white) and diffusion-dominated mixing regime (gray) are found using the Knudsen number (i.e., molecular-mean-free-path divided by the interfacial-thickness) criterion explained in Reference [14]. To illustrate the relevance of this diagram, ambient gas pressure-temperature lines, which span a range of conditions during different Diesel engine compression cycles, are shown for three representative initial conditions; a) turbo-charged (2.5 *bar*, 363 *K*), b) medium-load (1.6 *bar*, 343 *K*), and c) light-load (1 *bar*, 335 *K*) operation. Fuel injection occurs at full compression conditions, as indicated by the three respective points in the diagram. Interestingly, the cylinder pressures at full compression exceed the supercritical mixture pressure for all of the cases considered. Only at light-load operation does there appear to be a chance that classical fuel spray atomization takes place. Thus, contrary to conventional wisdom, the theory indicates that classical spray phenomena does not occur at the particular set of Diesel injection conditions considered here. Instead, the injected fuel jet exhibits diminished interfacial structure and surface tension, which leads to diffusion-dominated mixing. Predictions have been corroborated using microscopic imaging to visualize the features of dense-fluid jets (top right image in Fig. 1) and classical spray atomization (bottom right image).

Applying the analysis to a variety of system specific operating conditions suggests that almost all modern high-performance combustion devices operate over ranges of pressures and temperatures in the vicinity of, or across, the transitional regime. Figure 2 shows the typical operating envelopes associated with advanced Diesel, gas turbine, and gasoline direct-injection systems using n-dodecane, n-decane, and iso-octane as respective fuel surrogates. The diagram is constructed for liquid injection temperatures from 300 to 363 *K* in a general manner by normalizing the ambient gas pressure and temperature by the corresponding critical properties of the liquid phase. The Classical Spray Regime is highlighted in green, the Supercritical Fluid Regime is highlighted in blue, and the Transitional Regime is highlighted in red. Respective operating envelopes are then indicated by the oval white areas. In each case the operational envelope crosses into the transitional regime, which exemplifies the need to understand both classical spray and supercritical fluid phenomena simultaneously over relevant ranges of conditions.

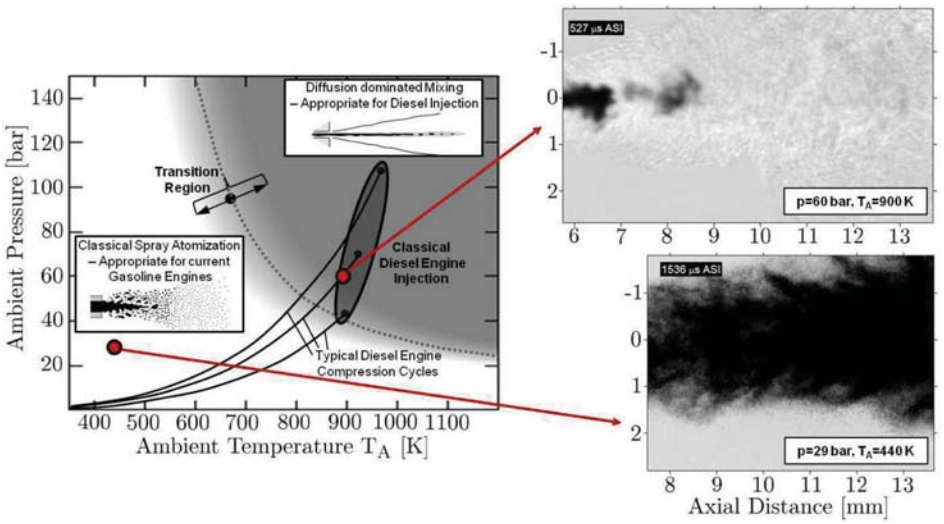

Figure 1. The regime diagram (left) describes conditions where n-dodecane injected at a temperature of 363 *K* into nitrogen transitions to a dense supercritical jet without drop formation. Corresponding high-speed imaging of a dense supercritical jet (top right) and spray (bottom right) illustrates the significant change induced as a function of different ambient pressures and temperatures [13, 14] (Images on right courtesy of L. M. Pickett, Sandia National Laboratories).

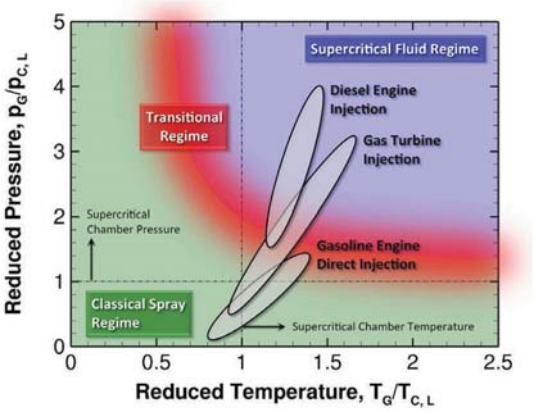

Figure 2. Typical operating envelopes associated with advanced Diesel, gas turbine, and gasoline direct-injection systems using n-dodecane, n-decane, and iso-octane as respective fuel surrogates. The diagram is constructed for liquid injection temperatures from 300 to 363 *K*. The ambient gas pressure and temperature are normalized by the corresponding critical properties of respective liquid phases.

APPROACH

To enhance our understanding of the processes described above in the context of Diesel engines, we have combined the new theoretical findings and high-fidelity Large Eddy Simulation (LES) to gain a more detailed view into direct-injection processes at high-pressures. We use the experimental data provided by Pickett *et al.* as part of the Engine Combustion Network cases (i.e., the ECN workshop, see www.ca.sandia.gov/ECN [15]) as key targets. The analysis is performed using a single unified code framework called RAPTOR. Unlike conventional LES codes, RAPTOR is a DNS solver that has been optimized to meet the strict algorithmic requirements imposed by the LES formalism. The theoretical framework solves the fully-coupled conservation equations of mass, momentum, total-energy, and species for a chemically reacting flow. It is designed to handle high Reynolds number, high-pressure, real-gas and/or liquid conditions over a wide Mach operating range. It also accounts for detailed thermodynamics and transport processes at the molecular level, and is sophisticated in its ability to handle a generalized model framework in both the Eulerian and Lagrangian frames. A noteworthy aspect of RAPTOR is it was designed specifically for LES using non-dissipative, discretely conservative, staggered, finite-volume differencing. This eliminates numerical contamination of the subgrid-scale models due to artificial dissipation and provides discrete conservation of mass, momentum, energy, and species, which is an imperative requirement for high quality LES. Details related to the baseline formulation and subgrid-scale models are given by Oefelein [16]. Representative case studies are given by Oefelein *et al.* [6, 17, 18, 19, 20, 21, 22, 23, 24].

The baseline system of equations are cast in dimensionless form using a reference length-scale δ_{ref}, flow speed U_{ref}, and fluid state characterized by a reference density ρ_{ref}, sound speed c_{ref}, constant pressure specific heat C_{pref}, and dynamic viscosity μ_{ref}. Using these quantities, a reference Mach and Reynolds number are defined as $M = U_{ref}/c_{ref}$ and $Re = \rho_{ref}U_{ref}\delta_{ref}/\mu_{ref}$. With these definitions, the instantaneous conservation equations of mass, momentum, total-energy and chemical species can be written in conservative form as follows:

- Mass:

$$\frac{\partial \rho}{\partial t} + \nabla \cdot (\rho \mathbf{u}) = 0. \tag{1}$$

- Momentum:

$$\frac{\partial}{\partial t}(\rho \mathbf{u}) + \nabla \cdot \left[\rho \mathbf{u} \otimes \mathbf{u} + \frac{p}{M^2}\mathbf{I}\right] = \nabla \cdot \tau, \tag{2}$$

where

$$\tau = \frac{\mu}{Re}\left[-\frac{2}{3}(\nabla \cdot \mathbf{u})\mathbf{I} + \left(\nabla \mathbf{u} + \nabla \mathbf{u}^T\right)\right]$$

represents the viscous stress tensor.

- Total Energy:

$$\frac{\partial}{\partial t}(\rho e_t) + \nabla \cdot [(\rho e_t + p)\mathbf{u}] = \nabla \cdot \left[\mathbf{q}_e + M^2(\tau \cdot \mathbf{u})\right], \tag{3}$$

where

$$\begin{aligned} e_t &= e + \frac{M^2}{2}\mathbf{u} \cdot \mathbf{u} \\ e &= \sum_{i=1}^{N} h_i Y_i - \frac{p}{\rho} \\ h_i &= h_{f_i}^{\circ} + \int_{p^{\circ}}^{p}\int_{T^{\circ}}^{T} C_{p_i}(T,p)dTdp \end{aligned}$$

represents the total internal energy, internal energy and enthalpy of the i^{th} species, respectively, and $\mathbf{q}_e$ represents the energy diffusion flux.

- Species:

$$\frac{\partial}{\partial t}(\rho Y_i) + \nabla \cdot (\rho Y_i \mathbf{u}) = \nabla \cdot \mathbf{q}_i + \dot{\omega}_i \qquad i = 1, \ldots, N-1, \tag{4}$$

where $\mathbf{q}_i$ and $\dot{\omega}_i$ represent the mass diffusion fluxes and the rate of production of the i^{th} species, respectively.

Equations (1), (2), (3), (4), coupled with 1) an appropriate equation of state, 2) appropriate treatments of thermodynamic and transport properties, and 3) validated mixing and combining rules for the mixtures of interest accommodate the most general system of interest including cases when multicomponent and/or preferential diffusion processes are present. The viscous stress tensor is assumed to follow Stokes' hypothesis, and the heat release due to chemical reaction in

Eq. (3) is accounted for in the description of the specific enthalpies, h_i, as given by the enthalpy of formation, h°_{fi}. The heat release rate can be represented equivalently, as a source term on the right hand side of Eq. (3), as the product of the enthalpy of formation and the local rate of production of all the species considered in the system. Using this representation, the source term and specific enthalpies are be defined as

$$\dot{Q}_e = -\sum_{i=1}^{N} \dot{\omega}_i h^\circ_{fi}, \text{ and} \tag{5}$$

$$h_i = \int_{p^\circ}^{p} \int_{T^\circ}^{T} C_{p_i}(T,p)\,dT\,dp. \tag{6}$$

For LES applications, the filtered version of Eqs. (1), (2), (3), (4) are solved. These equations are given respectively as:

$$\frac{\partial \overline{\rho}}{\partial t} + \nabla \cdot (\overline{\rho}\tilde{\mathbf{u}}) = 0, \tag{7}$$

$$\frac{\partial}{\partial t}(\overline{\rho}\tilde{\mathbf{u}}) + \nabla \cdot \left[\left(\overline{\rho}\tilde{\mathbf{u}} \otimes \tilde{\mathbf{u}} + \frac{\mathcal{P}}{M^2}\mathbf{I}\right)\right] = \nabla \cdot \vec{\mathcal{T}}, \tag{8}$$

$$\frac{\partial}{\partial t}(\overline{\rho}\tilde{e}_t) + \nabla \cdot [(\overline{\rho}\tilde{e}_t + \mathcal{P})\tilde{\mathbf{u}}] = \nabla \cdot \left[\left(\vec{\mathcal{Q}}_e + M^2(\vec{\mathcal{T}} \cdot \tilde{\mathbf{u}})\right)\right] + \overline{\dot{Q}}_e, \tag{9}$$

$$\frac{\partial}{\partial t}(\overline{\rho}\tilde{Y}_i) + \nabla \cdot (\overline{\rho}\tilde{Y}_i\tilde{\mathbf{u}}) = \nabla \cdot \vec{\mathcal{S}}_i + \overline{\dot{\omega}}_i. \tag{10}$$

The terms P, $\vec{\mathcal{T}}$, $\vec{\mathcal{Q}}_e$ and $\vec{\mathcal{S}}_i$ represent respective composite (i.e., molecular plus subgrid-scale) stresses and fluxes. Quantities $\overline{\dot{Q}}_e$ and $\overline{\dot{\omega}}_i$ represent the filtered energy and species source terms, respectively.

The subgrid-scale closure is obtained using the “mixed” dynamic Smagorinsky model by combining the models proposed by Erlebacher, Hussaini, Speziale and Zang [25], and Speziale [26] with the dynamic modeling procedure [27, 28, 29, 30, 31]. The composite stresses and fluxes in Eqs. (7), (8), (9), (10) are then given as

$$\vec{\mathcal{T}} = (\mu_t + \mu)\frac{1}{Re}\left[-\frac{2}{3}(\nabla \cdot \tilde{\mathbf{u}})\mathbf{I} + \left(\nabla\tilde{\mathbf{u}} + \nabla\tilde{\mathbf{u}}^T\right)\right] - \overline{\rho}\left(\widetilde{\tilde{\mathbf{u}} \otimes \tilde{\mathbf{u}}} - \tilde{\tilde{\mathbf{u}}} \otimes \tilde{\tilde{\mathbf{u}}}\right), \tag{11}$$

$$\vec{\mathcal{Q}}_e = \left(\frac{\mu_t}{Pr_t} + \frac{\mu}{Pr}\right)\frac{1}{Re}\nabla\tilde{h} + \sum_{i=1}^{N}\tilde{h}_i\vec{\mathcal{S}}_i - \overline{\rho}\left(\widetilde{\tilde{h}\tilde{\mathbf{u}}} - \tilde{\tilde{h}}\tilde{\tilde{\mathbf{u}}}\right), \text{ and} \tag{12}$$

$$\vec{\mathcal{S}}_i = \left(\frac{\mu_t}{Sc_{t_i}} + \frac{\mu}{Sc_i}\right)\frac{1}{Re}\nabla\tilde{Y}_i - \overline{\rho}\left(\widetilde{\tilde{Y}_i\tilde{\mathbf{u}}} - \tilde{\tilde{Y}}_i\tilde{\tilde{\mathbf{u}}}\right). \tag{13}$$

The term μ_t represents the subgrid-scale eddy viscosity, given by

$$\mu_t = \overline{\rho}C_R\Delta^2\Pi_{\tilde{\mathbf{S}}}^{\frac{1}{2}}, \tag{14}$$

where

$$\Pi_{\tilde{\mathbf{S}}} = \tilde{\mathbf{S}} : \tilde{\mathbf{S}}, \text{ and } \tilde{\mathbf{S}} = \frac{1}{2}\left(\nabla\tilde{\mathbf{u}} + \nabla\tilde{\mathbf{u}}^T\right). \tag{15}$$

The terms C_R, Pr_t, and Sc_{ti} represent the Smagorinsky, subgrid-scale Prandtl and subgrid-scale Schmidt numbers and are evaluated dynamically as functions of space and time. The overall model includes the Leonard and cross-term stresses and provides a Favre averaged generalization of the Smagorinsky eddy viscosity model [32] coupled with gradient diffusion models to account for subgrid-scale mass and energy transport processes.

The property evaluation scheme is designed to account for thermodynamic non-idealities and transport anomalies over a wide range of pressures and temperatures. The scheme is comprehensive and intricate, thus only a skeletal description can be given here. The extended corresponding states model [33, 34] is employed with a cubic equation of state. In past studies, both the Benedict-Webb-Rubin (BWR) equation of state and cubic equations of state have been used to evaluate the pressure-volume-temperature (PVT) behavior of the inherent dense multicomponent mixtures. Use of modified BWR equations of state in conjunction with the extended corresponding states principle has been shown to provide consistently accurate results over the widest range of pressures, temperatures, and mixture states, especially at near-critical conditions. A major disadvantage of BWR equations, however, is that they are not computationally efficient. Cubic equations of state can be less accurate, especially for mixtures at near-critical or saturated conditions, but are computationally efficient. Experience has shown that both the Soave-Redlich-Kwong (SRK) and Peng-Robinson (PR) equations, when used in conjunction with the corresponding states principle, can give accurate results over the range of pressures, temperatures, and mixture states of

interest in this study. The SRK coefficients are fit to vapor pressure data and are thus more suitable for conditions when the reduced temperature is less than one. The PR coefficients, on the other hand, are more suitable for conditions when the reduced temperature is greater than one. Here the PR equation of state was used exclusively. A summary of the cubic equations of state and recommended constants is given by Reid *et al.* [35, Chapter 3]. Having established an analytical representation for real mixture PVT behavior, the thermodynamic properties are obtained in two steps. First, respective component properties are combined at a fixed temperature using the extended corresponding states methodology to obtain the mixture state at a given reference pressure. A pressure correction is then applied using departure functions of the form given by Reid *et al.* [35, Chapter 5]. These functions are exact relations derived using the Maxwell relations (see VanWylen and Sonntag [36, Chapter 10], for example) and make full use of the real mixture PVT path dependencies dictated by the equation of state. Standard state properties are obtained using the databases developed by Gordon and McBride [37] and Kee *et al.* [38]. Chemical potentials and fugacity coefficients are obtained in a manner similar to that outlined above. Molecular transport properties are evaluated in a manner analogous to the thermodynamic properties. Viscosity and thermal conductivity are obtained using the extended corresponding states methodologies developed by Ely and Hanley [39, 40]. The mass diffusion coefficients and thermal diffusion coefficients are obtained using the methodologies outlined by Bird *et al.* [41] and Hirschfelder *et al.* [42] in conjunction with the corresponding states methodology proposed by Takahashi [43].

From an algorithmic perspective, RAPTOR is massively-parallel and has been ported to a wide variety of computer platforms. Parallelization is achieved using a distributed multiblock domain decomposition with generalized connectivity. Distributed-memory message-passing is performed using MPI and the Single-Program-Multiple-Data (SPMD) model. The temporal integration scheme employs an all-Mach-number formulation using dual-time stepping with generalized preconditioning. The approach is fourth-order accurate in time and provides a fully-implicit solution using a fully explicit (highly-scalable) multistage scheme. Preconditioning is applied on an inner pseudo-time loop and coupled to local time-stepping techniques to minimize convective, diffusive, geometric, and source term anomalies (i.e., stiffness) in an optimal manner. The formulation is A-stable, which allows one to set the physical time-step based solely on accuracy considerations. This attribute typically provides a 2 to 3 order of magnitude increase in the allowable integration time-step compared to conventional compressible flow solvers, especially in low Mach number regimes. The spatial scheme is designed using non-dissipative, discretely-conservative, staggered, finite-volume differencing. The discretization is formulated in generalized curvilinear (i.e., body-fitted) coordinates and employs a general R-refinement adaptive mesh (AMR) capability. This allows us to account for the inherent effects of geometry on turbulence over the full range of relevant scales while significantly reducing the total number of grid cells required in the computational domain. The differencing methodology has been specifically designed for LES. In particular, the second-order accurate staggered grid formulation (where we store scalar values at cell centers and velocity components at respective cell faces) fulfills two key accuracy requirements. First, it is spatially non-dissipative, which eliminates numerical contamination of the subgrid-scale models due to artificial dissipation. Second, the stencils provide discrete conservation of mass, momentum, total energy and species, which eliminates the artificial build up of velocity and scalar energy at the high wavenumbers. This is an imperative requirement for LES. The algorithm includes appropriate switches to handle shocks detonations, flame-fronts, and contact discontinuities.

RESULTS AND DISCUSSION

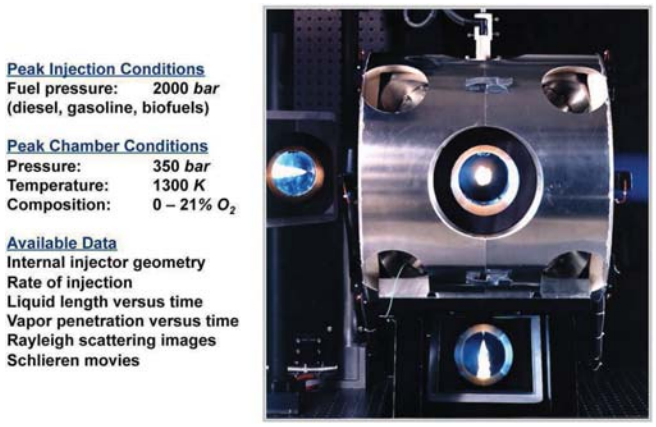

Figure 3. Photograph of the Sandia high-pressure combustion vessel.

Using the real-fluid model framework described above, we have performed a series of studies aimed at understanding the diffusion dominated mixing phenomena described in Figs. 1 and 2. We focus on two key experiments being studied by Pickett *et al.* [15]; namely the “Spray-H (n-heptane)” and “Spray-A (n-dodecane)” cases. Calculations are performed by identically matching the experimental operating conditions, injector geometry, and combustion chamber. The experimental apparatus is shown in Fig. 3. The corresponding computational domain and key operating conditions for the Spray-H case are shown in Fig. 4. The corresponding thermodynamic characteristics of n-heptane are shown in Figs. 5 and 6. Its critical point is 540 *K*, 27.4 *bar*. Thus, n-heptane is injected into the chamber as a compressed liquid (i.e., supercritical with respect to pressure, subcritical with respect to temperature).

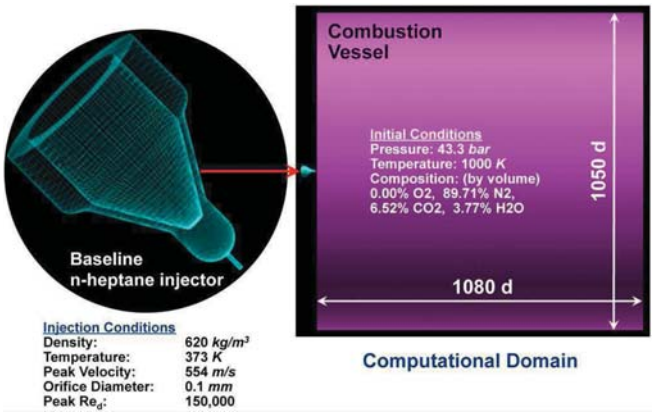

Figure 4. Computational domain and key operating conditions used for LES of the Spray-H case. The injector is mounted at the head-end of the vessel, as indicated by the red arrow.

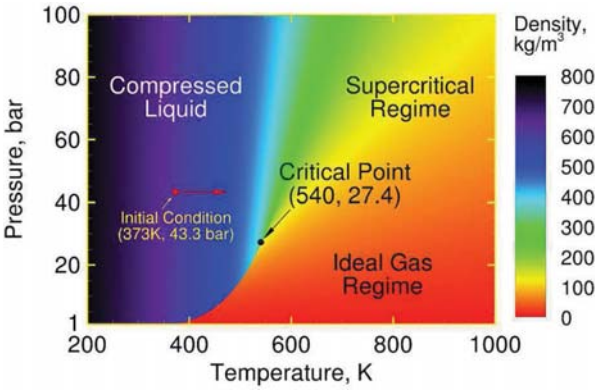

Figure 5. Pressure-temperature diagram of n-heptane showing contours of density, key thermodynamic regimes, and its initial state when injected into the combustion vessel. The n-heptane jet enters as a compressed liquid and is heated at supercritical pressure.

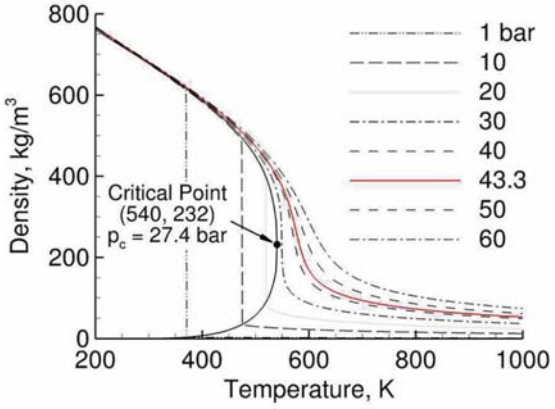

Figure 6. Density of n-heptane as a function of temperature.

The transient jet pulse is modeled to closely approximate the actual experimental conditions. This produces a peak bulk velocity of 554 *m*/*s* and corresponding jet Reynolds number of 150; 000 inside the injector nozzle. The quasi-steady portion of the pulse lasts for 6.66 *ms*. At 6.69 *ms* the jet ramps down to zero velocity, with the end of injection occurring at 6.93 *ms*. An instantaneous snapshot from the LES is shown in Fig. 7. This plot shows a typical instantaneous mixture fraction field. Iso-lines mark the thermodynamic transition of the mixture from a compressed liquid to a supercritical state (black), and the separation between non-ideal and ideal fluid behavior (white).

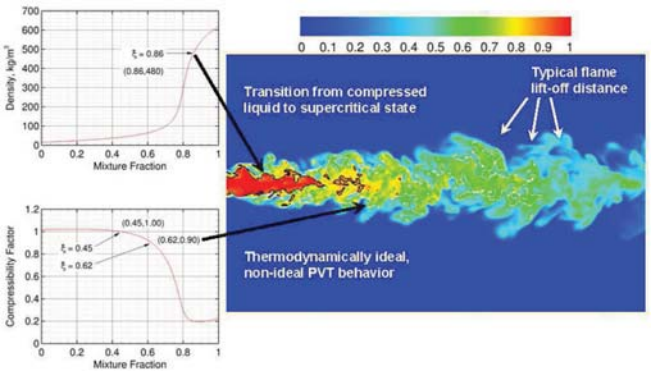

Figure 7. Contour plot showing a representative LES prediction of mixture fraction. Iso-lines mark the transition from a compressed liquid to supercritical state (black) and separation between regions of non-ideal and ideal fluid behavior (white).

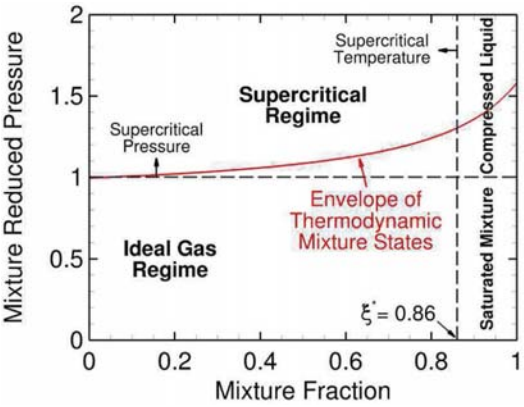

Figure 8. Envelope of mixture states predicted as a function of mixture fraction extracted from LES.

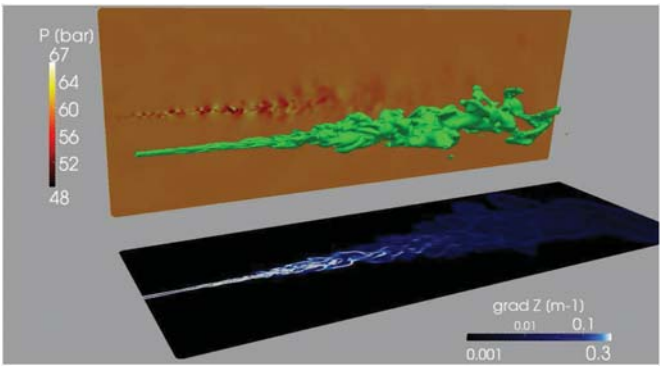

Figure 9. Instantaneous structure of the Spray-A case at 270 μs, which is the point of injection just prior to autoignition. The green iso-contour is the mass fraction of n-dodecane at a value of 0.5. The pressure and scalar dissipation fields along the center plane of the jet are also shown.

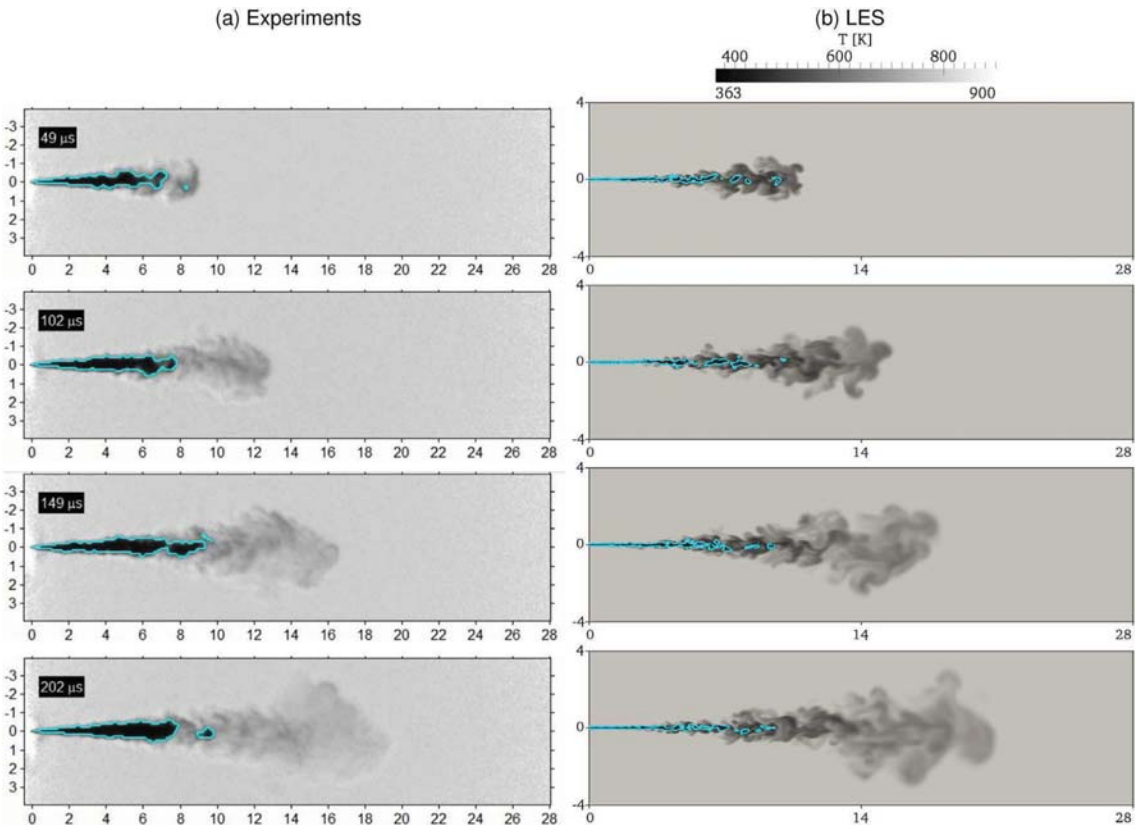

Figure 10. Injection sequence showing (a) shadowgraphs from Pickett *et al.* [44] and (b) corresponding LES fields. Images are obtained using diffused back illumination with a grayscale intensity threshold set to qualitatively indicate the dense liquid region. Based on recommendations from Picket *et al.*, instantaneous shots of the LES temperature field were chosen for comparisons. Space and time graduations are in *mm* and *μs*.

The entire envelope of mixture states associated with this case are shown on a thermodynamic regime diagram in Fig. 8. The mixing path associated with all states throughout the duration of injection never crosses the liquid-vapor regime (i.e., the mixture is never saturated). Instead, n-heptane is injected as a compressed liquid and the interfacial mixing layer dynamics are locally supercritical, which implies that classical first order vapor-liquid phase transitions (as are typically assumed) do not occur. This implies 1) that applying the ideal gas assumption just prior to autoignition in these types of flows is not valid, and 2) the classical view of spray atomization and secondary breakup processes as an appropriate model (as is widely assumed currently) is questionable at these particular conditions. Instead, non-ideal real-fluid behavior associated with the dense liquid jet must be taken into account. Additional details are given by Oefelein *et al.* [22, 23].

Using the same approach as described above, we performed a similar LES calculation of the ECN Spray-A case. Non-reacting liquid n-dodecane at 363 *K* is injected into a quiescent gaseous mixture at 900 *K* and 60 *bar*, which are precisely the same conditions represented by the medium-load compression cycle shown in Fig. 1. The gas mixture in the vessel results from the combustion of acetylene (C_2H_2) and hydrogen (H_2) into air. For the present case, all of the oxygen is consumed before injection and the composition of the gaseous ambient is Y_{O2} = 0, Y_{N2} = 0.897, Y_{CO2} = 0.065, and Y_{H2O} = 0.038. The liquid fuel is injected through a 0.09 *mm* diameter nozzle injector. The peak injection velocity is 620 *m*/*s*, which was selected to provide the same injected mass flow rate as the experiment. A synthetic turbulent signal with a turbulent intensity of 5-percent is superimposed on the bulk profile. The grid spacing in the vicinity of the injector exit is approximately 4 *μm*, with the grid stretched optimally in the downstream and radial directions.

Figure 9 shows the structure of the injected jet at 270 *μs*, which is the point of injection just prior to autoignition. Also shown are the instantaneous pressure and scalar dissipation fields along the center plane of the jet. Similarly, Fig. 10 shows a qualitative comparison of the injection sequence. Results from LES are compared to the shadowgraphs from Pickett *et al.* [44]. The experimental images were obtained using a diffuser back illumination method, with the dense region highlighted using an arbitrary cut-off value in the gray scale. Based on recommendations from Picket *et al.*, instantaneous shots of the LES temperature field were chosen for comparisons. Comparisons between respective images shows qualitatively good agreement between the experiment and LES. Large structures present in the back-illumination images are also observed in the numerical results. The density of the n-dodecane jet is slightly above 700 kg/m^3 at the injector nozzle exit whereas the density of the ambient gas is 23 kg/m^3. The presence of strong density gradients is known to have a stabilization effect on hydrodynamic instabilities, which delays

the destabilization of the jet. Once destabilization occurs, parcels of dense fluid detach from the compressed liquid jet. The dense fragments can still be observed 70 diameters (6.3 *mm*) downstream of the injector exit. The presence of these fast-moving structures enhances local turbulence, which significantly affects mixing.

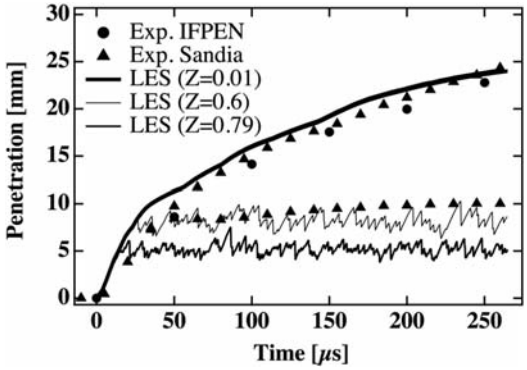

Figure 11. Vapor and liquid penetration trajectories of the jet. The time-resolved liquid core length was determined from high-speed Mie-scatter imaging using a 3-percent threshold of maximum intensity.

The vapor and "liquid" penetration trajectories are shown in Fig. 11. In the LES, vapor penetration is detected by the most upstream point of the iso-surface characterized by a mixture fraction of $Z = 0.01$. The sensitivity of this value has been tested and penetration curves have less than 2-percent variation between $Z = 0.01$ and $Z = 0.1$. LES results are in good agreement with experimental measurements, except at the initial phase of injection ($t < 50$ *μs*). During the initial startup, the simulated vapor penetration is slightly over-predicted. This is possibly an artifact of boundary anomalies associated with the interior sac and nozzle regions of the injector. The time-resolved liquid core length was determined from high-speed Mie-scatter imaging using a 3-percent threshold of maximum intensity, which to some degree is an arbitrary value. Given the current premise that a distinct gas-liquid interface does not exist in this flow, defining the threshold associated with the compressed-liquid core requires additional analysis. Two liquid penetration curves are extracted from the LES to investigate. The first is based on a threshold of $Z = 0.79$, which is the value where the density changes the most with respect to Z (see Fig. 12 b). The second was based on a threshold of $Z = 0.6$, which is simply the value that provides the best match with the experimental data. Both thresholds lead to the same trend as in the experiment. A plateau is observed in the temporal evolution with differing constant values of penetration depending on the mixture fraction value chosen.

Figure 12 provides a global representation of the mixture state just prior to ignition at $t = 260$ *μs*. Scatter plots of (a) temperature, (b) density, (c) compressibility factor, (d) Mach number, and (e) speed of sound are shown as a function of mixture fraction. The adiabatic mixing temperature is also plotted in Fig. 12(a), as shown by the solid blue line. The red line represents the average. The non-linear relation between these quantities and mixture fraction can be largely attributed to real-gas thermodynamics, where large changes in temperature and density occur as a function of relatively small variations in composition. Scatter away from near adiabatic mixing can be attributed to multidimensional transport anomalies. Turbulent stretching and curvature induced by the evolving coherent structures amplifies preferential diffusion effects at both resolved- and subgrid-scales.

Figures 13, 14, 15 show the corresponding mixture fraction, temperature, and density. In Figs. 13 and 14 one can observe the gas-like behavior of the n-dodecane jet. The high-speed compressed liquid jet stays coherent for almost 20 diameters before starting to disintegrate. At approximately 20 diameters downstream, the jet exhibits self-similar behavior, which is a feature of classical gaseous turbulent jets. This trend is correlated with the presence of strong density gradients shown in Fig. 15. Many vortical eddies are generated at the surface of the liquid core, which significantly affects scalar mixing. In the region where the dense core of the jet becomes very corrugated and eventually breaks-up (i.e., at between 20 and 60 diameters), the presence of dense lumps evolving at high speed locally generates significant pressure variations through compression/expansion effects, as can be seen in Fig. 9. These pressure variations modify the flow and enhance mixing.

Figure 12(d) and (e) reveal new and interesting conditions associated with real-fluid thermodynamics coupled with turbulent mixing. The Mach number in the flow varies from low-subsonic levels to approximately Mach 2.5. The speed of sound ($c = \sqrt{\gamma(\partial P/\partial \rho)_{T,Y_i}}$) is seen to vary from approximately 600 *m*/*s* in the ambient gas, to 200 *m*/*s* at a mixture fraction of approximately $Z = 0.79$, to 1000 *m*/*s* in the pure fuel. The affect of this variation on the corresponding instantaneous Mach number and speed of sound distributions is shown in Figs. 16 and 17. Non-linear thermodynamics in the mixing layer of the jet lead to an increase in the ratio of specific heats and a significant decrease of the partial derivative $(\partial P/\partial \rho)_{T,Yi}$, which results in a significant decrease of the sound speed. In the same region, the entrainment caused by the high-speed jet induces flow velocities of approximately 400 *m*/*s*, which is more than two times the local sound speed. These localized regions of supersonic flow have a significant influence on the local pressure field and resultant scalar mixing processes. More research is required in this area to determine the exact consequences of these new observations and how to potentially exploit them.

CONCLUSIONS

Imaging has long shown that under some high-pressure conditions, the presence of discrete two-phase flow processes becomes diminished. Under such conditions, liquid injection processes transition from classical sprays to dense-fluid jets, with no drops present. When and how this transition occurs, however, was not well understood until recently. In this paper, we have summarized a new theoretical description that quantifies the effects of real-fluid thermodynamics on liquid fuel injection processes as a function of pressure at typical Diesel engine operating conditions. We then focused on the implications this has on modeling such flows using the Large Eddy Simulation (LES) technique coupled with real-fluid thermodynamics and transport. The established theory explains and quantifies the major differences that occur in the jet dynamics compared to that described by classical spray theory in a manner consistent with experimental observations. In particular, the classical view of spray atomization as an appropriate model at some engine operating conditions is questionable. Instead, non-ideal real-fluid behavior must be taken into account using a multicomponent formulation that applies to hydrocarbon mixtures at high-pressure supercritical conditions.

To highlight the implications and needs related to modeling, we presented a sequence of studies focused on experiments being conducted in the high-pressure combustion vessel at Sandia National Laboratories. In particular, we extended LES studies performed previously to the Engine Combustion Network (www.sandia.gov/ECN) Spray-H and Spray-A injectors using n-heptane and n-dodecane as the respective fuels. The simulations were performed by identically matching the geometry and operating conditions used in the experiments. Analysis of the results reveals the structural characteristics associated with the inherent scalar mixing processes at conditions relevant to advanced Diesel engines. Trends demonstrate that the mixing path associated with all states throughout the duration of injection (for both Spray-H and Spray-A) never crosses the liquid-vapor regime (i.e., the mixture is never saturated). Instead, the respective fuels are injected as compressed liquids and the interfacial mixing layer dynamics are locally supercritical. This implies 1) that applying the ideal gas assumption just prior to autoignition in these types of flows is not valid, and 2) the classical view of spray atomization and secondary breakup processes as an appropriate model is questionable at these particular conditions. Instead, non-ideal real-fluid behavior associated with the dense liquid jet must be taken into account.

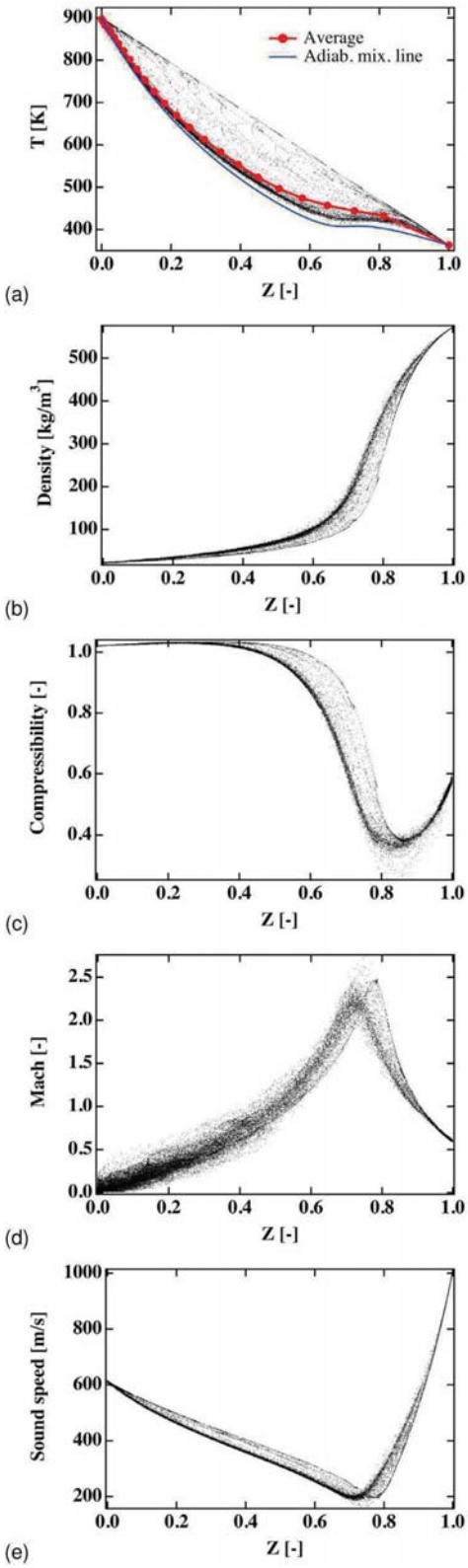

Figure 12. Scatter plots describing the global mixture state just prior to ignition at t = 260 μs.

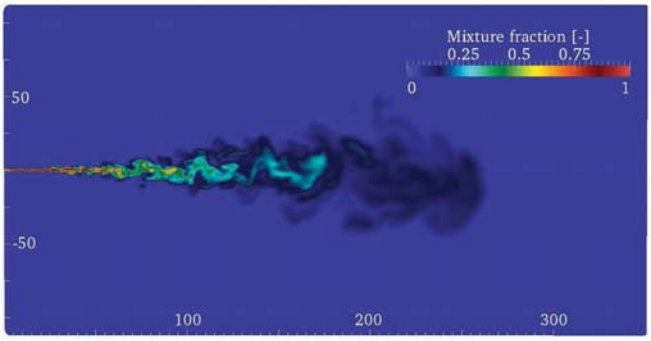

Figure 13. Instantaneous mixture fraction field along the center plane of the jet at 270 μs. Note that the spatial scale is non-dimensionalized using the jet diameter of d_j = 0.09 mm.

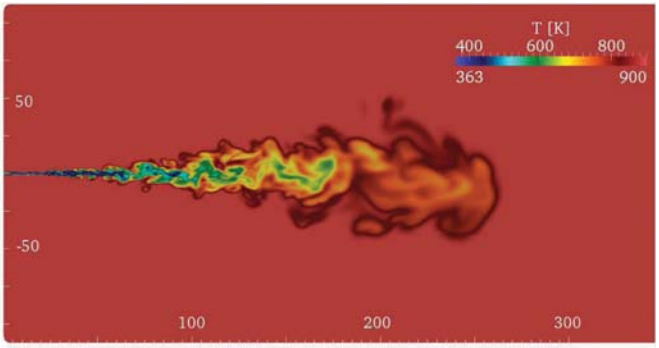

Figure 14. Instantaneous temperature field along the center plane of the jet at 270 μs. Note that the spatial scale is non-dimensionalized using the jet diameter of d_j = 0.09 mm.

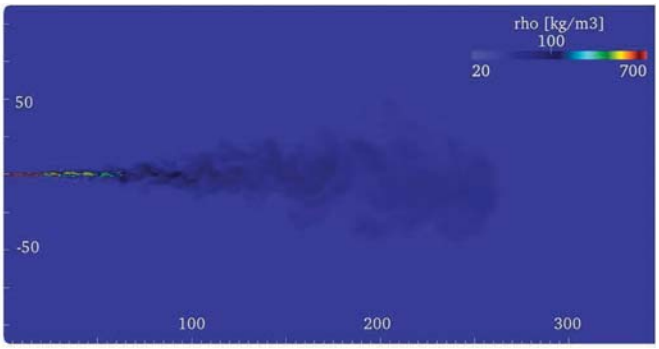

Figure 15. Instantaneous density field along the center plane of the jet at 270 μs. Note that the spatial scale is non-dimensionalized using the jet diameter of d_j = 0.09 mm.

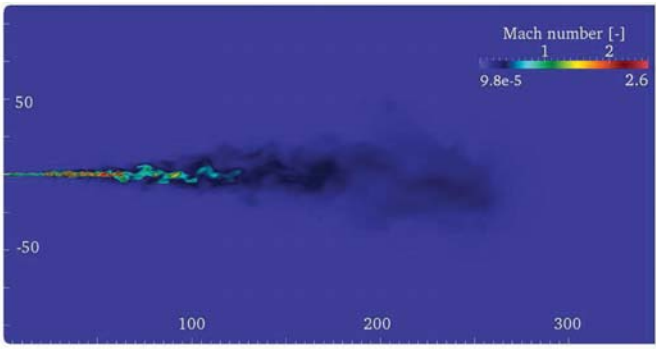

Figure 16. Instantaneous Mach number field along the center plane of the jet at 270 μs. Note that the spatial scale is non-dimensionalized using the jet diameter of d_j = 0.09 mm.

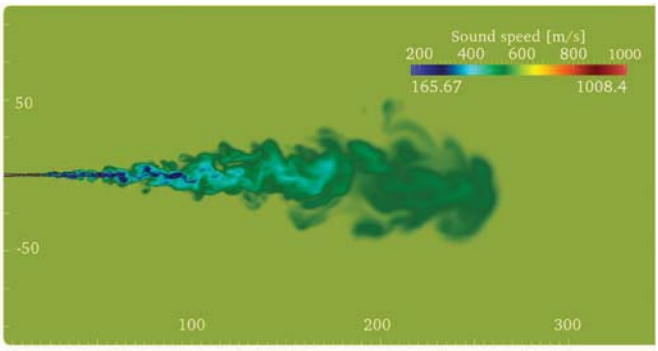

Figure 17. Instantaneous speed of sound distribution along the center plane of the jet at 270 μs. Note that the spatial scale is non-dimensionalized using the jet diameter of d_j = 0.09 mm.

Further analysis of the Spray-A case revealed the instantaneous three-dimensional structure of the injected jet and the instantaneous pressure and scalar dissipation fields along the center plane of the jet. Also shown were the corresponding mixture fraction, temperature, density, Mach number, and speed of sound distributions. The “gas-like” behavior of the fuel jets were observed along with the fact that the high-speed compressed liquid jet remained coherent for almost 20 diameters before starting to disintegrate. At approximately 20 diameters downstream, the jet exhibited self-similar behavior, which is a feature of classical gaseous turbulent jets. Strong density variations resulted from the high-momentum flux ratio, which delayed the destabilization of the jet. Once the destabilization of the dense core occurs, parcels of dense fluid detach from the compressed liquid jet. These dense fragments can still be observed 70 diameters downstream of the injector exit. The presence of these fast-moving dense structures enhances local turbulence as they act as fast-moving solid objects for the surrounding gaseous phase. Many vortical eddies are generated at the surface of the liquid core, and this phenomenon significantly affects the mixing of the fuel. The dense core of the jet becomes very corrugated and eventually breaks-up (at between 20 and 60 diameters), and the presence of dense lumps evolving at high speed locally generates significant pressure variations through compression/expansion effects. These pressure variations modify the flow and enhance mixing.

A last interesting feature of the present cases was how the instantaneous Mach number field varied in the jet. Results demonstrated that the flow is supersonic at various locations within the mixing layer due to variations associated with the speed of sound. In the mixing layer of the jet, non-linear thermodynamic effects lead to a sharp increase in the ratio of specific heats and a significant decrease of the partial derivative $\partial P/\partial \rho$. The combined effect results in a strong decrease of the speed of sound, which reaches a minimum of 170 m/s in the mixing region of the jet between 30 and 70 diameters downstream, compared to 1008 m/s for the pure fuel jet upon injection. In this region, the flow entrained by the high-speed jet has a velocity of approximately 400 m/s, which

is more than two times the local sound speed. More work is required in this area to determine the exact consequences of these new observations.

REFERENCES

1. Oschwald M., Smith J., Branam R., Hussong J., Schik A., Chehroudi B., and Talley D.. Injection of fluids into supercritical environments. *Combustion Science and Technology*, 178(1-3):49-100, 2006.
2. Habiballah M., Orain M., Grisch F., Vingert L., and Gicquel P.. Experimental studies of high-pressure cryogenic flames on the mascotte facility. *Combustion Science and Technology*, 178(1-3):101-128, 2006.
3. Lin K.-C., Cox-Stouffer S., and Jackson T.. Structures and phase transition processes of supercritical methane/ethylene mixtures injected into a subcritical environment. *Combustion Science and Technology*, 178 (1-3):129-160, 2006.
4. Candel S., Juniper M., Singla G., Scouflaire P., and Rolon C.. Structure and dynamics of cryogenic flames at supercritical pressure. *Combustion Science and Technology*, 178(1-3):161-192, 2006.
5. Zong N. and Yang V.. Cryogenic fluid jets and mixing layers in transcritical and supercritcal environments. *Combustion Science and Technology*, 178(1-3):193-228, 2006.
6. Oefelein J. C.. Mixing and combustion of cryogenic oxygen-hydrogen shear-coaxial jet flames at supercritical pressure. *Combustion Science and Technology*, 178(1-3): 229-252, 2006.
7. Bellan J.. Theory, modeling and analysis of turbulent supercritical mixing. *Combustion Science and Technology*, 178(1-3):253-281, 2006.
8. Selle L. C., Okong'o N. A., Bellan J., and Harstad K. G.. Modelling of subgrid-scale phenomena in supercritical transitional mixing layers: An a priori study. *Journal of Fluid Mechanics*, 593:57-91, 2007.
9. Ribert G., Zong N., Yang V., Pons L., Darabiha N., and Candel S.. Counterflow diffusion flames of general fluids: Oxygen/hydrogen mixtures. *Combustion and Flame*, 154: 319-330, 2008.
10. Lacaze G., Cuenot B., Poinsot T., and Oschwald M.. Large eddy simulation of laser ignition and compressible reacting flow in a rocket-like configuration. *Combustion and Flame*, 156:1166-1180, 2009.
11. Pons L., Darabiha N., Candel S., Ribert G., and Yang V.. Mass transfer and combustion in transcritical non-premixed counterflows. *Combustion Theory and Modelling*, 13:57-81, 2009.
12. Schmitt T., Méry Y., Boileau M., and Candel S.. Large-eddy simulation of oxygen/methane flames under transcritical conditions. *Proceedings of the Combustion Institute*, 33:1383-1390, 2011.
13. Dahms R. N., Manin J., Pickett L. M., and Oefelein J. C.. Understanding high-pressure gas-liquid interface phenomena in diesel engines. *Proceedings of the Combustion Institute*, 34:1667-1675, 2013. doi:10.1016/j.proci.2012.06.169.
14. Dahms R. N. and Oefelein J. C.. On the transition between two-phase and single-phase interface dynamics in multicomponent fluids at supercritical pressures. *Physics of Fluids*, 25(092103):1-24, 2013. doi:10.1063/1.4820346.
15. Pickett L. M.. Engine combustion network. www.sandia.gov/ECN, 2005-2014. Sandia National Laboratories, Combustion Research Facility, Livermore, California.
16. Oefelein J. C.. Large eddy simulation of turbulent combustion processes in propulsion and power systems. *Progress in Aerospace Sciences*, 42(1):2-37, 2006.
17. Oefelein J. C.. Thermophysical characteristics of LOX-H_2 flames at supercritical pressure. *Proceedings of the Combustion Institute*, 30:2929-2937, 2005.
18. Oefelein J. C., Schefer R. W., and Barlow R. W.. Toward validation of LES for turbulent combustion. *AIAA Journal*, 44(3):418-433, 2006.
19. Oefelein J. C., Sankaran V., and Drozda T. G.. Large eddy simulation of swirling particle-laden flow in a model axisymmetric combustor. *Proceedings of the Combustion Institute*, 31:2291-2299, 2007.
20. Williams T. C., Schefer R. W., Oefelein J. C., and Shaddix C. R.. Idealized gas turbine combustor for performance research and validation of large eddy simulations. *Review of Scientific Instruments*, 78(3).035114-1-9, 2007. doi:10.1063/1.27.12936.
21. Oefelein J. C. and Lacaze G.. Low-temperature injection dynamics and turbulent flame structure in high-pressure supercritical flows. *Proceedings of the 23rd International Colloquium on the Dynamics of Explosions and Reactive Systems*, July 24-29 2011. Irvine, California.
22. Oefelein, J., Dahms, R., and Lacaze, G., "Detailed Modeling and Simulation of High-Pressure Fuel Injection Processes in Diesel Engines," *SAE Int. J. Engines* 5(3):1410-1419, 2012, doi:10.4271/2012-01-1258.
23. Oefelein J. C., Dahms R. N., Lacaze G., Manin J. L., and Pickett L. M.. Effects of pressure on the fundamental physics of fuel injection in diesel engines. *Proceedings of the 12th International Conference on Liquid Atomization and Spray Systems*, September 2-6 2012. Heidelberg, Germany.
24. Oefelein J. C.. Large eddy simulation of complex thermophysics in advanced propulsion and power systems. *Proceedings of the 8th Joint Meeting of the US Sections of the Combustion Institute, Invited Plenary Presentation and Paper*, May 19-22 2013. Park City, Utah.
25. Erlebacher G., Hussaini M. Y., Speziale C. G., and Zang T. A.. Toward the large eddy simulation of compressible turbulent flows. *Journal of Fluid Mechanics*, 238:155-185, 1992.
26. Speziale C. G.. Galilean invariance of subgrid-scale stress models in the large eddy simulation of turbulence. *Journal of Fluid Mechanics*, 156:55-62, 1985.
27. Germano M., Piomelli U., Moin P., and Cabot W. H.. A dynamic subgrid-scale eddy viscosity model. *Physics of Fluids*, 3(7):1760-1765, 1991.
28. Moin P., Squires K., Cabot W., and Lee S.. A dynamic subgrid-scale model for compressible turbulence and scalar transport. *Physics of Fluids*, 3(11):2746-2757, 1991.
29. Lilly D. K.. A proposed modification of the germano subgrid-scale closure method. *Physics of Fluids*, 3(11): 633-635, 1992.
30. Zang Y., Street R. L., and Koseff J. R.. A dynamic mixed subgrid-scale model and its application to turbulent recirculating flows. *Physics of Fluids*, 5(12):3186-3195, 1993.
31. Vreman B., Geurts B., and Kuerten H.. On the formulation of the dynamic mixed subgrid-scale model. *Physics of Fluids*, 6(12):4057-4059, 1994.
32. Smagorinsky J.. General circulation experiments with the primitive equations. I. The basic experiment. *Monthly Weather Review*, 91:99-164, 1963.
33. Leland T. W. and Chappelear P. S.. The corresponding states principle. A review of current theory and practice. *Industrial and Engineering Chemistry Fundamentals*, 60 (7):15-43, 1968.
34. Rowlinson J. S. and Watson I. D.. The prediction of the thermodynamic properties of fluids and fluid mixtures-I. The principle of corresponding states and its extensions. *Chemical Engineering Science*, 24(8):1565-1574, 1969.
35. Reid R. C., Prausnitz J. M., and Polling B. E.. *The Properties of Liquids and Gases*. McGraw-Hill, New York, New York, 4th edition, 1987.
36. VanWylen G. J. and Sonntag R. E.. *Fundamentals of Classical Thermodynamics*. John Wiley and Sons, Incorporated, New York, New York, 3rd edition, 1986.
37. Gordon S. and McBride B. J.. Computer program for calculation of complex chemical equilibrium compositions, rocket performance, incident and reflected shocks and Chapman-Jouguet detonations. Technical Report NASA SP-273, National Aeronautics and Space Administration, 1971.
38. Kee R. J., Rupley F. M., and Miller J. A.. Chemkin thermodynamic data base. Technical Report SAND87-8215B, Sandia National Laboratories, 1990. Supersedes SAND87-8215 dated April 1987.
39. Ely J. F. and Hanley H. J. M.. Prediction of transport properties. 1. Viscosity of fluids and mixtures. *Industrial and Engineering Chemistry Fundamentals*, 20(4): 323-332, 1981.
40. Ely J. F. and Hanley H. J. M.. Prediction of transport properties. 2. Thermal conductivity of pure fluids and mixtures. *Industrial and Engineering Chemistry Fundamentals*, 22(1):90-97, 1981.

41. Bird R. B., Stewart W. E., and Lightfoot E. N.. *Transport Phenomena*. John Wiley and Sons, Incorporated, New York, New York, 1960.
42. Hirschfelder J. O., Curtiss C. F., and Bird R. B.. *Molecular Theory of Gases and Liquids*. John Wiley and Sons, Incorporated, New York, New York, 2nd edition, 1964.
43. Takahashi S.. Preparation of a generalized chart for the diffusion coefficients of gases at high pressures. *Journal of Chemical Engineering of Japan*, 7(6):417-420, 1974.
44. Pickett L. M., Genzal C. L., Manin J., Malbec L.-M., and Hermant L.. Measurement uncertainty of liquid penetration in evaporating diesel sprays. *Proceedings of the 23rd Annual Conference on Liquid Atomization and Spray Systems*, May 15-18 2011. Ventura, California.

CONTACT INFORMATION

Joseph C. Oefelein
oefelei@sandia.gov

ACKNOWLEDGMENTS

Support for this research was provided jointly by the U. S. Department of Energy; Office of Science (SC), Basic Energy Sciences (BES) program; and the Office of Energy Efficiency and Renewable Energy (EERE), Vehicle Technologies (VT) program, under grant numbers KC0301020 and VT0401000. Development of the foundational property evaluation schemes for multicomponent hydrocarbon mixtures was supported by the SC-BES program. Application of these tools to advanced engine combustion simulations was supported by the EERE-VT program. Sandia National Laboratories is a multiprogram laboratory operated by Sandia Corporation, a Lockheed Martin Company, for the United States Department of Energy under contract DE-AC04-94-AL85000. This research used resources of the Oak Ridge Leadership Computing Facility located in the Oak Ridge National Laboratory, which is supported by the Office of Science under Contract DE-AC05-00OR22725.

C.3 Article présenté au *35th Symposium (Int) on Combustion*

Available online at www.sciencedirect.com

ScienceDirect

Proceedings of the Combustion Institute xxx (2014) xxx–xxx

Proceedings of the Combustion Institute

www.elsevier.com/locate/proci

Analysis of high-pressure Diesel fuel injection processes using LES with real-fluid thermodynamics and transport

Guilhem Lacaze [a,*], Antony Misdariis [b], Anthony Ruiz [a], Joseph C. Oefelein [a]

[a] *Combustion Research Facility, Sandia National Laboratories, Livermore, CA 94551, USA*
[b] *Renault SAS, 1 Avenue Cornuel, 91570 Lardy, France*

Abstract

Imaging has long shown that under some high-pressure conditions, the presence of discrete two-phase flow processes becomes diminished. Instead, liquid injection processes transition from classical sprays to dense-fluid jets with no drops present. When and how this transition occurs, however, was not well understood until recently. In this paper, we summarized a new theoretical description that quantifies the effects of real fluid thermodynamics on liquid fuel injection processes as a function of pressure at typical Diesel engine operating conditions. We then apply the Large Eddy Simulation (LES) technique coupled with real-fluid thermodynamics and transport to analyze the flow at conditions when cylinder pressures exceed the thermodynamic critical pressure of the injected fuel. To facilitate the analysis, we use the experimental data posted as part of the Engine Combustion Network (see www.sandia.gov/ECN); namely the "Spray-A" case. Calculations are performed by rigorously treating the experimental operating conditions. Numerical results are in good agreement with available experimental measurements. The high-fidelity simulation is then used to analyze the details of transient mixing and understand the processes leading to auto-ignition. The analysis reveals the profound effect of supercritical fluid phenomena on the instantaneous three-dimensional mixing processes. The large density ratio between the supercritical fuel and the ambient gas leads to significant penetration of the jet with enhanced turbulent mixing at the tip and strong entrainment effects. Using detailed chemistry, a map of the auto-ignition delay time was calculated in simulation results. This map shows that a large flammable region with low velocity and mixture gradients is generated 250 diameters downstream of the injector. In the experiment, the first ignition site is observed at this location. This correspondence seems to indicate that the ignition location is piloted by the efficient mixing operating at the extremity of the jet coupled with long residence times, low strain rates and low scalar gradients.
Published by Elsevier Inc. on behalf of The Combustion Institute.

Keywords: LES; Diesel fuel injection; Supercritical fluids; Real-fluid thermodynamics

* Corresponding author. Address: Combustion Research Facility, Sandia National Laboratories, 7011 East Avenue, Mail Stop 9051, Livermore, CA 94551-0969, USA. Fax: +1 (925) 294 3055.
E-mail address: gnlacaz@sandia.gov (G. Lacaze).

http://dx.doi.org/10.1016/j.proci.2014.06.072
1540-7489/Published by Elsevier Inc. on behalf of The Combustion Institute.

1. Introduction

Future Diesel engines will operate in high pressure, low temperature regimes with significantly optimized fuel injection systems. As such, the current research is focused on developing a better understanding of fuel mixing at elevated pressures and the related transient mixing mechanisms. Research over the past decade has provided significant insights into the structure and dynamics of multiphase flows at high pressures. Most of this research has been done in the context of liquid-rocket propulsion. Imaging has long shown that under some high-pressure conditions, the injection mechanisms of a liquid into a gaseous environment change dramatically. At low pressures, classical primary and secondary atomization occurs leading to the formation of drops that subsequently evaporate. At high-pressure, surface tension diminishes as intermolecular interactions become symmetrical at the liquid–gas interface. The resultant force toward the liquid becomes as strong as the one toward the gas, which results in the suppression of atomization. The mixing of the dense fluid then depends on turbulence where large density gradients play an important role. Recent findings can be found in the review papers of Oschwald et al. [1] and Chehroudi [2]. Characteristic experimental imaging of the phenomenon is presented in the study by Mayer et al. [3]. Simulations in rocket-like configurations also confirm the impact of supercritical fluid phenomena at such conditions [4–6]. The references cited here only reflect the most representative work on rocket flows. The trends observed in rocket engines are equally valid for other liquid fueled devices. Here we focus on Diesel engines at conditions where the fuel is injected at conditions that exceed its thermodynamic critical pressure. In particular, recent research by Dahms and Oefelein [7,8] has provided new conceptual insights into Diesel injection processes at high-pressures. Prior to this work, the transition mechanism was not well understood. To the Author's knowledge, the theory presented in Refs. [7,8] is the first to quantify this transition. A key output are regime diagrams such as the example shown in Fig. 1. Detailed analysis of the gas–liquid interfacial structure quantifies under what conditions "classical" spray dynamics transition to diffusion dominated mixing. Predictions have been corroborated using microscopic imaging to visualize the features of dense-fluid jets (top right image in Fig. 1) and classical spray atomization (bottom right image). Analysis of the trends suggests that most high-performance combustion devices currently operate over ranges of pressures and temperatures in the vicinity of this transitional regime.

The regime diagram in Fig. 1 shows results for n-dodecane injected at a temperature of 363 K into gaseous nitrogen at varying ambient pressures and temperatures. The classical spray regime (highlighted in white) and diffusion-dominated mixing regime (gray) are found using the Knudsen-number criterion explained in Ref. [8]. To illustrate the relevance of this diagram, ambient gas pressure–temperature lines, which span a range of conditions during different Diesel engine compression cycles, are shown for three representative conditions; (a) high-load, (b) medium-load, and (c) light-load operation. The corresponding initial pressures and temperatures are (a) 2.5 bar, 363 K, (b) 1.6 bar, 343 K, and (c) 1 bar, 335 K, respectively. Fuel injection then occurs at full compression conditions, as indicated by the three respective points in the diagram. Interestingly, the cylinder pressures at full compression exceed the supercritical mixture pressure for all of the cases considered. Only under representative light-load operation does there appear to be a chance that classical fuel spray atomization takes place. Thus, contrary to conventional wisdom, the regime diagram suggests that classical spray phenomena does not occur at typical Diesel injection conditions. Instead, the fuel jet exhibits diminished interfacial structure and surface tension, which leads to diffusion-dominated mixing.

To enhance our understanding of the processes described above, we have combined the new theoretical findings and the Large Eddy Simulation (LES) technique to gain a more detailed view into direct injection processes in Diesel engines. At the conditions of interest, mixing layer dynamics are dominated by non-ideal thermodynamics and transport processes. We use the experimental data of the "Spray-A" case (n-dodecane), provided by several groups from the Engine Combustion Network (see www.sandia.gov/ECN [9]). This case corresponds identically to the conditions depicted by the dense-fluid jet image shown at the top right in Fig. 1. LES is performed using the real-fluid model described below. Results are then analyzed from the perspective of real-fluid thermodynamics with emphasis on the state of the transient mixing field prior to auto-ignition.

2. Approach

LES is performed using a single unified code framework called RAPTOR, which is a fully compressible solver that has been optimized to meet the strict algorithmic requirements imposed by the LES formalism. The theoretical framework solves the fully coupled conservation equations of mass, momentum, total-energy, and species for a chemically reacting flow. It is designed to handle high Reynolds number, high-pressure, real-gas and/or liquid conditions over a wide Mach operating range. It also accounts for detailed thermodynamics and transport processes at the

Please cite this article in press as: G. Lacaze et al., *Proc. Combust. Inst.* (2014), http://dx.doi.org/10.1016/j.proci.2014.06.072

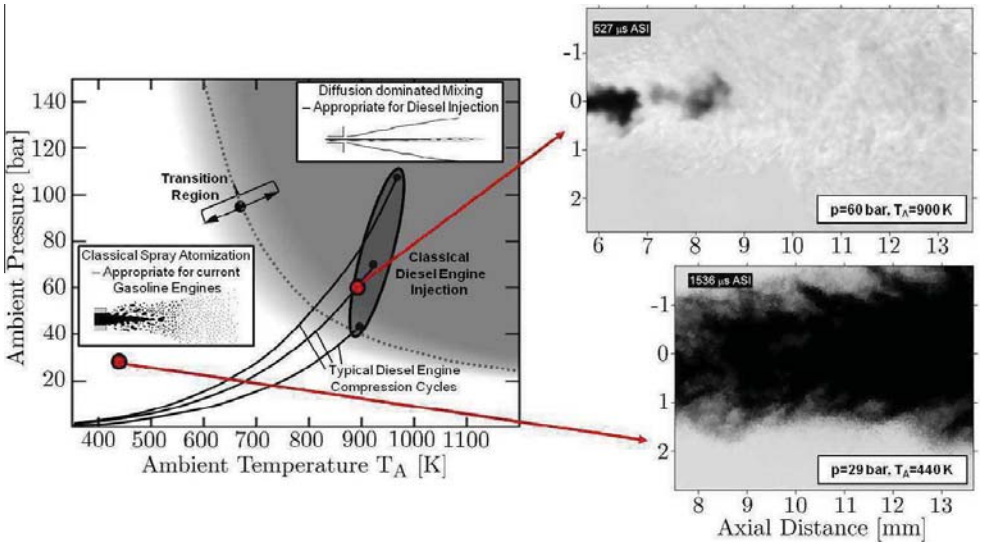

Fig. 1. Regime diagram for n-dodecane injected at a temperature of 363 K into nitrogen suggests the presence of dense supercritical jets under Diesel engine conditions without drop formation. High-speed imaging of both a dense jet and spray illustrates the significant transitional change that occurs at high supercritical pressures [7,8] (Images on right courtesy of L.M. Pickett, Sandia National Laboratories, Combustion Research Facility).

molecular level, and is sophisticated in its ability to handle a generalized model framework. A noteworthy aspect of RAPTOR is it was designed specifically for LES using non-dissipative, discretely conservative, staggered, finite-volume differencing. This eliminates numerical contamination of the subgrid-scale models due to artificial dissipation and provides discrete conservation of mass, momentum, energy, and species, which is an imperative requirement for high quality LES. Details related to the baseline formulation and subgrid-scale models are given by Oefelein [10]. Representative case studies are given by Oefelein et al. [11–14,16–19].

The baseline system of equations are cast in dimensionless form using a reference length-scale δ_{ref}, flow speed U_{ref}, and fluid state characterized by a reference density ρ_{ref}, sound speed c_{ref}, constant pressure specific heat $C_{p_{\text{ref}}}$, and dynamic viscosity μ_{ref}. Using these quantities, reference Mach and Reynolds numbers are defined as $M = U_{\text{ref}}/c_{\text{ref}}$ and $Re = \rho_{\text{ref}} U_{\text{ref}} \delta_{\text{ref}}/\mu_{\text{ref}}$. With these definitions, the filtered conservation equations of mass, momentum, total-energy and chemical species can be written in conservative form as follows:

$$\frac{\partial \overline{\rho}}{\partial t} + \nabla \cdot (\overline{\rho}\tilde{\mathbf{u}}) = 0, \tag{1}$$

$$\frac{\partial}{\partial t}(\overline{\rho}\tilde{\mathbf{u}}) + \nabla \cdot \left[\left(\overline{\rho}\tilde{\mathbf{u}} \otimes \tilde{\mathbf{u}} + \frac{\mathcal{P}}{M^2}\mathbf{I}\right)\right] = \nabla \cdot \vec{\mathcal{T}}, \tag{2}$$

$$\frac{\partial}{\partial t}(\overline{\rho}\tilde{e}_t) + \nabla \cdot [(\overline{\rho}\tilde{e}_t + \mathcal{P})\tilde{\mathbf{u}}] = \nabla \cdot \left[\left(\vec{\mathcal{Q}}_e + M^2(\vec{\mathcal{T}} \cdot \tilde{\mathbf{u}})\right)\right] + \dot{\overline{\mathcal{Q}}}_e, \tag{3}$$

$$\frac{\partial}{\partial t}(\overline{\rho}\widetilde{Y}_i) + \nabla \cdot (\overline{\rho}\widetilde{Y}_i\tilde{\mathbf{u}}) = \nabla \cdot \vec{\mathcal{S}}_i + \overline{\dot{\omega}}_i. \tag{4}$$

The terms $\mathcal{P}$, $\vec{\mathcal{T}}$, $\vec{\mathcal{Q}}_e$ and $\vec{\mathcal{S}}_i$ represent respective composite (i.e., molecular plus subgrid-scale) stresses and fluxes. The terms $\dot{\overline{\mathcal{Q}}}_e$ and $\overline{\dot{\omega}}_i$ represent the filtered energy and species source terms.

The subgrid-scale closure is obtained using the "mixed" dynamic Smagorinsky model by combining the models proposed by Erlebacher et al. [20] and Speziale [21] with the dynamic modeling procedure [22–26]. The composite stresses and fluxes in Eqs. (1)–(4) are then given as:

$$\vec{\mathcal{T}} = (\mu_t + \mu)\frac{1}{Re}\left[-\frac{2}{3}(\nabla \cdot \tilde{\mathbf{u}})\mathbf{I} + \left(\nabla\tilde{\mathbf{u}} + \nabla\tilde{\mathbf{u}}^T\right)\right] - \overline{\rho}\left(\widetilde{\tilde{\mathbf{u}} \otimes \tilde{\mathbf{u}}} - \tilde{\tilde{\mathbf{u}}} \otimes \tilde{\tilde{\mathbf{u}}}\right), \tag{5}$$

$$\vec{\mathcal{Q}}_e = \left(\frac{\mu_t}{Pr_t} + \frac{\mu}{Pr}\right)\frac{1}{Re}\nabla\tilde{h} + \sum_{i=1}^{N}\tilde{h}_i\vec{\mathcal{S}}_i - \overline{\rho}\left(\widetilde{\tilde{h}\tilde{\mathbf{u}}} - \tilde{\tilde{h}}\tilde{\tilde{\mathbf{u}}}\right), \text{ and} \tag{6}$$

$$\vec{\mathcal{S}}_i = \left(\frac{\mu_t}{Sc_{t_i}} + \frac{\mu}{Sc_i}\right)\frac{1}{Re}\nabla\widetilde{Y}_i - \overline{\rho}\left(\widetilde{\widetilde{Y}_i\tilde{\mathbf{u}}} - \tilde{\widetilde{Y}}_i\tilde{\tilde{\mathbf{u}}}\right). \tag{7}$$

The term μ_t represents the subgrid-scale eddy viscosity given by

$$\mu_t = \overline{\rho}C_R\Delta^2\Pi_{\tilde{\mathbf{S}}}^{\frac{1}{2}}, \tag{8}$$

where

$$\Pi_{\tilde{\mathbf{S}}} = \tilde{\mathbf{S}} : \tilde{\mathbf{S}}, \text{ and } \tilde{\mathbf{S}} = \frac{1}{2}\left(\nabla\tilde{\mathbf{u}} + \nabla\tilde{\mathbf{u}}^T\right). \tag{9}$$

The terms C_R, Pr_t, and Sc_{t_i} represent the modified Smagorinsky, subgrid-scale Prandtl, and sub-

grid-scale Schmidt numbers, respectively, and are evaluated dynamically as functions of space and time. In expressions (5)–(7), the second terms of the right-hand-side are the respective Leonard cross-term stresses. The overall model provides a Favre averaged generalization of the Smagorinsky eddy viscosity model [27] coupled with gradient diffusion models to account for subgrid-scale mass and energy transport processes.

Equations (1)–(4) coupled with an appropriate equation of state, appropriate treatments of thermodynamic and transport properties, and validated mixing and combining rules accommodate the most general system of interest including cases when multicomponent and/or preferential diffusion processes are present. The property evaluation scheme used for the current study is designed to account for thermodynamic non-idealities and transport anomalies over a wide range of pressures and temperatures. The scheme is comprehensive and intricate, thus only a skeletal description can be given here. The extended corresponding states model [28,29] is employed with a cubic equation of state. Experience has shown that both the Soave–Redlich–Kwong (SRK) and Peng–Robinson (PR) equations, when used in conjunction with the corresponding states principle, can give accurate results over the range of pressures, temperatures, and mixture states of interest here. The SRK coefficients are adjusted to fit vapor pressure data and are thus more suitable for conditions when the reduced temperature is less than one. The PR coefficients, on the other hand, are more suitable for conditions when the reduced temperature is greater than one. Here the PR equation of state was used exclusively.

A summary of the cubic equations of state and recommended constants is given by Reid et al. [30, Chapter 3]. Having established an analytical representation for real mixture pressure–volume–temperature (PVT) behavior, the thermodynamic properties are obtained in two steps. First, respective component properties are combined at a fixed temperature using the extended corresponding states methodology to obtain the mixture state at a given reference pressure. A pressure correction is then applied using departure functions of the form given by Reid et al. [30, Chapter 5]. These functions are exact relations derived using the Maxwell relations (e.g., see VanWylen and Sonntag [32, Chapter 10]) and make full use of the real mixture PVT path dependencies dictated by the equation of state. Standard state properties are obtained using the databases developed by Gordon and McBride [33] and Kee et al. [34]. Molecular transport properties are evaluated in a manner analogous to the thermodynamic properties. Viscosity and thermal conductivity are obtained using the extended corresponding states methodologies developed by Ely and Hanley [35]. Mass and thermal diffusion coefficients are obtained using the methodologies outlined by Bird et al. [36] and Hirschfelder et al. [37] in conjunction with the corresponding states methodology proposed by Takahashi [38].

3. Results and discussion

Using LES with the real-fluid model framework described above, we have performed a series of studies aimed at understanding the diffusion dominated mixing phenomena illustrated in Fig. 1. We focus on the Spray-A experiment described by Pickett et al. [9]. Liquid n-dodecane at 363 K is injected through a 0.09 mm diameter injector nozzle into a gaseous mixture at 900 K and 60 bar. These are precisely the same conditions represented by the dense-fluid jet image shown at the top right in Fig. 1. The peak injection velocity is 620 m/s, which was selected to provide the same injected mass flow rate as the experiment. A synthetic turbulent signal with a turbulent intensity of 5-percent is superimposed on the bulk profile. Measurements have shown that the vessel temperature is almost uniform in space, which justifies the use of adiabatic walls in the simulation. The grid spacing in the vicinity of the injector exit is approximately 4 μm, with the grid stretched optimally in the downstream and radial directions. The integration time step is 2.3 ns.

Figure 2 shows a qualitative comparison of the injection sequence. Results from the LES are compared to the shadowgraphs from Pickett et al. [39]. The experimental images were obtained using a diffuser back illumination method, with the dense region highlighted using an arbitrary cut-off value in the gray scale. Based on recommendations from Pickett et al., instantaneous shots of the LES temperature field were chosen for comparisons. Comparisons between respective images shows qualitatively good agreement between the experiment and LES. Large structures present in the back-illumination images are also observed in the numerical results. The density of the n-dodecane jet is slightly above 700 kg/m^3 at the injector nozzle exit whereas the density of the ambient gas is 22.8 kg/m^3. The presence of strong density gradients is known to have a stabilization effect on hydrodynamic instabilities [31], which delays the destabilization of the jet. Once destabilization occurs, parcels of dense fluid detach from the compressed liquid jet. The dense fragments can still be observed 70 diameters (6.3 mm) downstream of the injector exit. The presence of these fast-moving structures enhances local turbulence. The eddies generated in the shear layers significantly affect mixing.

The vapor and "liquid" penetration trajectories are shown in Fig. 3. In the LES, vapor penetration is detected by the most upstream point of the iso-surface characterized by a mixture fraction

Please cite this article in press as: G. Lacaze et al., *Proc. Combust. Inst.* (2014), http://dx.doi.org/10.1016/j.proci.2014.06.072

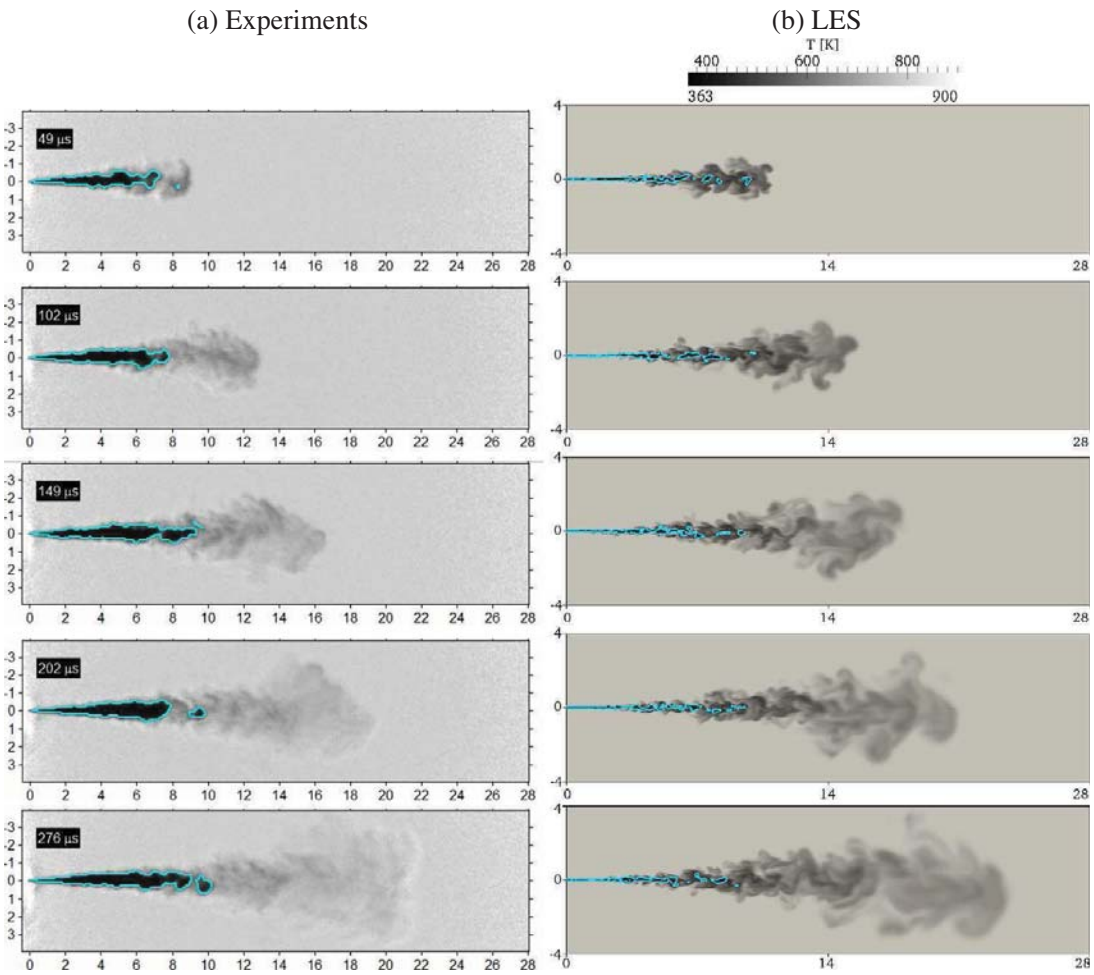

Fig. 2. Injection sequence showing (a) shadowgraphs from Pickett et al. [39] and (b) corresponding LES fields. Images are obtained using diffused back illumination with a grayscale intensity threshold set to qualitatively indicate the dense liquid region. Based on recommendations from Picket et al., instantaneous shots of the LES temperature field were chosen for comparisons. Spatial graduations are in mm and time is in μs, as indicated in the respective images.

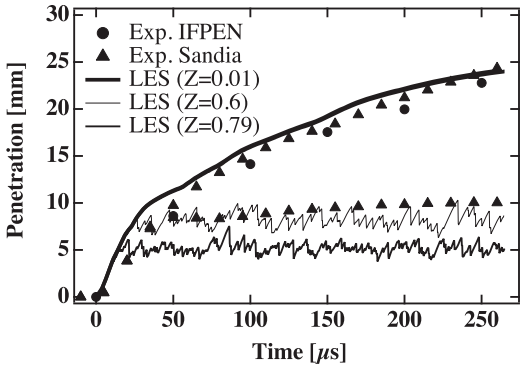

Fig. 3. Vapor and liquid penetration trajectories of the jet. The time-resolved liquid core length was determined from high-speed Mie-scatter imaging using a 3-percent threshold of maximum intensity.

of $Z = 0.01$. The sensitivity of this value has been tested and penetration curves have less than 2-percent variation between $Z = 0.01$ and $Z = 0.1$. LES results are in good agreement with experimental measurements, except at the initial phase of injection ($t < 50$ μs). During the initial startup, the simulated vapor penetration is slightly over-predicted. This is possibly an artifact of boundary anomalies associated with the interior sac and nozzle regions of the injector or a slight miss-match in the rate of injection. The time-resolved liquid core length was determined from high-speed Mie-scatter imaging using a 3-percent threshold of maximum intensity, which to some degree is an arbitrary value. Given the current premise that a distinct gas–liquid interface does not exist in this flow, defining the threshold associated with the compressed-liquid core requires additional analysis. Two liquid penetration curves are extracted from the LES to investigate. The first is based on a threshold of $Z = 0.79$, which is the value where the density changes the most with respect to Z (see Fig. 4b). The second was based on a threshold of $Z = 0.6$, which is simply the value that provides the best match with the experimental data. Both thresholds lead to the same trend as in the experiment.

Please cite this article in press as: G. Lacaze et al., *Proc. Combust. Inst.* (2014), http://dx.doi.org/10.1016/j.proci.2014.06.072

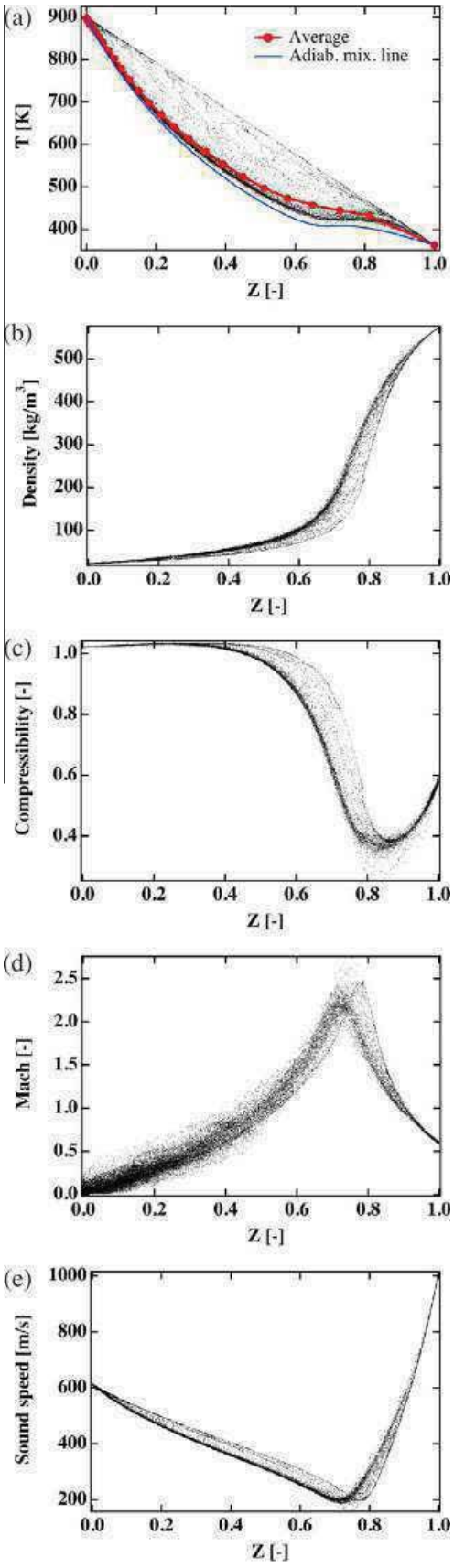

Fig. 4. Scatter plots describing the global mixture state just prior to ignition at $t = 260$ μs.

A plateau is observed in the temporal evolution with differing constant values of penetration depending on the mixture fraction value chosen.

A key focal point of this study is to better understand the local instantaneous mixture state of the jet immediately prior to auto-ignition, which occurs at approximately $t = 260$ μs after the start of injection. Figure 4 provides a global representation of the mixture state at this point in time. Scatter plots of (a) temperature, (b) density, (c) compressibility factor, (d) Mach number, and (e) speed of sound are shown as a function of mixture fraction. The adiabatic mixing temperature is also plotted in Fig. 4(a), as shown by the blue solid line. The red line represents the average. The non-linear relation between these quantities and mixture fraction can be largely attributed to real-gas thermodynamics, where large changes in temperature and density occur as a function of relatively small variations in composition. Scatter away from near adiabatic mixing can be attributed to multidimensional transport anomalies. Turbulent stretching and curvature induced by the evolving coherent structures amplifies preferential diffusion effects at both resolved- and sub-grid-scales.

Figure 4(d) and (e) reveals new and interesting conditions associated with real-fluid thermodynamics coupled with turbulent mixing: the Mach number in the flow varies from low-subsonic levels to approximately Mach 2.5. The speed of sound $\left(c = \sqrt{\gamma(\partial P/\partial \rho)_{T,Y_i}}\right)$ is seen to vary from approximately 600 m/s in the ambient gas, to 200 m/s at a mixture fractions of approximately $Z = 0.79$, to 1000 m/s in the pure fuel. In the mixing layer of the jet, non-linear thermodynamic effects lead to an increase in the ratio of specific heats and a significant decrease of the partial derivative $(\partial P/\partial \rho)_{T,Y_i}$ which globally results in strong decrease of the sound speed. In the same region, the entrainment caused by the high-speed jet induces flow velocities of approximately 400 m/s, which is more than two times the local sound speed. These localized regions of supersonic flow have a significant influence on the local pressure field and resultant scalar mixing processes.

To better understand the state of the transient mixing field just prior to auto-ignition, one can use the parametrization shown in Fig. 4 to approximate local ignition delay times in the mixture. The ignition time is estimated using perfectly stirred reactor (PSR) calculations, which do not take history effects into account but allow a first order estimate based on the present detailed numerical results. Using the observation that the scatter of temperature in mixture fraction space is small, the temperature can be described as a function of Z. To recover the composition of the reacting Spray-A case [42], we assumed that initial mixing processes are not affected by chemistry. Subsequently, the mixture fraction of the present case [39] (non-reacting) is used to retrieve the mixture composition of the reacting case where the

Please cite this article in press as: G. Lacaze et al., *Proc. Combust. Inst.* (2014), http://dx.doi.org/10.1016/j.proci.2014.06.072

reservoir is composed of 15% of oxygen by volume [42]. For a given mixture fraction, the mixture state is known and a PSR calculation is performed to determine the ignition time. For this analysis, the solver CANTERA [40] has been used with the detailed scheme developed by Westbrook et al. [41]. The chemical kinetics scheme is composed of 2115 species and 15,787 reactions. Figure 5 shows the type of data obtained. Temperature as a function of time for mixture fractions close to the stoichiometric value of $Z_{st} = 0.045$ are shown. As is consistent with experimental studies [15], a two-stage ignition process is observed. The auto-ignition time is defined as that needed for the PSR to reach 90-percent of its equilibrium temperature. Figure 6 shows the resulting auto-ignition time as a function mixture fraction. A fourth order polynomial is used to fit the data points located near the stoichiometric point where the auto-ignition time is less than 2.5 ms. This allows the auto-ignition field to be mapped over the mixture fraction field.

Using the results obtained above, we investigate the regions where auto-ignition is most likely to occur. Figure 7(a) shows the instantaneous fields (at $t = 260$ μs) of the ignition delay time, (b) the magnitude of the mixture fraction gradient, (c) the magnitude of the axial-component of velocity, and (d) the typical location where the first ignition kernels are observed in the experiment. Analysis of the temporal evolution of the these fields reveals that regions of the flow that are both flammable and have low values of scalar dissipation rate only appear approximately 200 μs after the start of injection. Thus, the instantaneous flow structure at 260 μs was selected to highlight where the ignition delay time is less than 2.5 ms. This allows us to focus on the structure of the chemically active regions. These data show that there are many favorable locations with low-auto-ignition mixtures within the mixing layer of the jet. Upstream locations before 200 diameters (18 mm) is where small pockets of flammable mixture appear first.

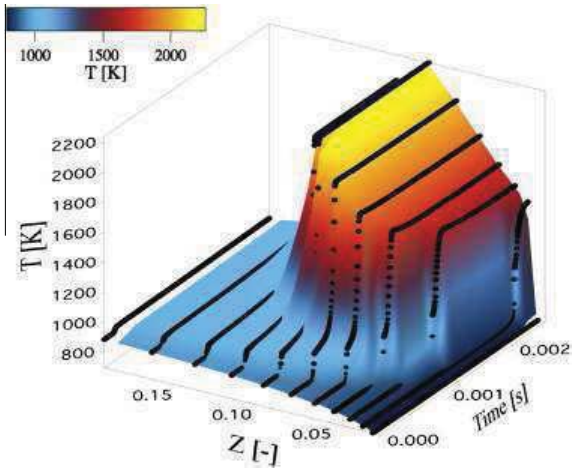

Fig. 5. Ignition delay time along mixing line.

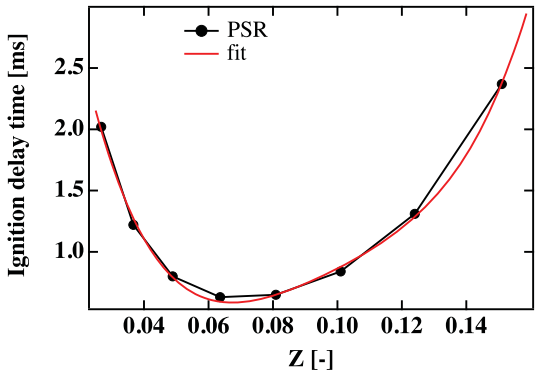

Fig. 6. Mapping of ignition delay time onto mixture fraction. Each point corresponds to a PSR simulation.

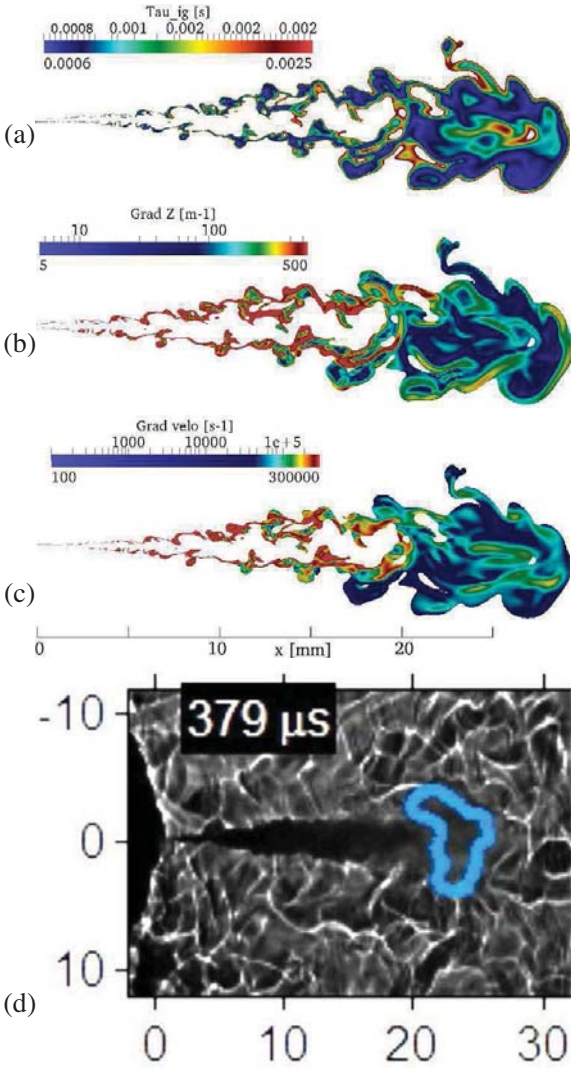

Fig. 7. Instantaneous flow structure close to the ignition time (260 μs) where the ignition delay is less than 2.5 ms; (a) ignition delay time, (b) magnitude of mixture fraction gradient, (c) magnitude of axial-component of velocity, and (d) typical location of first ignition kernels in the experiment [42].

However, Fig. 7(b) and (c) shows that strong velocity and mixture fraction gradients in these regions will prohibit the formation of the first flame kernels

Please cite this article in press as: G. Lacaze et al., *Proc. Combust. Inst.* (2014), http://dx.doi.org/10.1016/j.proci.2014.06.072

due to high stretch and scalar dissipation rate. Low gradients and larger flammable pockets are present between 200 and 250 diameters (18–22.5 mm) downstream of the injector, which is in qualitative agreement with the location of the initial kernels observed in the experiment. The large flammable mixture region observed at the extremity of the jet is the result of intense turbulent mixing enhanced by supercritical effects. The large density ratio between the compressed liquid fuel jet and the ambient gas is dominated by high-pressure thermodynamics, and intensifies the mixing mechanism at the tip of the liquid core (≈10 mm downstream of the injector). In this region, dense pockets of fuel are ejected at high velocity in the surrounding gas. This leads to an increase of turbulence and entrainment effects. As the mixture is convected downstream, the dense fuel pockets dissolve and turbulent mixing processes transition from supercritical (dense fluid into light gas) to a more classical turbulent mixing (gas into gas). Large entrainment structures force the equivalence ratio of the mixture to decrease. This goes along with an increase of its chemical reactivity as near stoichiometric conditions are attained. The turbulent mixing transition also yields a decrease of velocity and scalar gradients. This sequence of events serves to quantify the location of the initial flame kernels observed experimentally. The results represent a first step toward the development of a robust ignition model based on an appropriately reduced version of the Westbrook et al. [41] mechanism.

4. Conclusions

Imaging has long shown that under some high-pressure conditions, the presence of discrete two-phase flow processes becomes diminished. Under such conditions, liquid injection processes transition from classical sprays to dense-fluid jets, with no drops present. When and how this transition occurs, however, was not well understood until recently. In this paper, we have summarized a new theoretical description that quantifies the effects of real fluid thermodynamics on liquid fuel injection processes as a function of pressure at typical Diesel engine operating conditions. We then focused on the effects of real-fluid thermodynamics and transport using the Large Eddy Simulation (LES) technique. Analysis was performed using the Engine Combustion Network (www.sandia.gov/ECN) Spray-A case. LES was performed by identically matching the operating conditions used in the experiments. Results were analyzed with emphasis placed on the state of the transient mixing field prior to auto-ignition.

The LES results reveal the instantaneous three-dimensional structure of the injected fuel jet with a degree of resolution that is not accessible by current experimental diagnostics. An unexpected feature of the results is the presence of supersonic regions in the mixing layer of the jet. This is a consequence of a significant decrease of speed of sound due to real-gas thermodynamics, turbulent mixing of hot ambient nitrogen with the cold fuel stream, and high fuel injection velocity. The subsequent compressibility effects lead to pressure waves that affect the destabilization and transient mixing of the injected fuel.

Two different mixing processes were identified where turbulence is profoundly modified by the non-linear properties of the supercritical flow. In the vicinity of the dense fuel core, the presence of large density gradients leads to an intensification of mixing. Fast-moving parcels of dense compressed fluid detach from the fuel core and enhance turbulence due to their high momentum, as they travel through the gas phase. Further downstream, the dense blobs of fuel disintegrate leading to the significant reduction of scalar and velocity gradients. The mixing mechanisms transition from supercritical (dense fluid into light gas) to a more classical turbulent mixing (gas into gas) as the flow evolves spatially.

Using the results above, we focused on the identification of the flammable regions resulting from the present non-ideal transient mixing processes. A series of perfectly-stirred-reactors were computed to generate a mapping of ignition delay time as a function of mixture fraction and the mixture state in the three-dimensional field. The mapping revealed the development of a large volume of highly reactive mixture downstream of the injector, where the ignition delay time, scalar dissipation rate, and strain rate are simultaneously minimized. This represents a very favorable condition for initiation of auto-ignition. The location of this region is consistent with experimental results as the initial flame kernel is observed in this zone. This suggests that auto-ignition is piloted by the coupling of a highly-reactive mixture with long induction time and low gradients. Future work will focus on the ignition transient and flame stabilization using a suitable chemical model and combustion closure.

Acknowledgments

Support for this research was provided jointly by the U.S. Department of Energy; Office of Science (SC), Basic Energy Sciences (BES) program; and the Office of Energy Efficiency and Renewable Energy (EERE), Vehicle Technologies (VT) program, under grant numbers KC0301020 and VT0401000. Development of the foundational property evaluation schemes for multicomponent hydrocarbon mixtures was supported by the SC-BES program. Application of these tools to advanced engine combustion simulations was

supported by the EERE-VT program. Sandia National Laboratories is a multiprogram laboratory operated by Sandia Corporation, a Lockheed Martin Company, for the United States Department of Energy under contract DE-AC04-94-AL85000. This research used resources of the Oak Ridge Leadership Computing Facility located in the Oak Ridge National Laboratory, which is supported by the Office of Science under Contract DE-AC05-00OR22725.

References

[1] M. Oschwald, J.J. Smith, R. Branam, et al., *Combust. Sci. Technol.* 178 (1–3) (2006) 49–100.
[2] B. Chehroudi, *Int. J. Aerosp. Eng.* 2012 (2012) 1–31.
[3] W.O.H. Mayer, A.H.A. Schik, B. Vielle, et al., *J. Propul. Power* 14 (4) (1998) 835–842.
[4] T. Schmitt, L. Selle, A. Ruiz, B. Cuenot, *Am. Inst. Aeronaut. Astronaut. J.* 48 (9) (2010) 2133–2145.
[5] T. Schmitt, J. Rodriguez, I.A. Leyva, S. Candel, *J. Fluid Mech.* 24 (2012) 1–30.
[6] L.C. Selle, N.A. Okong'o, J. Bellan, K.G. Harstad, *J. Fluid Mech.* 593 (2007) 57–91.
[7] R.N. Dahms, J. Manin, L.M. Pickett, J.C. Oefelein, *Proc. Combust. Inst.* 34 (2013) 1667–1675. http://dx.doi.org/10.1016/j.proci.2012.06.169.
[8] R.N. Dahms, J.C. Oefelein, *Phys. Fluids* 25 (092103) (2013) 1–24. http://dx.doi.org/10.1063/1.4820346.
[9] L.M. Pickett, Engine Combustion Network, Sandia National Laboratories, Combustion Research Facility, Livermore, California, 2005–2013, available at www.sandia.gov/ECN.
[10] J.C. Oefelein, *Prog. Aerosp. Sci.* 42 (1) (2006) 2–37.
[11] J.C. Oefelein, *Proc. Combust. Inst.* 30 (2005) 2929–2937.
[12] J.C. Oefelein, R.W. Schefer, R.W. Barlow, *AIAA J.* 44 (3) (2006) 418–433.
[13] J.C. Oefelein, V. Sankaran, T.G. Drozda, *Proc. Combust. Inst.* 31 (2007) 2291–2299.
[14] T.C. Williams, R.W. Schefer, J.C. Oefelein, C.R. Shaddix, *Rev. Sci. Instrum.* 78 (3) (2007) 035114-1–035114-9. http://dx.doi.org/10.1063/1.27.12936.
[15] M. Tanabe, T. Bolik, C. Eigenbrod, H.J. Rath, J. Sato, M. Kono, *Proc. Combust. Inst.* 26 (1) (1996) 1637–1643.
[16] J.C. Oefelein, G. Lacaze, *Proceedings of the 23rd International Colloquium on the Dynamics of Explosions and Reactive Systems*, Irvine, California.
[17] J.C. Oefelein, R.N. Dahms, G. Lacaze, *SAE Int. J. Engines* 5 (3) (2012) 1–10. http://dx.doi.org/10.4271/2012-10-1258.
[18] J.C. Oefelein, R.N. Dahms, G. Lacaze, J.L. Manin, L.M. Pickett, in: Proceedings of the 12th International Conference on Liquid Atomization and Spray Systems, Heidelberg, Germany. ISBN 978-88-903712-1-9.
[19] J.C. Oefelein, in: Proceedings of the 8th Joint Meeting of the US Sections of the Combustion Institute, Invited Plenary Presentation and Paper, Park City, Utah.
[20] G. Erlebacher, M.Y. Hussaini, C.G. Speziale, T.A. Zang, *J. Fluid Mech.* 238 (1992) 155–185.
[21] C.G. Speziale, *J. Fluid Mech.* 156 (1985) 55–62.
[22] M. Germano, U. Piomelli, P. Moin, W.H. Cabot, *Phys. Fluids* 3 (7) (1991) 1760–1765.
[23] P. Moin, K. Squires, W. Cabot, S. Lee, *Phys. Fluids* 3 (11) (1991) 2746–2757.
[24] D.K. Lilly, *Phys. Fluids* 3 (11) (1992) 633–635.
[25] Y. Zang, R.L. Street, J.R. Koseff, *Phys. Fluids* 5 (12) (1993) 3186–3195.
[26] B. Vreman, B. Geurts, H. Kuerten, *Phys. Fluids* 6 (12) (1994) 4057–4059.
[27] J. Smagorinsky, *Mon. Weather Rev.* 91 (1963) 99–164.
[28] T.W. Leland, P.S. Chappelear, *Ind. Eng. Chem. Fundam.* 60 (7) (1968) 15–43.
[29] J.S. Rowlinson, I.D. Watson, *Chem. Eng. Sci.* 24 (8) (1969) 1565–1574.
[30] R.C. Reid, J.M. Prausnitz, B.E. Polling, *The Properties of Liquids and Gases*, 4th Edition., McGraw-Hill, New York, 1987.
[31] I.A. Hannoun, H.J.S. Fernando, E.J. List, *J. Fluid Mech.* 189 (1988) 189–209.
[32] G.J. VanWylen, R.E. Sonntag, *Fundamentals of Classical Thermodynamics*, 3rd Edition., John Wiley and Sons, Incorporated, New York, 1986.
[33] S. Gordon, B.J. McBride, *Computer Program for Calculation of Complex Chemical Equilibrium Compositions, Rocket Performance, Incident and Reflected Shocks and Chapman-Jouguet Detonations*, Tech. Rep. NASA SP-273, National Aeronautics and Space Administration, 1971.
[34] R.J. Kee, F.M. Rupley, J.A. Miller, *Chemkin Thermodynamic Data Base*, Tech. Rep. SAND87-8215B, Sandia National Laboratories, supersedes SAND87-8215 dated April 1987, 1990.
[35] J.F. Ely, H.J.M. Hanley, *Ind. Eng. Chem. Fundam.* 20 (4) (1981) 323–332.
[36] R.B. Bird, W.E. Stewart, E.N. Lightfoot, *Transport Phenomena*, John Wiley and Sons, Incorporated, New York, 1960.
[37] J.O. Hirschfelder, C.F. Curtiss, R.B. Bird, *Molecular Theory of Gases and Liquids*, 2nd Edition., John Wiley and Sons, Incorporated, New York, 1964.
[38] S. Takahashi, *J. Chem. Eng. Jpn.* 7 (6) (1974) 417–420.
[39] L.M. Pickett, C.L. Genzal, J. Manin, L.-M. Malbec, L. Hermant, in: Proceedings of the 23rd Annual Conference on Liquid Atomization and Spray Systems, Ventura, California.
[40] D. Goodwin, Cantera: An Object-Oriented Software Toolkit for Chemical Kinetics, Thermodynamics, and Transport Processes, California Institute of Technology, Pasadena, California, 2009. Available at <http://code.google.com/p/cantera>.
[41] C.K. Westbrook, W.J. Pitz, O.H. Herbineta, H.J. Currana, E.J. Silkea, *Combust. Flame* 156 (2009) 181–199, http://dx.doi.org/10.1016/j.combustflame.2008.07.014.
[42] M. Bardi, R. Payri, L.-M. Malbec, et al., *Atomization Sprays* 22 (2012) 807–842.

INSTITUT NATIONAL POLYTECHNIQUE DE TOULOUSE
Doctorat d'Université, spécialité Dynamique des Fluides
04 Mars 2015
Antony Misdariis

Schémas cinétiques réduits et couplage thermique pour les simulations aux grandes échelles du cliquetis dans les moteurs à piston

Résumé

Pour améliorer le rendement des moteurs essence, une méthode efficace est le downsizing qui consiste en la diminution de la cylindrée moteur compensée par l'ajout d'un compresseur pour maintenir la puissance. Lorsque le niveau de downsizing est trop important les fortes pression et températures rencontrées favorisent l'apparition de phénomènes d'auto-allumage de type cliquetis ou rumble néfastes pour l'intégrité du moteur. Ce type de phénomène, aujourd'hui encore mal compris, constitue une limite à l'utilisation du downsizing. Dans cette thèse la Simulation aux Grandes Echelles est utilisée pour étudier ce type de combustion dite anormale. L'objectif est de proposer une méthodologie numérique capable de reproduire leurs apparitions pour en étudier les mécanismes. L'auto-allumage est un mode de combustion sensible aux variations des conditions thermodynamiques locales. Des méthodes numériques précises et des modèles appropriés, en particulier pour la thermique paroi doivent donc être utilisés. La première partie de ce manuscrit présente la méthodologie numérique proposée et en particulier deux aspects développés lors de cette thèse: un modèle d'auto-allumage qui permet de reproduire le délai d'auto-allumage des gaz frais avec un schéma cinétique réduit et une méthodologie de couplage entre la chambre de combustion et la culasse permettant de définir des champs de températures paroi réalistes. La seconde partie de ce manuscrit présente les résultats de deux études numériques reproduisant certains points de fonctionnement d'un moteur expérimental. La première étude est réalisée à l'aide de modèles de combustion de la littérature et vise à reproduire le comportement expérimental pour diverses variations paramétriques influant sur la combustion. La seconde étude est réalisée à l'aide des modèles développés dans cette thèse afin d'étudier l'impact de la thermique paroi dans les mécanismes d'apparition des combustions anormales.

Abstract

In order to improve the efficiency of gasoline engines, one efficient solution resides in engine downsizing which consists in the diminution of the engine size with the adjunction of a compressor to keep the power output. When the downsizing level is important, the high pressure and temperature levels promote auto-ignition phenomena such as knocking or rumble that can damage the engine. This kind of combustion, still misunderstood, is a limit to further use downsizing. In this thesis, Large Eddy Simulation is used to study this kind of abnormal combustions. The objective is to propose a numerical methodology able to reproduce its apparition and to understand its mechanisms. Auto-ignition is a combustion regime very sensitive to the variations of local thermodynamic conditions. Precise numerical methods and appropriate models, especially for thermal boundary conditions must be used. The first part of this manuscript presents the proposed numerical methodology and in particular two aspects implemented during this thesis: an auto-ignition model that permits to reproduce auto-ignition delays with reduced kinetic schemes and a coupling methodology between combustion chamber and cylinder head in order to obtain realistic temperature fields for the boundary conditions. The second part of this manuscript presents the results of two numerical studies that reproduce some operating points from an experimental engine database. The first study is performed using combustion models from the literature and aims at reproducing experimental behavior for various parametric variations impacting the combustion. The second study is performed thanks to the numerical models implanted in this thesis in order to evaluate the impact of the thermal boundary conditions on the mechanisms leading to abnormal combustions.